The structural use of alkali activated materials (Geopolymers)

by

Joachim Paul Louw

Thesis presented in fulfilment of the requirements for the degree of Master of Engineering in Civil Engineering in the Faculty of Engineering at Stellenbosch University

Department of Civil Engineering,
Stellenbosch University,
Private Bag X1, Matieland 7602, South Africa.

Supervised by:
Prof. W.P. Boshoff

March 2017

Declaration

By submitting this document, I declare that the work that is contained herein is my own original work. I know the meaning of plagiarism and declare all of the work, except for that which is properly acknowledged, is my own. I am the owner of this document and it has not been submitted for any other examination.

Joachim Paul Louw

Date: March 2017

Abstract

Alkali activated materials (AAMs), also referred to as geopolymer concretes, are a new generation of alternative construction materials, which are formed through the alkali activation of clinker-free binder materials, such as fly ash and slag. Compared to Ordinary Portland cement (OPC) concrete, the production of AAMs is associated with low energy consumption and low carbon dioxide (CO_2) emissions, together with promising mechanical properties.

The main goal of this study is to determine the structural use of a fly ash/slag based AAM, activated with sodium silicate and sodium hydroxide. The mechanical properties, with the focus on the compressive strength and the elastic modulus, as well as the structural behaviour of reinforced AAMs are investigated to achieve this goal.

For the mechanical properties of AAMs, several of mix parameters were varied, which include: the type of activator; the calcium content; the activator concentration; the dosage; the modulus of the activator; and the coarse aggregate content and size. Compressive strengths of up to 67 MPa were obtained, while the elastic modulus was low in comparison with that typically found for OPC concrete, with values between 10 GPa and 32 GPa. The mechanical properties were mainly influenced by calcium content, sodium hydroxide concentration and the activator modulus.

Large scale reinforced AAM beams were tested in bending in order to obtain the flexural behaviour of reinforced AAMs, while reinforcement pull-out tests were performed to determine the bond behaviour between AAMs and the reinforcement. For both these tests, two AAM mixes were compared against two OPC mixes with similar strengths. It was found that it is possible to use design codes, such as the EN 1992-1-1, (2004), for the ULS design of reinforced AAM beams. However, attention has to be given to the low elastic modulus in order to reduce the large deflections of the AAM beams. The design codes also seem to be inadequate for the deflection calculations of AAMs. Promising results were obtained in terms of the design bond stress of AAMs, as they were generally higher than that of the OPC-mixes. This indicates that shorter embedded lengths can possibly be used for AAMs.

It can be concluded that the AAMs is still some time away from being used as a structural material, as there is still a number of issues, for example the low elastic modulus, that need to be addressed. However, there is potential for AAMs as a structural material, if these problems are solved.

Opsomming

Alkali geaktiveerde materiale (AGMe), ook genoem geopolimeerbeton, is 'n nuwe generasie van alternatiewe konstruksie materiale. AGMe bestaan uit klinker-vry binder materiale, soos vliegas en slagment, wat geaktiveer word deur alkaliese oplossings. In vergelyking met normale "OPC" beton, word AGMe verband gehou met lae energieverbruik en lae vrystelling van koolstofdioksied (CO_2). Belowende meganiese eienskappe is ook al verky met AGMe.

Die hoofdoel van hierdie studie is om die strukturele gebruik van 'n vliegas/slagmentgebaseerde AGM, geaktiveer deur natrium silikaat en natrium hidroksied, te bepaal. Dit was gedoen deur die meganiese eienskappe, met die fokus op die druksterkte en elastisiteitsmodulus, sowel as die stukturele gedrag van bewapende AGMe te ondersoek.

Vir die meganiese eienskappe van AGMe, was verskeie meng variasies getoets . Hierdie meng variasies sluit in: die tipe aktiveerder; die kalsium inhoud; die aktiveerder konsentrasie; die aktiveerder- dosis en modulus; en die klip inhoud en grootte. Druksterktes van so hoog as 67 MPa was verkry, terwyl die elastisiteitsmodulus laag was (tussen 10 GPa en 32 GPa) in vergelyking met tipiese waardes verky deur OPC beton. Die meganiese eienskappe was hoofsaaklik beinvloed deur die kalsium inhoud, natrium hidroksied konsentrasie en die aktiveerder modulus.

Groot skaal bewapende AGM balke was getoets in buiging om die buig gedrag van bewapende AGMe te bepaal, terwyl die bindings gedrag tussen AGMe en staal bewapening verkry was deur bewapening uittrek toetse. Twee AGM menge was vergelyk met twee OPC menge met dieselfde sterktes, vir buide hierdie twee toetse. Dit was gevind dat ontwerp kodes, soos die EN 1992-1-1, (2004), kan gebruik word om bewapende AGM balke te ontwerp, maar aandag moet gegee word aan die lae elastiteitsmodulus om die groot defleksies te verhoed. Dit blyk ook of die ontwerp kodes onvoldoende is vir die defleksie berekeninge van AGMe. Belowende resultate was verkry in terme van die ontwerp-verbindingspanning vir AGMe, wat oor die algemeen groter was invergelyking met die OPC menge. Dit dui aan dat korter verbindings lengtes heel moontlik gebruik kan word vir AGMe.

Daar kan tot 'n gevolgtrekking gekom word dat AGMe groot potensiaal het as 'n alternatiewe strukturele materiaal, maar verkeie probleme, soos die lae elastisiteitsmodulus, sal eers ondersoek en opgelos moet word.

Acknowledgements

I would like to extend my thanks to the following people for their guidance, support and motivation which provided a great degree of encouragement to complete this study.

- Professor Billy Boshoff, for his mentorship, advice and guidance in conducting this study, and providing me with a great learning experience. Your patience and support is greatly appreciated.
- The staff at the University of Stellenbosch. I hope to make the most of all the advice and learning experiences I have gained during my years of study at the institute.
- The technical staff, for your assistance and companionship in the laboratories: Charlton Ramat, Peter Cupido and Johan van der Merwe.
- The secretarial staff for helping me with all the requests I had: Natalie Scheepers, Olivia van Wyk and Arthur Layman. Your assistance and friendliness has made the two years great.
- Andrew Heath from the University of Bath, for his advice and guidance on AAMs
- My family members, for their continual support, prayers and words of encouragement.
- My friends, with whom I shared an office with for two years. I will keep the memorable moments with me for a long time. The motivation, advice and encouragement means a lot. Thank you: Manus Bester, Lourens Steyl, Leon de Beer, Johannes Fourie, Willem van Jaarsveld, Johann Gerber, Nickilus Tredoux and Michael Drennan.

Finally, but not the least important, I would like to thank God, for His blessings have been abundant and full of glory.

Contents

List of Figures

List of Tables

Nomenclature

Latin letters

A	Compression area of cubes in compressive strength test, in mm^2
A_s	Area of tensile reinforcement in a beam section
A'_s	Area of compression reinforcement in a beam section
a	Deformation parameter taken as the strain, curvature, rotation or deflection
a_I	Deformation calculated for uncracked condition
a_{II}	Deformation calculated for fully cracked condition
b	Width of beam section
c_{clear}	Clear distance between the ribs of the steel reinforcement, in mm
d	Depth of tensile reinforcement in a beam section
d'	Depth of compression reinforcement in a beam section
E_c	Elastic modulus of concrete, in GPa
$\mathrm{E_d}$	Dissipated energy in reinforced beams, in $kN.m^2$
E_s	Elastic modulus of steel, in GPa
F	Failure load for compressive strength of concrete, in N
F_{cc}	Internal compression force in concrete due to bending of beams
F_{sc}	Internal compression force in steel due to bending of beams
F_{st}	Internal tensile force in steel due to bending of beams
$f_{c,cube}$	Cube compressive strength for concrete, in MPa
$f_{c,cyl}$	Cylinder compressive strength for concrete, in MPa
f_{cd}	Design strength for concrete, in MPa
f_{ck}	Characteristic cylinder compressive strength for concrete, in MPa
f_{ctd}	Design tensile strength for concrete, in MPa

$f_{ctk,0.05}$	5 % fractile value of the characteristic tensile strength for concrete, in MPa
f_{ctm}	Tensile strength for concrete, in MPa
f_{cu}	Characteristic cube compressive strength for concrete, in MPa
f_{cy}	Assumed yield stress for concrete, in MPa
f_u	Ultimate stress for steel, in MPa
f_y	Yield stress for steel, in MPa
f_{yc}	Yield stress for steel in compression, in MPa
f_{ycd}	Design stress for steel reinforcement in compression, in MPa
f_{yd}	Design stress for steel reinforcement, in MPa
$f_{\%}$	Stress percentage for stress-strain relationship of AAM mixes
I	Moment of inertia, in mm^4
M	Internal moment in reinforced beams
M_{cr}	Cracking moment
M_u	Ultimate moment during the bending of reinforced beams, in kN.m
m	Mass of the cube specimens, in kg
N	Normal force within reinforced concrete member
N_{cr}	Cracking force of concrete
P_s	Service load during bending of reinforced beams, kN
S	Slip of embedded reinforcement bar, in mm
S_1	First characteristic slip value, in mm
S_2	Second characteristic slip value, in mm
S_3	Third characteristic slip value, in mm
T	Tensile force in steel reinforcement, in N
V	Volume of the cube specimens, in m^3
x	Neutral axis for beam in bending

Greek letters

α	Regression constant of local bond-slip model
α_{cc}	Coefficient taking into account of the long term effects on the compressive strength of concrete and the unfavourable effects resulting from the way the load is applied

α_{ct}	Coefficient for the long term effects on tensile strength of concrete
β	The coefficient accounting for the influence of the duration of loading or repeated loading on the average strain
γ_c	Partial safety factor for concrete
γ_s	Partial safety factor for steel
Δ_s	Reinforced beam deflection at service load, in mm
Δ_u	Reinforced beam deflection at ultimate load, in mm
Δ_y	Reinforced beam deflection at yield load, in mm
ε_c	Concrete strain at ultimate stress
ε_{cu}	Concrete ultimate strain
ε_{cy}	Assumed yield strain of concrete
$\varepsilon_{\mathrm{p,2}}$	Strain recorded at preload stress level on the second load cycle of elastic modulus test, in mm/mm
ε_s	Steel reinforcement strain
ε_{sc}	Strain of compression steel reinforcement in reinforced beams
$\varepsilon_{s,y}$	Yield strain of steel reinforcement
ε_{st}	Strain of tensile steel reinforcement in reinforced beams
$\varepsilon_{\mathrm{u,3}}$	Strain recorded at upper stress level on the third load cycle of elastic modulus test, in mm/mm
$\varepsilon_{\%}$	Strain percentage for stress-strain relationship of AAM mixes
ζ	The interpolation coefficient for the deformation formula (allowing for the effect of tension stiffening at a section)
η	Factor used to define the effective strength for the assumed rectangular concrete stress block in beam design
η_1	Bond condition factor
η_2	Reinforcement bar size factor
λ	Factor used to define the effective height for the assumed rectangular concrete stress block in beam design
μ_d	Ductility index of reinforced beams
ρ	Concrete density, in $\mathrm{kg/m^3}$

σ_a	The bond stress at adhesion loss, in MPa
σ_b	Bond stress of embedded reinforcement, in MPa
σ_{bmax}	Peak bond stress, in MPa
σ_d	Design bond stress, in MPa
σ_f	Residual bond stress, in MPa
σ_{p}	Preload during the elastic modulus test, in MPa
σ_s	Tensile stress in embedded reinforcement bar, in MPa
σ_{sr}	Tensile stress in embedded reinforcement bar when the concrete cracks, in MPa
σ_{u}	Upper load during the elastic modulus test, in MPa
v_a	Adhesion stress
v_b	Bearing stress
v_s	Shear stress
ϕ	Reinforcement bar nominal diameter, in mm

Abbreviations

AAM	Alkali Activated Material
ACI	American Concrete Institute
BFS	Blast Furnace Slag
CV	Coefficient of Variation
DP	Degree of Depolymerisation
FA	Fly Ash
GGBS	Ground Granulated Blast-furnace Slag
GGCS	Ground Granulated Corex Slag
LOI	Loss Of Ignition
LVDT	Linear Variable Displacement Transducer
OPC	Ordinary Portland Cement
PO	Pull-Out (referring to the test procedures or specimens)
PPC	Pretoria Portland Cement
RB	Reinforced Beam (referring to the test procedures or specimens)
SD	Standard Deviation
ULS	Ultimate Limit State

Chemical notation

Al_2O_3	Aluminium oxide
$CaCO_3$	Calcium carbonate
CaO	Calcium oxide
$Ca(OH)_2$	Calcium hydroxide
CO_2	Carbon dioxide
Cr_2O_3	Chromium(III) oxide
Fe_2O_3	Iron oxide
H_2O	Water
KOH	Potassium hydroxide
K_2O	Potassium oxide
K_2SiO_3	Potassium silicate
$MgCO_3$	Magnesium carbonate
MgO	Magnesium oxide
MnO	Manganese(II) oxide
$NaHCO_3$	Sodium bicarbonate
$NaOH$	Sodium hydroxide
Na_2CO_3	Sodium carbonate
Na_2O	Sodium oxide
Na_2SiO_3	Sodium silicate
Na_2SO_4	Sodium sulfate
P_2O_5	Phosphorus pentoxide
SiO_2	Silica oxide
TiO_2	Titanium dioxide

Chapter 1

Introduction

Concrete is the most widely used, as well as preferred construction material, due to its favourable mechanical properties. In order to produce concrete, Ordinary Portland cement (OPC) is used as a binder. The worldwide production of OPC was approximately 4 Gt in 2013 and 4.2 Gt in 2014 (Statista, 2016). Even though the cement production remained constant in 2015, it is expected that the production will continue to grow by 3.7 % in 2016 and remain at a constant growth of approximately 4 % during 2017 and 2018 (Statista, 2016; PCA, 2015). This increase in OPC production indicates that concrete will continue as a preferred construction material.

The excessive use of OPC gives rise to several environmental problems. These problems include: the large amount of natural resources and energy consumed; damage caused during extraction of raw materials and most importantly the significant amount of carbon dioxide (CO_2) emissions during the production of OPC (Sumajouw et al., 2007). The global CO_2 emissions due to OPC is on average, approximately 866 kg CO_2 per tonne of clinker produced. The production, together with the processing and handling of OPC concretes contributes to roughly 7 % of the world's CO_2 emissions (De Villiers, 2015b). Therefore, in order to address these problems, it is necessary to find alternative binder materials to produce concrete.

Currently, by-products from industry such as fly ash, are used as partial replacement of OPC, leading to an estimated global reduction of 5-20 % in CO_2 emissions caused by OPC production. Concrete containing these by-products still exhibit excellent mechanical properties, as well as enhanced durability performance (De Villiers, 2015b; Grieve, 2009). There is a growing concern about the management of the by-products, with only approximately 20-30 % of these by-products used, mainly for OPC replacement, and the rest being disposed of in landfills (Álvarez-Ayuso et al., 2008). Thus, in addition to the reduction of environmental problems associated with OPC, the disposal of by-products also contribute to the use of an alternative construction material, namely alkali activated materials (AAMs).

Alkali activated materials (AAMs), also sometimes mistakenly referred to as geopolymers, are a class of "concrete" which contains no cement, but could still have calcium silicate hydrate as a binding product. The cement is replaced with binder materials such as slag and fly ash, while chemical activators are used to initiate the strengthening reaction.

These materials are classified into two groups, namely the activation of calcium rich binder materials and the activation of aluminosilicate binder materials. In the first, the binder material contains more than 70 % SiO_2 and CaO in its composition, forming a calcium silicate hydrate gel that contains aluminium within the structure (C-A-S-H) when activated with a mild alkaline solution. A zeolite like polymer is formed as the product in the second group of AAMs. Geopolymers fall under this class of AAMs (Li et al., 2010; Roy, 1999). A third type of AAM is also possible, namely the combination of the two types above. In these AAMs the binder material contains high amounts of calcium, silica and aluminium (Garcia-Lodeiro et al., 2015). The last mentioned type is the focus of this study.

1.1 Problem statement

Research over the past 80 years have demonstrated that AAMs exhibit comparable, or even superior properties to that of OPC concrete such as high early age strength gain, low shrinkage as well as fire- and acid resistance, among others (Diaz et al., 2010a; Li et al., 2010). These properties together with the fact that AAMs are more environmental friendly than OPC concrete, only producing approximately 20 % CO_2 normally produced by OPC concrete, make AAMs a very desirable alternative construction material (Sakulich et al., 2010).

However, there are several issues and unknowns regarding AAMs, which prevents it from being used as a structural material. Some of these issues that have been identified by various studies are: the hazardous sodium hydroxide which is used as an alkaline activator; methods to design AAMs for a specific structural strength; low elastic modulus of AAMs; and structural behaviour, such as the interaction between the reinforcement and the AAMs. If the issues regarding AAMs can be addressed, AAMs could be more widely used as an alternative structural material to OPC concrete.

Therefore, the main goal of this study is to determine whether AAMs can be used as structural material. In order to achieve this a fly ash/slag based AAM activated with sodium silicate and sodium hydroxide was investigated by means of four objectives. These objectives are discussed in the next section.

1.2 Objectives and methodology

The four objectives include: finding an alternative activator to hazardous sodium hydroxide; establishing relationships between constituents and the compressive strength for the mix design of AAMs; improving the low modulus of elasticity of AAMs; and determining the structural behaviour of reinforced AAMs. The approach that was followed to obtain these specific objectives, as well as the method/process that was used to address the objectives, are discussed in the following sections.

1.2.1 Objective 1: Finding an alternative activator to hazardous sodium hydroxide

Sodium hydroxide and sodium silicate are normally used in combination as activators for AAMs. Sodium hydroxide is used due to its reactivity. However, safety equipment and several safety measures are required when working with sodium hydroxide, as it is hazardous. Therefore, experienced people will be required on a construction site to use AAMs and to implement the necessary safety requirements. This makes it difficult to use AAMs as a structural material. Consequently, an alternative activator should be used for AAMs.

From several studies it was found that sodium silicate and/or sodium carbonate could also be used as alkaline activators (Bakharev et al., 1999; Fernández-Jiménez et al., 2003b; Wang et al., 1994; Collins et al., 1998). These two substances are not as hazardous to use as sodium hydroxide. Therefore, sodium silicate and sodium hydroxide were examined as alternative activators, in this study.

1.2.2 Objective 2: Establishing relationships between constituents and the compressive strength for the mix design of AAMs

There are several methods that are used to design an OPC concrete mix. One of these methods is the C&CI method (Addis et al., 2009). When this method is used, the concrete is designed for a specific compressive strength. The water-to-cement ratio is the main factor that contributes to the strength of the concrete (Addis et al., 2009).

A generic design method is not yet available in the public domain for AAMs, making it difficult to obtain a specific strength for a structural design. Thus, a method needs to be created in order to design an AAM mix. Before this can be done, relationships between the constituents of AAMs and the compressive strength, as the water-to-cement ratio in OPC concrete, first needs to be determined. These relationships can then be used to create a mix design method for AAMs.

Due to AAMs containing more constituents than OPC concrete (binder material, activator, water and aggregate), there are more variables that influence the strength. The major influencing variables that have been identified by previous studies include: the calcium content; activator concentration; activator dosage; activator modulus; and water content (Bernal et al., 2012; Fernández-Jiménez et al., 2006a; Temuujin et al., 2009). The dosage of the activator is defined as the ratio of Na_2O content within the alkaline activator to the mass of the binder (%Na_2O/binder), while the activator modulus is the mass ratio of the SiO_2 to the Na_2O in the activator (SiO_2/Na_2O ratio). These variables are depended on both the type of binder and activator used.

In this study the calcium content, activator concentration, activator dosage and activator modulus were investigated. A relationship was established between these variables and the compressive strength, contributing to future AAM mix design methods.

1.2.3 Objective 3: Improving the low modulus of elasticity of AAMs

The modulus of elasticity of concrete is an important property when designing structural elements, such as beams. This is because it is related to the stiffness of the concrete. For normal-density OPC concrete the modulus of elasticity generally ranges between 27 GPa and 38 GPa (EN 1992-1-1, 2004). However, it was found that ambient cured AAMs yielded low elastic modulus values of not more than 20 GPa (Barnard, 2014). This will result in large deflection when designing structural elements with AAMs. Therefore, the modulus of elasticity of AAMs needs to be improved.

Barnard, (2014) found that the concentration of the sodium hydroxide solution had the most significant effect on the elastic modulus of AAMs. He also obtained contradicting results in terms of the coarse aggregate content. The stiffness decreased with an increase in coarse aggregate content, where in OPC concrete the stiffness would increase, due to the higher stiffness of the aggregate.

The modulus of elasticity was determined for all of the variables as mentioned in Objective 2. This will ensure that a relationship is also established between the variables and the elastic modulus. From these relationships a possible prediction can be made to improve the elastic modulus of AAMs. The contradicting results for the aggregate content from Barnard, (2014), was also further investigated.

1.2.4 Objective 4: Determining the behaviour of reinforced AAMs

Today, all concrete structures are designed with reinforcement. Therefore, another important factor to consider when designing concrete structures, is the behaviour of reinforced concrete, specifically the flexural behaviour and the interaction between the concrete and the reinforcement. Research is limited on the behaviour of reinforced AAMs, therefore investigation is required.

In order to gain insight into the behaviour of reinforced AAMs, two tests were conducted. These tests include: large scale beams that were tested in bending; and reinforcement pull-out tests. The results in Objectives 1 to 3 were used to obtain AAM mixes for these tests, which were compared to OPC concrete with similar properties.

1.3 Report Layout

The report consists out of seven chapters. The chapter that follows, Chapter 2, is a theoretical background on AAMs, providing fundamental knowledge required to understand AAMs. Previous research that was done on the mechanical properties of AAMs are also included in this chapter.

Chapter 3 provides the structural aspects of reinforced concrete. In this chapter the general material properties for reinforced concrete are given, followed by typical reinforced concrete behaviour in terms of flexure, ductility, cracking and bond.

The experimental design is provided in Chapter 4. The test preparations, test setups and methods, material specifications and mix designs are included in this chapter.

Chapter 5 presents the results that was obtained for the mechanical properties of AAMs. Results on the workability, compressive strength, density, elastic modulus and stress-strain relationship are given and discussed.

The results that was obtained for the structural behaviour of reinforced AAMs is presented in Chapter 6. Results on the beam test and pull-out test are given and discussed.

Chapter 7 concludes the findings documented in this research and also provides recommendations for future studies.

Chapter 2

Alkali activated materials (AAMs)

Alkali activated materials (AAMs) are a new generation of alternative construction materials, which are formed through the alkali activation of clinker-free binder materials, such as fly ash and slag. Unlike Ordinary Portland cement (OPC), the production of AAMs is associated with low energy consumption and low carbon dioxide (CO_2) emissions. In this chapter a background to AAMs is given, which provides the required knowledge to understand AAMs. Previous research that was done on the mechanical properties of AAMs are also included in this chapter.

2.1 Background of AAMs

2.1.1 History

The earliest research done on AAMs was considered to be by R. Feret in 1939 and A.O. Purdon in 1940, who worked on the activation of slags. However, it was not until V.D. Glukhovsky presented so called soil silicates in 1959 that a theoretical basis of alkaline cements was established. Glukhovsky also emphasized the difference between the soil silicates and previous works, with the former acting as a structure forming component, producing zeolitic materials containing alkalis and the latter being an accelerator for the reactivity of slag, producing calcium silicate hydrate (C-S-H) and portlandite (Adam, 2009; Roy, 1999). A new type of material, very similar to the alkaline binding system, was introduced in 1979 by Davidovits. The term 'geopolymer' was adopted for these solid materials which were produced by an alkaline solution reacting with an aluminosilicate powder. The development of these materials were originally to find an alternative fire-resistant binding material after several fires occurred in Europe, which led to the material being used for applications such as fire protection coating of cruise ships, thermal protection of wooden structures etc. The main application of geopolymers shifted to the construction industry, after it was found that reliable, high-performance geopolymer concrete can be obtained when fly ash was alkaline activated (Provis et al., 2009). Detailed historical lists with the above mentioned milestones and numerous others are presented in Li et al., (2010) and Roy, (1999).

2.1.2 Terminology

There are several names and terms used to describe essentially the same material, here referred to as AAMs, including geopolymers, mineral polymers, alkali ash material, soil silicates, F-concrete, zeocements, and a variety of others. This can create confusion among researchers who are not familiar with AAMs (Provis et al., 2014). For the purpose of this study, the terms 'alkali activated material (AAM)' and 'geopolymer' are clarified.

The term alkali activated material (AAM) is considered to be the broadest classification for these type of binder systems resulting from an alkali metal source reacting with a solid silicate powder (binder material). The solid powders can consist of calcium silicate such as conventional clinkers being alkali activated, or more aluminosilicate-rich precursors for instance fly ash or metakoalin. The alkali activation of the solid powders require an alkali source which provides alkali metal cations, increase the reaction mixture's pH and speed up the dissolution of these solid precursors. Soluble substances that can be used for these purposes include alkali hydroxides, silicates, carbonates, sulfates, aluminates or oxides. The pH can also be elevated by alkaline earth compounds, normally a reaction between Class C Fly ashes and water. However, these binder systems are not included in the definition for AAMs (Provis et al., 2014).

Geopolymers are referred to as a subset of AAMs, where aluminosilicates are predominantly present in the highly coordinated binding phase. Therefore, the binder materials have very low amounts of calcium content in order to form amorphous zeolite network (three-dimensional tetrahedral) structures instead of crystalline chains typically found in C-S-H. The binder materials include low calcium fly ash (Class F) and natural clays, which are activated by alkali hydroxide and alkali silicate. The reaction process when these materials are alkali activated, is defined as polymerisation (Hardjito, 2005; Provis et al., 2014).

2.1.3 Classification

As mentioned previously, AAMs are binder systems consisting of solid silicate powders activated by an alkali metal source. The activation of AAMs can be classified into two main groups:

1. In the first group, calcium-rich binder materials such as blast furnace slag (BFS), are activated with mild alkaline solutions. The main reaction product in these systems is a calcium silicate hydrate gel, with aluminium taken up in the structure (C-A-S-H) (Li et al., 2010; Roy, 1999). This group of AAMs is referred to as high calcium activated systems.

2. The second group is considered to be the activation of aluminosilicate binder materials such as metakaolin or Class F fly ash, with medium to high alkaline solutions. This reaction leads to the formation of zeolite like polymers as the end product. Geopolymers fall under this class of AAMs (Li et al., 2010). This group of AAMs is referred to as low calcium activated systems.

A more detailed discussion on the reaction mechanisms and products that form in high calcium- and low calcium activated systems follows in the next section.

2.2 Reaction mechanisms and products

Over the past few years, a number of different types of AAMs have been developed. These AAMs differ in the binder material used, as well as the activation source. As mention, all of the different AAMs can be grouped into two categories, depending on the nature of the binder material. The two groups of AAMs include high calcium activated systems and low calcium activated systems. The reaction mechanisms during the activation of the binder material, together with the products that form after activation, differs in each. There is also a third type of alkaline activation that could occur, namely the combination of the preceding two. This is a result of the activation of materials with high amounts of calcium, as well as silica and aluminium (Garcia-Lodeiro et al., 2015). In this section, the reaction mechanisms and the resulting products that form for each of these systems are discussed.

2.2.1 High calcium activated systems

High calcium activated systems are prepared with calcium- and silicon-rich binder materials (SiO_2 + $CaO > 70\%$). The most common binder material used for these systems is slag, specifically blast furnace slag, a by-product of steel production (Garcia-Lodeiro et al., 2015). The reaction mechanism of slag based AAMs is governed by alkali hydration of slag, which corresponds to a heterogeneous reaction process with several steps. These steps include: the dissolution of slag particles; nucleation and growth of initial solid phases; mechanical binding of these initial solid phases; and the continued reaction through chemical equilibrium and diffusion over time. The steps can be summarised into the destruction of slag which is followed by the polycondensation of the reaction products (Palomo et al., 1999; Provis et al., 2014).

The alkaline activation of slag can be illustrated by a series of reactions as follow:

$$\equiv Si{-}O^{-} + R^{+} \longrightarrow \equiv Si{-}O{-}R$$

$$\equiv Si{-}O{-}R + OH^{-} \longrightarrow \equiv Si{-}O{-}R{-}OH^{-}$$

$$\equiv Si{-}O{-}R{-}OH^{-} + Ca^{2+} \longrightarrow \equiv Si{-}O{-}Ca{-}OH + R^{+}$$

In the initial phase of hydration, the alkaline cation (R^{+}) merely acts as catalyser, via the cationic exchange with Ca^{2+} ions (Garcia-Lodeiro et al., 2015). The nature of the anion in the solution also plays an important role in regards with the reaction rate during activation (Fernández-Jiménez et al., 2003b). Figure 2.1 demonstrates the typical reaction mechanism.

It has also been perceived that the alkalis in slag based AAMs has a similar role to that in blended OPC-slag cements, namely the continuous supply of hydroxide ions (OH^{-}) in the system. After

the blended OPC-slag cement is mixed with water, a layer forms on the surface of the slag grains, which prevents further hydration of slag. The $Ca(OH)_2$ from the hydration of OPC, provides an alkaline environment to break this layer down. The $Ca(OH)_2$ then also reacts with the silica from the slag to form C-S-H, the same hydration product generated in OPC cement (Adam, 2009; Grieve, 2009). In slag based AAMs the alkalis breaks the slag bonds (Ca-O, Si-O-Si, etc.), and then takes part in the reaction to form an aluminium-substituted C-A-S-H type gel as the main reaction product (Li et al., 2010; Provis et al., 2014).

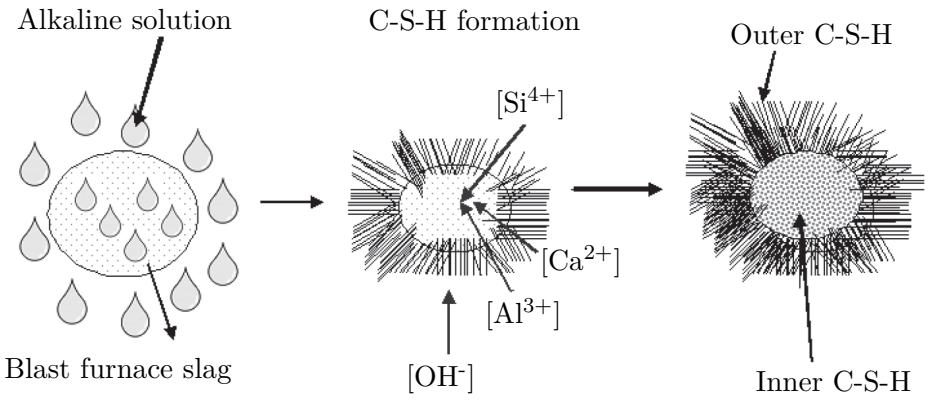

Figure 2.1: Typical reaction mechanism for alkali-activated slag (Garcia-Lodeiro et al., 2015)

This main reaction product formed in high calcium activated systems together with the secondary products are very similar to that formed in normal OPC cements. In OPC cements, the main reaction product is C-S-H, which is responsible for the mechanical properties of the cement. The reaction product in high calcium activated systems differs due to the aluminium that is taken up in the C-S-H structure, as well as the lower CaO/Si_2O ratio. Secondary products that form in OPC cements include: portlandite ($Ca(OH)_2$), ettringite and calcium monosulfoaluminate (AF_m and AF_t), while hydrotalcite-, C_4AH_{13}-, C_4AcH_{11}- and $C_8Ac_2H_{24}$-type phases have been observed in high calcium activated systems (Grieve, 2009; Combrinck, 2015b; Garcia-Lodeiro et al., 2015). The reaction products of OPC cement and (high- and low calcium) AAMs are compared in Table 2.1. Ben Haha et al., (2011) also found that as the reaction advances some of the Ca^{2+} in the C-A-S-H could be replaced by Na^+, which leads to C-(N)-A-S-H gel formation. Some similarities can be observed between the SEM images of the slag-based AAM and OPC cement shown in Figure 2.2.

Table 2.1: Reaction products of OPC cement and (high- and low calcium) AAMs (Garcia-Lodeiro et al., 2015)

Binder Type		**OPC**	**AAM**	
			High calcium system	**Low calcium system**
Reaction product	**Primary**	C-S-H	C-A-S-H	N-A-S-H
	Secondary	$Ca(OH)_2$ AF_m AF_t	Hydrotalcite C_4AH_{13} C_4AcH_{11} $C_8Ac_2H_{24}$	Zeolites: Hydroxysodalite zeolite P, Na-chabazite, zeolite Y
C = CaO, S = SiO_2, A = Al_2O_3, N = Na_2O, H = H_2O, c = CO_2				

The structure and composition of the C-A-S-H and the secondary products that form, are highly dependent on the composition of the starting materials, the type and concentration of the activator, curing conditions and the pH environment. An ordered crystalline structure is obtained when sodium hydroxide is used to activate slag, while the crystallinity remains low when sodium silicate is used as activator. This could be attributed to the higher amount of silicate species available in the pore solution of silicate-activated systems (Grieve, 2009; Provis et al., 2014). Schilling et al., (1994) established that the aluminium uptake increased at higher temperatures and humidity, while Fernández-Jiménez et al., (2003c) showed that gels with longer linear chains are obtained with more aluminium content.

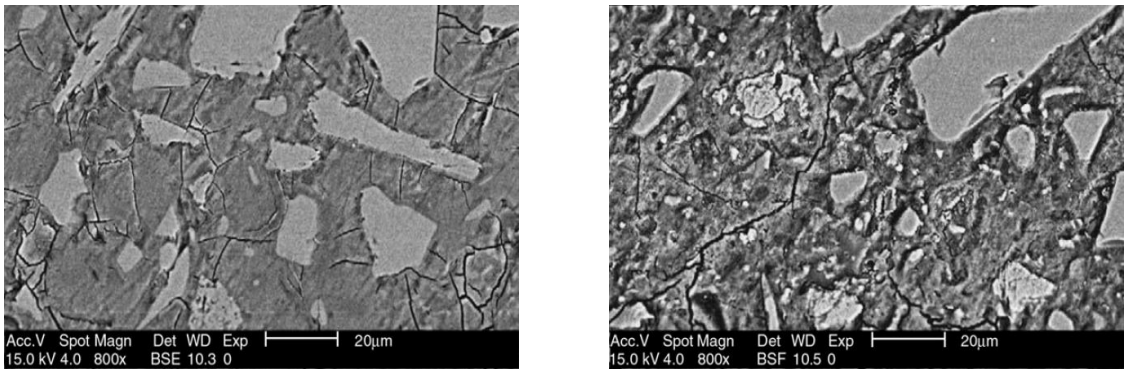

(a) Slag-based AAM (b) OPC cement

Figure 2.2: SEM images (Li et al., 2010)

2.2.2 Low-calcium activated systems

Low calcium activated systems are activated by aluminium- and silica-rich binder materials, containing no or a very low amount of calcium content. These materials are typically class F fly ash or metakaolin. A general model consisting of three stages was proposed to describe the reaction mechanism of low calcium activated systems. The three stages include: (a) destruction-coagulation; (b) coagulation-condensation; and (c) condensation-crystallisation. This reaction process is referred to as geopolymerisation (Adam, 2009; Garcia-Lodeiro et al., 2015).

The first stage of the geopolymerisation process starts directly after the alkaline activator comes into contact with the binder material, during initial mixing. The hydroxide (OH^-) ions in the alkaline activator breaks the Si-O-Si, Al-O-Al, and Si-O-Al bonds within the amorphous phase of the binder material. This is a result of the bonds being weakened by the OH^- ions redistributing their electronic density around the silica and aluminium atoms. The silica and aluminium ions released from the broken bonds into the solution, then form species containing Si-OH and Al-OH groups. This stage is also referred to as the dissolution of silica and aluminium ions within virtuous phase of the binder material (Fernández-Jiménez et al., 2006c). The rate at which dissolution occurs is highly dependent on the pH of the alkaline solution and the composition of the binder material (Li et al., 2010).

The dissolution of silica and aluminium within fly ash is demonstrated in Figure 2.3. The process starts with the alkaline solution attacking the surface of the particles, forming cavities in the particle walls. Therefore, the smaller particles within the broken particle is exposed, causing chemical attack from the inside out as well as from outside in. This process will continue until the entire ash particle is consumed.

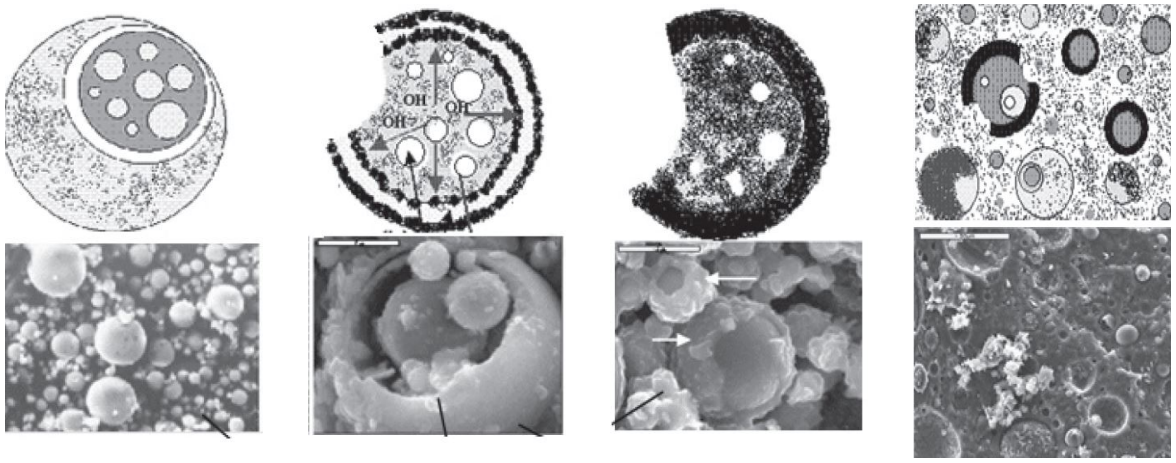

(a) (b) (c) (d)

Figure 2.3: Model for the alkaline activation of fly ash (Garcia-Lodeiro et al., 2015)

In the second stage, the ionic species accumulate and interacts with one another in the solution to form coagulated structures. This is a condensation reaction between the silica monomers, forming dimers (Si-O-Si bonds). The dimers then also react with other monomers, which builds polymers in all directions. The alumina monomers also participate in the reaction by replacing the silicon tetrahedra. The OH^- ions are required as the catalyst during this stage (Garcia-Lodeiro et al., 2015; Khale et al., 2007). The second stage can be represented by the following reaction:

$$n(Si_2O_5, Al_2O_2) + nSiO_2 + nH_2O \xrightarrow{\text{NaOH, KOH}} n(OH)_3\text{-}Si-O-\overset{(-)}{\underset{|}{Al}}\underset{(OH)_2}{}-O-Si-$$

The coagulated polymer structures formed in the second stage further reacts with each other and with the monomers in the third stage, producing a condensed interlocking network structure. The products that form during the last stage of the reaction is dependent on the composition of the binder material, the type of alkaline activator and the curing conditions. A heat source is generally required for this hardening reaction (Garcia-Lodeiro et al., 2015; Van Chanh et al., 2008). The reaction during the third stage is demonstrated as follow:

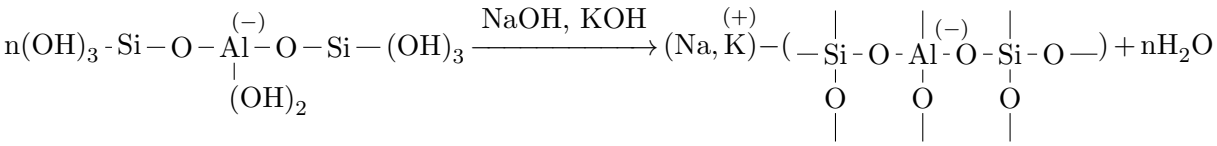

From these reactions, it is evident that the water merely acts as a reagent. During the last stage of the geopolymerisation process, the water is expelled by evaporation through the nano-pores of the matrix. Therefore, the water does not form part of the reaction process or the final reaction product, but does provide workability to the fresh mixture. This is in contrast with the hydration process of OPC concrete, where the water takes part in the chemical reaction (Rangan, 2008).

Apart from the role of water in the reaction process, the reaction products of low calcium AAMs are also very different to that of normal OPC concrete. As mentioned in the previous section, the main reaction product in OPC concrete is C-S-H, while an amorphous alkaline aluminosilicate hydrate, known as N-A-S-H gel, is the main reaction product in low calcium AAMs (Garcia-Lodeiro et al., 2015). The term poly(sialate), an abbreviation for silicon-oxo-aluminate, is also used for this reaction product. The poly(sialite) network consist of Si^{4+} and Al^{3+} ions which are alternately linked together by sharing oxygen ions. The negative charge of Al^{3+} in the IV-fold coordination is balanced by the positive ions (Na^{+}) (Davidovits, 1989).

Poly(sialate) has the following empirical formula:

$$M_n(\text{-}(SiO_2)_z\text{-}AlO_2)_n.wH_2O$$

Where M is the alkali element such as sodium or potasium; n is the degree of polycondensation; z is a value between 1 and 3; and w is the hydration extent. Poly(sialates) are chain and ring polymers which range from semi-crystalline to amorphous (Davidovits, 1989; Davidovits, 1994). Three types of poly(sialates) have been identified by Davidovits as shown in Figure 2.4.

The secondary products that form in low calcium AAMs are hydroxysodalite, zeolite P, Na-chabazite, zeolite Y and faujasite. These products are silicate minerals that form part of the zeolite family (Garcia-Lodeiro et al., 2015). Both the main and secondary products of low calcium AAMs are compared to normal OPC concrete and high calcium AAMs in Table 2.1.

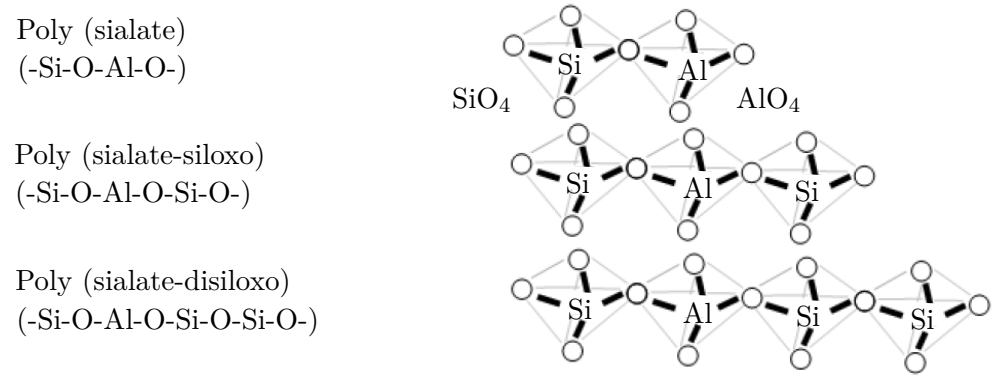

Figure 2.4: Chemical structure of poly(sialates) (Davidovits, 1994)

2.2.3 Combined systems

A combination of the two alkali activation systems is possible when the binder material used, has a CaO, SiO_2, and Al_2O_3 content of over 20 % each. High calcium (Class C) fly ash or blended low- and high calcium sources are normally used as these binder materials (Garcia-Lodeiro et al., 2015; Provis et al., 2014). In these systems, the geopolymerisation process can be considered as the main reaction mechanism. The geopolymeric gel that is formed is depended on the availability of dissociated silicate $SiO_n(OH)_{4-n}^{n-}$ and aluminate $Al(OH)^{4-}$ monomers present in the alkaline medium. Thus, the geopolymerisation process is governed by the dissolution of silica and aluminium from the binder source. However, the governing reactions become more complex with soluble calcium present in the alkaline medium (Yip et al., 2008). Yip et al., (2008) suggested two ways to which calcium will take part in the reaction:

1. The calcium could precipitate as calcium hydroxide ($Ca(OH)_2$). During the mixing of the AAM constituents, the dissolved Ca^{2+} reacts with OH^- in the water, forming $Ca(OH)_2$. This will lower the the alkalinity of the medium and, as a result, enhance the dissolution of silica and aluminium from the binder materials. The $Ca(OH)_2$ further reacts with CO_2 in the atmosphere, which forms calcite ($CaCO_3$). This reaction is considered as the main hardening mechanism. The above process occurs in combination with the dissolution of silica and aluminium (Astutiningsih et al., 2005).

2. The calcium could also react with the dissolved silica and aluminium species, therefore interfering with the formation of the geopolymeric gel (Yip et al., 2008). Yip et al., (2003) found that the calcium would take part in the formation of C-S-H gel, a secondary product to the amorphous and semi-crystalline geopolymeric gel that forms. The C-S-H gel contributes to improved compressive strengths and accelerated setting times. However, these products do not develop separately, but interact and undergo structural change during the reaction process (Garcia-Lodeiro et al., 2015).

The process that occurs, as well as the reaction products that form are highly dependent on the alkalinity (pH) of the system and the dissolved Ca, Si and Al content in the alkaline medium. A study done by Garcia-Lodeiro et al., (2011) showed that N-A-S-H-type gels were modified in the presence of dissolved calcium. The sodium is partially replaced by calcium resulting in the formation of (N,C)-A-S-H gels. It was also found that the formation of C-A-S-H gels are favoured over N-A-S-H gels, in the presence of sufficient calcium and high pH values, as shown in Figure 2.5. At low alkalinities, the co-precipitation of both geopolymeric gel and C-S-H gel is possible, providing acceptable mechanical properties (Yip et al., 2003; Yip et al., 2008). Puertas et al., (2000) also found reaction products such as hydrocalcite ($Mg_6Al_2CO_3(OH)_{16}.4H_2O$), pirssonite ($Na_2Ca(CO_3).2H_2O$) and calcite in the combined systems.

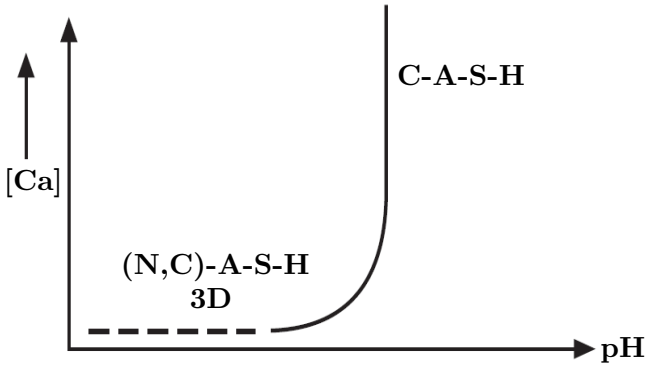

Figure 2.5: Model proposed to define N-A-S-H gel stability in terms of pH and calcium content (Garcia-Lodeiro et al., 2011)

2.3 Constituents of AAMs

AAMs consist out of a binder material that is alkali activated, together with coarse and fine aggregate. As in normal OPC concrete, the aggregate comprises of about 65 to 80 % of the mass. It is also considered that the properties of the aggregate, such as grading, angularity and strength to have the same effect as in the case of normal OPC concrete (Lloyd et al., 2010; Combrinck, 2015a). The binder materials and the alkaline activators that are used to make AAMs are specified in this section.

2.3.1 Binder material

There are several materials that have been instigated and used as the binder material for AAMs. These materials include natural minerals such as kaolinite and clays, as well as by-products such as slag, silica fume, fly-ash, rice-husk ash and red mud (Motorwala et al., 2013). Davidovits, (2013) categorised these binder materials into slag-, rock-, fly-ash- and ferro-sialate-based AAMs. The use of the binder material depends strongly on the following factors: availability, cost, type of application, and specific demand of the end user. Due to these factors, the predominantly

used binder materials are slag and fly-ash (Lloyd et al., 2010), which are further discussed in the following sections:

2.3.1.1 Slag

The first AAMs was developed by using slag as a binder material. This was done in the 1980's through the research of Davidovits and Saywer at Lone Industries in the USA. The research resulted in a type (K,Na,Ca)-poly(sialate), an invention well known today as Parament® cement (Davidovits, 2013). Due to the rapid strength gain of Paramennt® (20 MPa after 4 hours), it is ideal for repairing airline runways made of concrete, industrial pavements, and highways (Geopolymer Institute, 2013).

Slag is a by-product that is formed during the manufacturing of steel. During this process, additives (iron ore, coke ash, limestone etc.) are added to iron ore to remove the impurities. This results in the formation of a molten slag that floats on top of the molten iron. The slag is then separated from the iron and cooled (Slag Cement Association, 2002; Li et al., 2010). The method used to cool the molten slag determines the slag products that form. A crystalline slag is formed when cooled very slowly, while the slag is glassy with rapid cooling. The formed slag consist primarily of silicates, aluminosilicates and calcium-alumina-silicates, which depend on the composition of the iron ore (Grieve, 2009; Lewis, 1992).

Different types of slags are obtained depending on what process is used to manufacture the iron ore. The blast-furnace process produces the most generally used slag type, namely blast furnace slag. A ground granulated blast-furnace slag (GGBS) is obtained when the hot slag is quenched with water and milled to a fine powder. Another type of slag is produced with the more environmental friendly Corex process. This slag is referred to as corex slag, which are said to be more reactive than blast-furnace slag (Grieve, 2009; Siemens, 2011). These slags are typically used as partial replacement for or additive to OPC.

OPC has been partially replaced by slag for more than a century. This is done in order to reduce the carbon dioxide emissions as well as reducing the life-cycle costs of a concrete structure, due to the improved durability characteristics. Other benefits associated with slag replacement include:

- Better concrete workability
- Easier finishability
- Higher compressive and flexural strength
- Improved resistance to chemical attack

(Slag Cement Association, 2002)

The phase composition and the glass structure of slag is the main factor that contributes to the reactivity thereof in AAMs. It has been reported that the glass content (CaO, SiO_2, Al_2O_3 and MgO) should exceed 90 %, but good results have also been obtained from slags with low glass content (30-65 %). This demonstrates that although the glass structure is essential to the

reactivity, there is no exact correlation between the two. However, a direct relationship has been proven between the degree of depolymerisation (DP) and slag reactivity. This value typically ranges between 1.3 and 1.5, and can be calculated with the following equation (Garcia-Lodeiro et al., 2015; Li et al., 2010):

$$DP = \frac{n(CaO) - 2n(MgO) - n(Al_2O_3) - n(SO_3)}{n(SiO_2) - 2n(MgO) - 0.5n(Al_2O_3)} \tag{2.1}$$

The main properties that are required for the slag to be used in AAMs are as follow:

- A vitreous phase content of $>$ 85-95 %
- Granulated or pelletised
- Ground to a specific surface of 400-600 m^2/kg
- Small particle size of less than 20 μm for fast reactivity

(Duxson, 2009; Garcia-Lodeiro et al., 2015)

2.3.1.2 Fly ash

In 1997, Silverstrim et al., (1997) and Van Jaarsveld et al., (1997) further built on the research and work conducted on slag-based geopolymeric cements as well as on the synthesis of zeolites from fly ashes. This resulted in the development of geopolymeric fly ash-based cements.

Fly ash is defined by the American Concrete Institute (ACI) Committee 116R as a finely divided residue that is formed during the combustion of coal. The residue is then transported from the combustion zone to the particle removal system via flue gasses (ACI Committee 232, 2002). A Dust collection system is used to remove the fly ash from the combustion gases before they are released into the atmosphere. This is done mechanically or through the use of electrostatic precipitators (Motorwala et al., 2013).

Fly ash is mainly composed of fine oxides particles (SiO_2, Al_2O_3, Fe_2O_3 and CaO) and compounds such as quartz, hematite, mullite and amorphous particles. This chemical composition of fly ash is determined by the type of coal used and relative amounts of incombustible matter within the coal (Temuujin et al., 2009). A high calcium fly ash (typically containing more than 20 % CaO) is produced from lignite or sub-bituminous coals, while a low calcium fly ash (containing less than 10 % CaO) is produced from anthracite and bituminous coals. High- and low calcium fly ash are categorised by ASTM Standard C618, (2012) as Class C and Class F fly ash, respectively (Adam, 2009; ACI Committee 232, 2002). Class F fly ash was used in this study, as it is the only type of fly ash that is produced in South Africa.

Fly ash has been widely used to partially replace OPC and in turn produce more environmentally friendly concrete. The fly ash acts as an artificial pozzolan, where the silicon dioxide within the fly ash reacts with the calcium hydroxide from the hydration process of cement, forming C-S-H

gel (Grieve, 2009). The addition of fly ash to cement has been studied for many years and it is generally agreed that the concretes properties are improved as follow:

- The workability of the fresh concrete is improved as a result of the spherical shaped particles of fly ash, as shown in Figure 2.6
- The spherical particles also enables one to reduce the amount of water and therefore less bleeding is experienced
- The reduction in water, together with the small particle size of fly ash ensures better packing of particles. This produces a dense and durable concrete with improved compressive strengths
- CO_2 emissions are reduced
- Reduces drying shrinkage

(Motorwala et al., 2013; Provis et al., 2009)

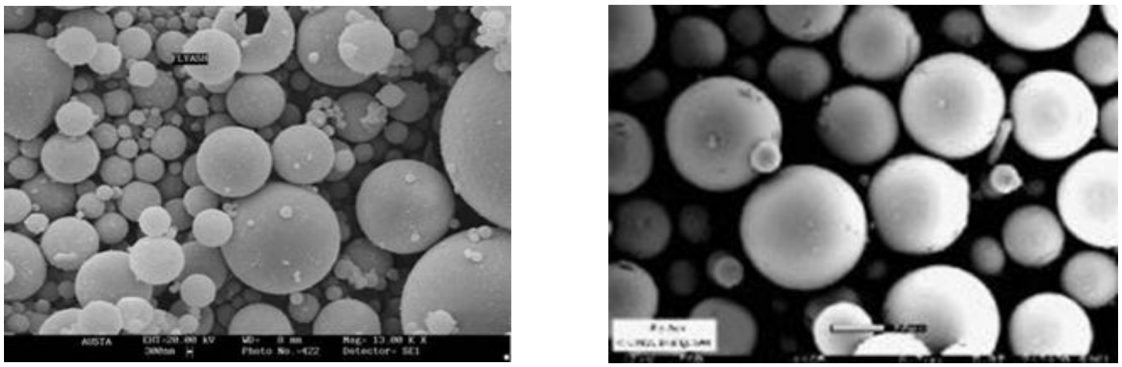

(a) Ungraded fly ash (b) Graded fly ash

Figure 2.6: Spherical shape of fly ash (Motorwala et al., 2013)

Fernández-Jiménez et al., (2003a) did a comprehensive study on a large number of different fly ashes and concluded that a Class F fly ash must meet several requirement for it to be suitable in the use of AAMs. These requirements include:

- Unburned material, also referred to as loss of ignition (LOI), must be lower than 5 %
- Fe_2O_3 content less than 10 %
- CaO content less than 10 %
- Reactive SiO_2 content between 40 % and 50 %
- Between 80 % and 90 % of the particles must be smaller than 45 μm
- The vitreous phase content must be greater than 50 %
- A $[SiO_2]_{reactive}/[Al_2O_3]_{reactive}$ ratio larger than 1.5

(Fernández-Jiménez et al., 2003a; Fernández-Jiménez et al., 2006c)

2.3.2 Alkaline activators

There is a variety of alkaline solutions that can be used to activate the binder material of AAMs. These activators can be classified according to their chemical composition into six groups:

1. Caustic alkalis: MOH;
2. Non-silicate weak acid salts: M_2CO_3, M_2SO_4, M_3PO_4, MF, etc;
3. Silicates: $M_2O.nSiO_2$;
4. Aluminates: $M_2O.nAl_2O_3$;
5. Aluminosilicates $M_2O.Al_2O_2.(2\text{-}6)SiO_2$; and
6. Non-silicate strong acid salts: M_2SO_4.

(Shi et al., 2006)

From all of the above, sodium silicate (Na_2SiO_3), sodium hydroxide (NaOH), sodium carbonate (Na_2CO_3) and sodium sulfate (Na_2SO_4) are the activators which are normally used due to availability and economic reasons (Adam, 2009; Shi et al., 2006). Potassium is also often used as the soluble alkali metal, instead of sodium. However, the applications of potassium compounds are limited due to their availability and cost (Lloyd et al., 2010; Shi et al., 2006). Xu et al., (2000) also found that a lower dissolution rate is obtained with potassium compounds than with sodium compounds.

Previous research showed that promising results are obtained with a combination of sodium hydroxide and sodium silicate as the alkaline activator. The addition of sodium silicate solution to the sodium hydroxide solution, improves the reaction between the binder and the alkali solution (Adam, 2009; Lloyd et al., 2010; Xu et al., 2000).

Sodium hydroxide in combination with sodium silicate was used as the alkaline activator in this study. Sodium carbonate was also used as an alternative alkaline activator. The properties, production and application of these three activators are discussed in the following sections.

2.3.2.1 Sodium silicate

Sodium silicate solution, also known as waterglass or liquid glass, is a thick, viscous, colourless to greenish substance. Commercial sodium silicates are generally specified according to the weight ratio of silica- to sodium oxide (SiO_2/Na_2O ratio), which can vary between 1.6 and 3.85, as well as the water content. The viscosity of sodium silicate increases with the SiO_2/Na_2O ratio, at a given constant silica content. Sodium silicate solutions are also soluble in water (Lagaly et al., 2000; Shi et al., 2006).

Sodium silicate is produced by dissolving a glass melt, typically silica sand. This is done either at atmospheric pressure as it is drawn from the melting furnace or under steam pressure, after

cooling and crushing. Another method to produce sodium silicate solution, which is used to a lesser extent, is to dissolve the silica sand in caustic liquid (Lagaly et al., 2000; Shi et al., 2006).

Typical applications of sodium silicate include: detergents and cleaning products; adhesives; surface coatings; paper deinking and bleaching; water treatment; and stabilisation of soils (Lagaly et al., 2000).

2.3.2.2 Sodium hydroxide

Sodium hydroxide, also referred to as caustic soda due to its corrosive action, is an inorganic compound with a white crystalline appearance. Apart from the prepared solutions, sodium hydroxide is also commercially available in four solid forms: pellets, flakes, beads and compounder's. All of these solid forms have the same chemical composition, with only the particle size that differ. The dissolution of sodium hydroxide in water is a highly exothermic reaction in which a large amount of heat is released. Both the heat of dissolution and the viscosity increases with an increase of concentration (Shi et al., 2006; Kurt et al., 2006).

Sodium hydroxide is produced by the electrolysis of sodium chloride brine; yielding sodium hydroxide solution, chlorine and hydrogen. This electrolytic process occurs either in a membrane cell or diaphragm cell. The solid sodium hydroxide is obtained by evaporating the water from the sodium hydroxide solution (Occidental Chemical Corporation, 2013; Kurt et al., 2006).

Sodium hydroxide is used in many industries, mostly as a strong chemical base in the manufacture of pulp and paper, textiles, water treatment, soaps and detergents (Kurt et al., 2006).

2.3.2.3 Sodium carbonate

Sodium carbonate, also known as washing soda or soda ash, is the neutral sodium salt of carbonic acid. Pure sodium carbonate is a white, odourless powder that is hygroscopic (absorbs moisture from the air). Sodium bicarbonate ($NaHCO_3$) is formed when CO_2 is absorbed into a sodium carbonate solution. The solubility of sodium carbonate is highly dependent on the temperature (Shi et al., 2006; Thieme, 2000).

Sodium carbonate is either obtained from natural sources or produced from chemical processes. Natural sodium carbonate-bearing minerals are generally located in shallow, non-marine alkaline lake sand marches. The production of sodium carbonate is generally done with the Solvay process (Ammonia-Soda Process), which converts sodium chloride into sodium carbonate using ammonia. The Leblanc process is another process used to produce sodium carbonate by using salt, sulphuric acid, limestone and coal (Thieme, 2000).

Sodium carbonate is an important material for the following industries: chemical; detergent and soap; pulp and paper; textile; iron and steel; glass and silicate; and food (Thieme, 2000).

2.4 Mechanical properties of AAMs

A large amount of research has already been done on the mechanical properties of AAMs. From these studies it has been shown that AAMs exhibit promising or even superior mechanical properties to that of OPC concrete. Several of the important properties are:

- Heat resistance
- Resistance to chemical attack
- Creep and drying shrinkage
- Elastic modulus and Poisson's ratio
- Compressive strength
- Flexural and tensile strength
- Ductility
- Durability
- Workability
- Setting times

2.4.1 Typical mechanical properties

Several of the important mechanical properties of AAMs are listed in the previous section. The following properties are discussed in more detail in the following sections: heat resistance, chemical attack, creep and shrinkage, elastic modulus, Poisson's ratio, and the compressive strength.

2.4.1.1 Heat resistance

As mentioned in Section 2.1.1, geopolymers originated from research that was done on heat resistant materials after several fires broke out in France during the 1970's. It was found that the geopolymers performed well during the heat resistance tests; even better than OPC concrete (Davidovits, 1989). This is due to the different reaction processes and products that form between the two materials. Calcium silicate hydrate forms during the hydration process in OPC concrete, which tends to decompose when it is exposed to extreme temperatures. This negatively affects the other mechanical properties, for example decreasing the compressive strength. Due to the polycondensation process that occurs within geopolymers, the reaction product is a geopolymeric gel instead of calcium silicate hydrate. Unlike the calcium silicate hydrate, the geopolymeric gel is stable when exposed to high temperatures (Davidovits, 2013; Hager, 2013). However, it should be noted that if there is a significant amount of calcium present in the binder

material, hydrates are formed in conjunction with the geopolymeric gel. Thus, AAMs only exhibit exceptional heat resistance when the binder material has a low calcium content.

2.4.1.2 Chemical attack

Concrete deteriorates due to chemical reactions which are caused by chlorides, carbonation, sulphates, acids and water (Ballim et al., 2009). Studies have shown that AAMs generally perform well against chemical attack.

The chloride permeability and carbonation of AAMs were investigated by Bernal et al., (2011) and Bernal et al., (2012) and compared to that of OPC concrete. The chloride permeability was tested by measuring the total charge that was transferred through the specimens. It was found that the AAMs had a lower charge than OPC concrete, which corresponds to a reduced chloride permeability. A phenolphthalein indicator was used to determine the extent of carbonation after the specimens were exposed to a CO_2 environment. The AAM specimens were more susceptible to carbonation than OPC concrete, as shown in Figure 2.7. This is due to the high alkali content within AAMs (Bernal et al., 2011; Bernal et al., 2012).

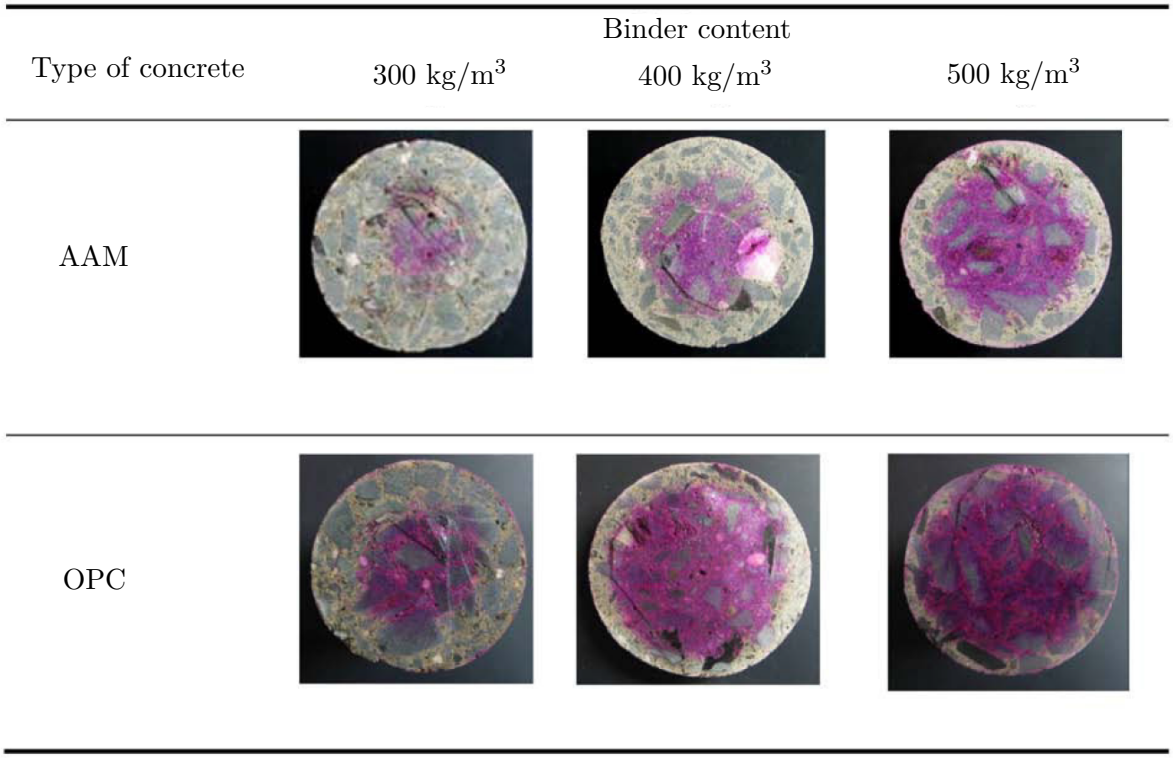

Figure 2.7: Transverse sections of carbonated concretes after 1000 h of exposure to a 1 % CO_2 environment, with the extent of carbonation revealed by a phenolphthalein indicator (Bernal et al., 2011)

Wallah et al., (2006) investigated chemical deterioration due to sulphate- and acid attack. No damage was observed to the surface of the AAM specimens exposed to sodium sulphate for a year. The sulphate exposed specimens also had no substantial mass loss or a decrease in the

compressive strength. The specimens that were exposed to sulfuric acid experienced some surface damage, mass loss and a decrease in compressive strength. However, the chemical deterioration of the AAM specimens was still less than that of the OPC concrete (Wallah et al., 2006).

2.4.1.3 Creep and drying shrinkage

Studies that investigated the creep and shrinkage of AAMs, found that these properties are dependent on parameters, such as the type and chemical composition of the constituents used, as well as the temperature and conditions used during curing. When compared to OPC concrete, the creep of AAMs is generally lower than OPC concrete, while the shrinkage is higher (Wallah et al., 2015).

The creep and shrinkage of slag based AAMs activated with different activators (sodium silicate, sodium hydroxide and sodium carbonate) was investigated by Collins et al., (1999). The AAMs were cured at ambient conditions. The creep for the AAMs were relatively low for the first few days, which increased after 112 days of loading to slightly higher values than that of OPC concrete. The AAMs activated with sodium hydroxide and sodium carbonate showed similar shrinkage to that of OPC concrete, while the AAMs activated with sodium silicate had more shrinkage (Collins et al., 1999).

Bakharev et al., (1999) also investigated the shrinkage of different activators used for slag based AAMs, cured at ambient temperatures. The sodium silicate solution as activator caused the largest amount of shrinkage, while all of the activators exhibited more shrinkage than that of OPC concrete. The study also revealed that the shrinkage increased with higher amounts of alkalis in the activators (Bakharev et al., 1999).

Fly ash-based AAMs, activated with sodium silicate and sodium hydroxide, was studied by Wallah et al., (2006). The creep and shrinkage was measured at ambient and heated curing conditions. Similar results were found between the AAMs cured at ambient temperatures and OPC concrete, while the heat curing caused very low creep and shrinkage within the AAMs. The drying shrinkage for the AAMs with heat curing and ambient curing is shown in Figure 2.8.

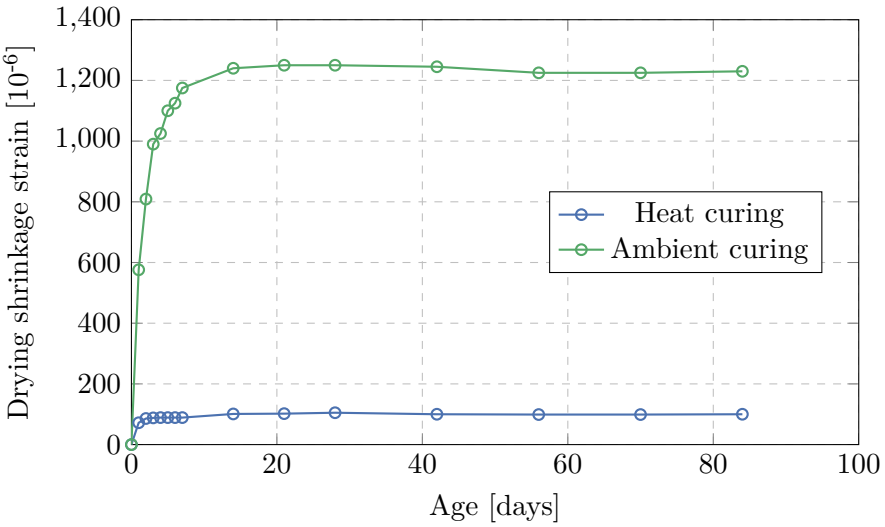

Figure 2.8: Drying shrinkage of heat cured and ambient cured specimens (Wallah et al., 2006)

The research on creep and shrinkage of AAMs is still limited and incomplete. Thus, more research is required to understand these mechanical properties and their influencing factors.

2.4.1.4 Elastic modulus and Poisson's ratio

It has been shown through previous research that the elastic modulus and the Poisson's ratio of AAMs are dependent on various factors, such as the composition of the constituents; the mix proportions; and curing conditions. The elastic modulus of AAMs is generally relatively low, while similar values to that of OPC concrete are obtained for the Poisson's ratio.

Barnard, (2014) investigated the effect of several parameters on the elastic modulus of AAMs, which consisted out of a combination of slag and fly ash as the binder and sodium silicate and sodium hydroxide as the alkali activator. The AAMs was cured at ambient curing conditions. The parameters that was changed include: the slag content; alkali solution replaced by water; sodium silicate to sodium hydroxide ratio; and the sodium hydroxide concentration. From these influencing parameters, it was found that the sodium hydroxide concentration had the largest influence on the elastic modulus, as shown in Figure 2.9. The elastic modulus ranged between 9.4 GPa and 23 GPa.

Fernández-Jiménez et al., (2006b) did a study on the elastic modulus of fly ash activated by only sodium hydroxide, as well as a combination of sodium hydroxide and sodium silicate. The elastic modulus for the sodium hydroxide as the only activator was 11.7 GPa, while the combination of sodium hydroxide and sodium silicate gave a value of 18.4 GPa. From this it can be concluded that the presence of sodium silicate improves the elastic modulus. Similar results were obtained in a study by Duxson et al., (2007), who used metakoalin as a binder to estimate what the effect of the Si/Al ratio is on the elastic modulus. The elastic modulus increased from approximately 2 GPa to 6 GPa after the Si/Al ratio was increased from 1.15 to 2.25.

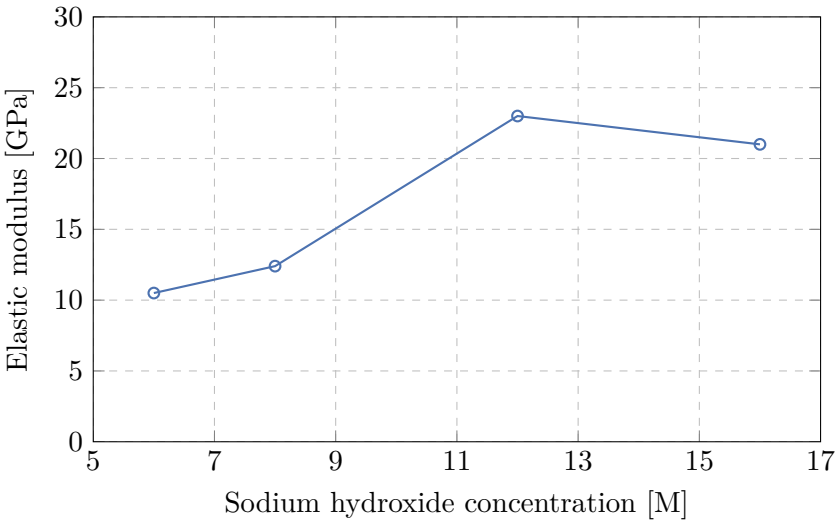

Figure 2.9: Effect of sodium hydroxide concentration on the elastic modulus (Barnard, 2014)

The elastic modulus and Poisson's ratio was determined in a study by Sofi et al., (2007). Fly ash and slag was used for the binder, which was activated by one or more of the following activators: sodium silicate, sodium hydroxide and sodium carbonate. The elastic modulus values ranged between 20 GPa and 38 GPa, which was lower than the values obtained from the model proposed by the Australian Standards AS 3600 to estimate the elastic modulus of OPC concrete. The Poisson's ratio values for the AAMs varied between 0.23 and 0.26, which is slightly higher than Poisson's ratio values for OPC concrete (Sofi et al., 2007).

Hardjito, (2005) also investigated the elastic modulus and Poisson's ratio of a fly ash-based AAM, activated with both sodium hydroxide and sodium silicate. However, elevated temperatures was used for curing. The results for the elastic modulus of the AAM indicated that, similar to OPC concrete, the elastic modulus also increased as the compressive strength increased. The elastic modulus varied between 23 GPa and 31 GPa. The Poisson's ratio was the same for both the AAM and OPC concrete, ranging between 0.12 and 0.16. These results are shown in Table 2.2 (Hardjito, 2005).

Table 2.2: Elastic modulus and Poisson's ratio (Hardjito, 2005)

Mean compressive strength [MPa]	Age of concrete [Days]	Modulus of elasticity [GPa]	Poisson's ratio
89	90	30.8	0.16
68	90	27.3	0.12
55	90	26.1	0.14
44	90	23	0.13

It is thus evident that the elastic modulus of AAMs are generally significantly lower than OPC concrete. However, with the correct curing conditions, mix proportioning and activator properties, the elastic modulus could be improved to obtain similar values to that of OPC concrete. The Poisson's ratio was found to be in the same range as OPC concrete.

2.4.1.5 Compressive strength

It has been established through numerous studies that AAMs are able to achieve comparable or even superior compressive strengths to OPC concrete. However, the compressive strength of AAMs is dependent on a number of factors (Nath et al., 2012; Hardjito et al., 2004; Barnard, 2014). Some of the factors that affect the compressive strength of AAMs include: curing temperature; curing time; calcium content; type of alkali activator; activator concentration; activator dosage (% Na_2O/binder); activator modulus (SiO_2/Na_2O ratio); and water content. These influencing factors are discussed in more detail in the following section.

2.4.2 Factors influencing mechanical properties

Compared to the water to binder ratio for OPC concrete, AAMs have considerably more factors that influence the compressive strength. The curing temperature, curing time, calcium content, type of alkali activator, activator concentration, activator dosage (% Na_2O/binder), activator modulus (SiO_2/Na_2O ratio), and the water content as influencing factors are discussed in this section.

2.4.2.1 Curing temperature

The curing temperature plays an important part in the strength development of AAMs. Heat curing is required to accelerate the geopolymerisation process and obtain high compressive strengths (Hardjito et al., 2004). Although the geopolymerisation process is not as sufficient at low temperatures, Nath et al., (2012) demonstrated that it is possible to obtain adequate strength with ambient curing. Experimental research by Hardjito et al., (2005), found that there is no significant change in strength with curing temperatures higher than 60 °C. The strength increase with higher curing temperatures are demonstrated in Figure 2.10.

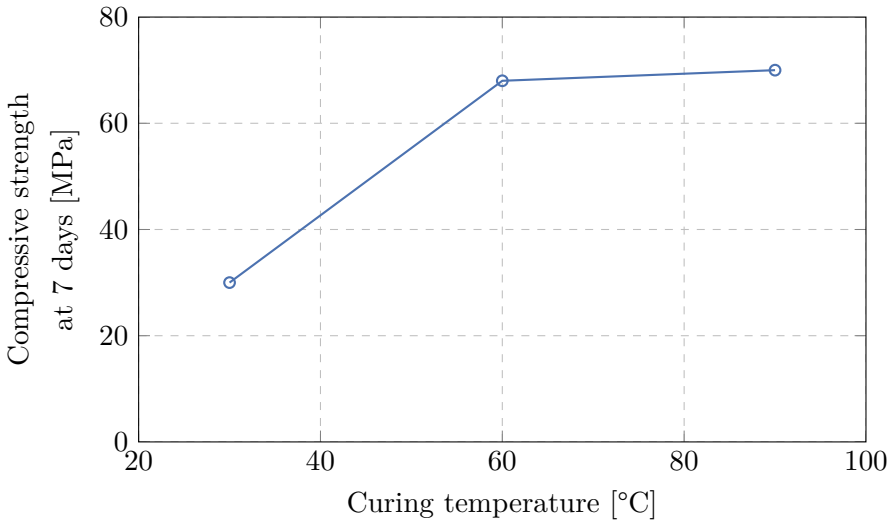

Figure 2.10: Effect of curing temperature on compressive strength (Hardjito et al., 2004)

2.4.2.2 Curing time

The geopolymerisation process is also improved when the duration of initial heat curing is extended, which yields higher compressive strengths. However, Hardjito et al., (2004) indicated that the compressive strength does not significantly change after 48 hours of curing at 60 °C. The results of Hardjito et al., (2004) are shown in Figure 2.11.

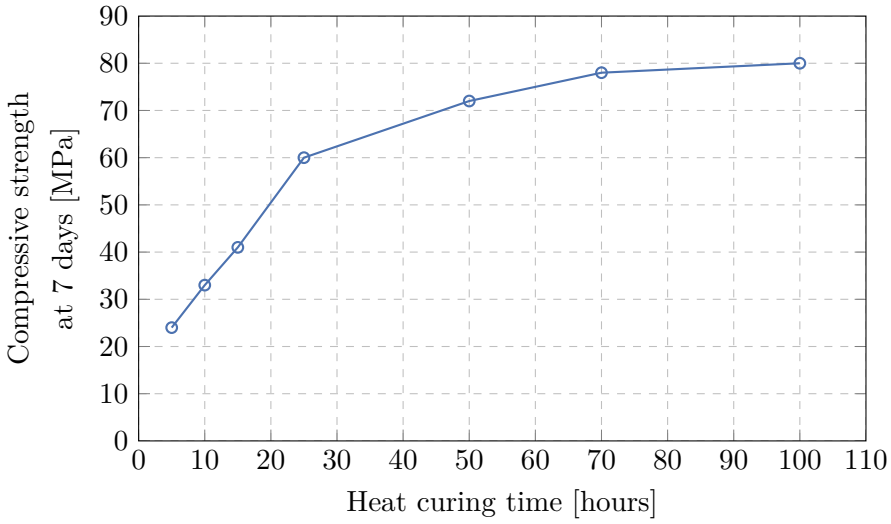

Figure 2.11: Effect of heat curing time on compressive strength (Hardjito et al., 2004)

2.4.2.3 Calcium content

The compressive strength of AAMs are improved with an increase in calcium content. This was demonstrated by both Barnard, (2014) and Nath et al., (2012) who investigated AAMs with a binder material consisting out of fly ash and slag. The slag was the main source of calcium and was varied to determine its effect on the compressive strength. Their results are shown in Figure 2.12. Diaz et al., (2010a) also showed that analytical CaO content within fly ash improves the compressive strength.

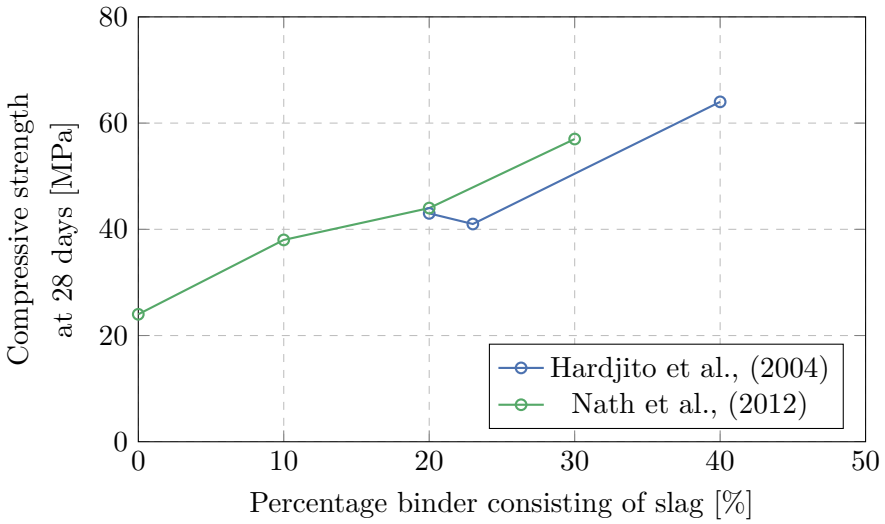

Figure 2.12: Effect of calcium content in binder on compressive strength (Barnard, 2014; Nath et al., 2012)

The improvement in strength with increase in calcium content can be attributed to the calcium silicate hydrates (C-S-H and C-A-S-H) that form in conjunction with the alumina-silicate geopolymer network, as well as the enhancement of the geopolymerisation process (Nath et al., 2012; Diaz et al., 2010b). However, the geopolymerisation process is highly dependent on the crystallinity of the calcium source (Yip et al., 2008). It should also be noted that the setting time of AAMs accelerates drastically when the calcium content is increased, as shown in Figure 2.13 (Diaz et al., 2010a).

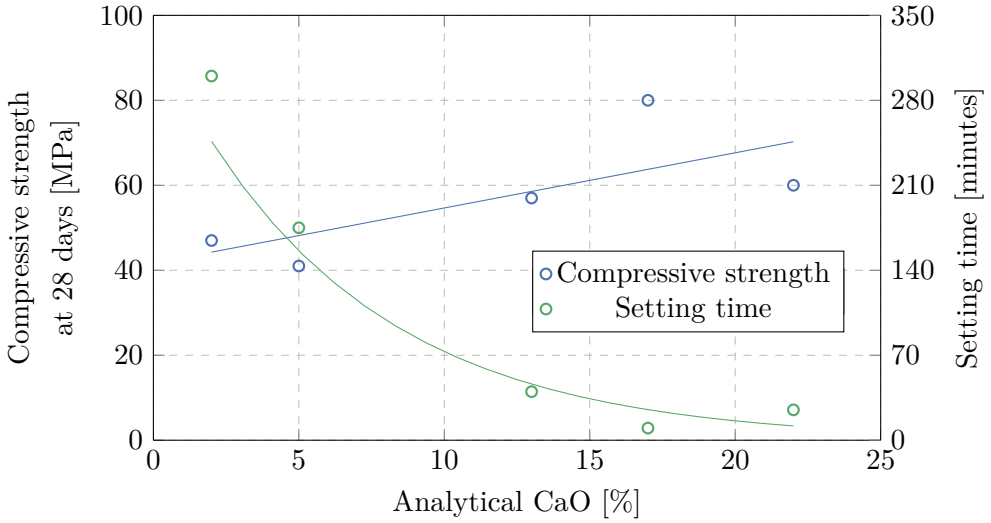

Figure 2.13: Effect of analytical CaO content on the compressive strength and setting times (Diaz et al., 2010a)

2.4.2.4 Type of alkaline activator

As mentioned in Section 2.3.2, there is a variety of alkaline solutions that can be used to activate the binder material of AAMs. The activators which are generally used include: sodium hydroxide (NaOH), potassium hydroxide (KOH), sodium silicate (Na_2SiO_3), potassium silicate (K_2SiO_3), sodium carbonate (Na_2CO_3) and sodium sulfate (Na_2SO_4) (Adam, 2009; Provis et al., 2014). These activators have been tested and compared against one another to obtain the most suitable alkaline activator.

Wang et al., (1994) compared sodium silicate, sodium hydroxide, sodium carbonate and sodium sulfate with one another. It was found that the sodium silicate activator produced the best results, with compressive strengths ranging between 65 MPa and 90 MPa. Adequate compressive strengths were obtained for the sodium hydroxide and sodium silicate, with values of 23 MPa and 36 MPa respectively. The compressive strength for sodium sulfate was quite low (Wang et al., 1994). Similar results were obtained by Bakharev et al., (1999), with compressive strengths of 35 MPa for sodium silicate, 26 MPa for sodium carbonate and 21 MPa for sodium hydroxide.

The effect of combined activators on the compressive strength was tested by Fernández-Jiménez et al., (2003b) and Fernández-Jiménez et al., (2005). The combinations included: sodium silicate and sodium hydroxide; sodium silicate and sodium carbonate; as well as sodium hydroxide and sodium carbonate. The ratios between these activators in combination was also varied. It was found that the specimens with sodium silicate as the primary activator, gave the best results. The results of Fernández-Jiménez et al., (2003b) are summarised in Table 2.3.

Table 2.3: Compressive strengths of different alkali activators (Fernández-Jiménez et al., 2003b)

Specimen	Activator	Compressive strength [MPa]		
		3 days	7 days	28 days
1	Na_2SiO_3	84.75	88.39	88.00
2	80%Na_2SiO_3/20%NaOH	82.61	82.93	83.10
3	80%Na_2SiO_3/20%Na_2CO_3	70.44	81.02	79.57
4	NaOH	37.48	40.26	49.38
5	80%NaOH/20%Na_2SiO_3	43.61	51.81	61.34
6	80%NaOH/20%Na_2CO_3	30.64	39.78	47.87
7	Na_2CO_3	-	14.43	50.20
8	80%Na_2CO_3/20%Na_2SiO_3	-	22.13	51.40
9	80%Na_2CO_3/20%NaOH	-	49.00	55.56

2.4.2.5 Activator concentration

The activator concentration is predominantly associated with the sodium hydroxide, as the sodium hydroxide solids are generally dissolved in water to obtain a specific concentration. However, the concentration should also be considered when sodium carbonate is used.

Several studies have already investigated the effect of the sodium hydroxide concentration on the compressive strength of AAMs. All of these studies obtained higher compressive strengths when the concentration was increased (Hardjito, 2005; Arioz et al., 2012; Álvarez-Ayuso et al., 2008). Figure 2.14 illustrates this increase in strength with higher concentrations. The increase in strength is attributed to the different nature of reaction products that form due to more aluminosilicates dissolving. It was also found that the concentration of the activator is one of the factors that has the most influence on the compressive strength of AAMs (Barnard, 2014; Puertas et al., 2000).

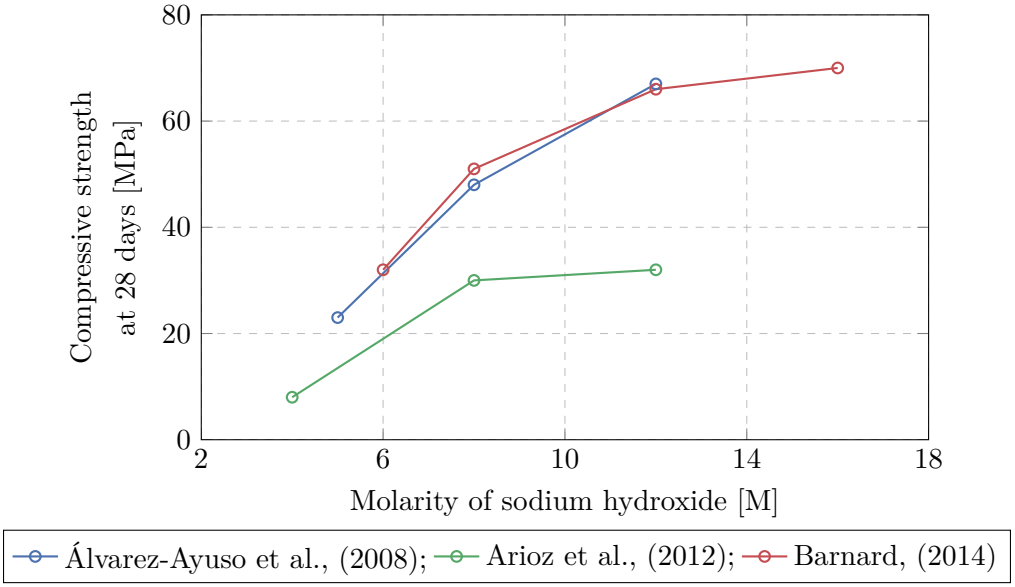

Figure 2.14: Effect of activator concentration on the compressive strength (Álvarez-Ayuso et al., 2008; Arioz et al., 2012; Barnard, 2014)

2.4.2.6 Activator dosage (% Na_2O/binder)

The ratio between the Na_2O content within the alkaline activator and the mass of the binder (% Na_2O/binder), is often used to represent the dosage of the activator. Adam, (2009) tested slag based AAMs with dosages of 3 %Na_2O/binder and 5 %Na_2O/binder, as well as fly ash based AAMs with dosages of 10 %Na_2O/binder and 15 %Na_2O/binder. In both cases the increase in the dosage yielded higher compressive strengths, as shown in Table 2.4. Fernández-Jiménez et al., (2005) obtained similar results, with strengths of 32 MPa, 42 MPa and 70 MPa corresponding to dosages of 6.5 %Na_2O/binder, 8.7 %Na_2O/binder and 13.7 %Na_2O/binder, respectively. More research is still required to determine the effect of dosage on the compressive strength of AAMs.

2.4.2.7 Activator modulus (SiO_2/Na_2O ratio)

Research has shown that the activation of AAMs and their compressive strength are also strongly dependent on the modulus (SiO_2/Na_2O ratio) of the alkali activator. It was generally found

that the strength increased up until an optimum value, and then decreased.

Wang et al., (1994) investigated the effect of the modulus on the compressive strength of different slags. Strengths between 20 MPa and 100 MPa were obtained with the optimum modulus values ranging between 1 and 1.25, as shown in Figure 2.15. Optimum modulus values of 1.25 and 1 were also obtained by Bakharev et al., (1999) and Adam, (2009), respectively. The results from Adam, (2009) is represented in Table 2.4. Collins et al., (2001) increased the modulus from 1 to 1.8, obtaining a decrease in strength. It should be noted that there is a relation between the activator modulus and the dosage in regards with the strength of AAMs (Wang et al., 1994).

Table 2.4: Compressive strengths at different dosages and modulus values (Adam, 2009)

Mix	Na_2O/binder dosage	Activator modulus	Compressive strength (28 day) [MPa]
AAS3-0.75	3%	0.75	15.09
AAS3-1.00	3%	1.00	26.63
AAS3-1.25	3%	1.25	22.93
AAS5-0.75	5%	0.75	43.54
AAS5-1.00	5%	1.00	52.27
AAS5-1.25	5%	1.25	49.48
G10-1.00	10%	1.00	57.04
G10-1.25	10%	1.25	59.71
G10-1.50	10%	1.50	61.03
G15-1.00	15%	1.00	74.69
G15-1.25	15%	1.25	79.26
G15-1.50	15%	1.50	69.16

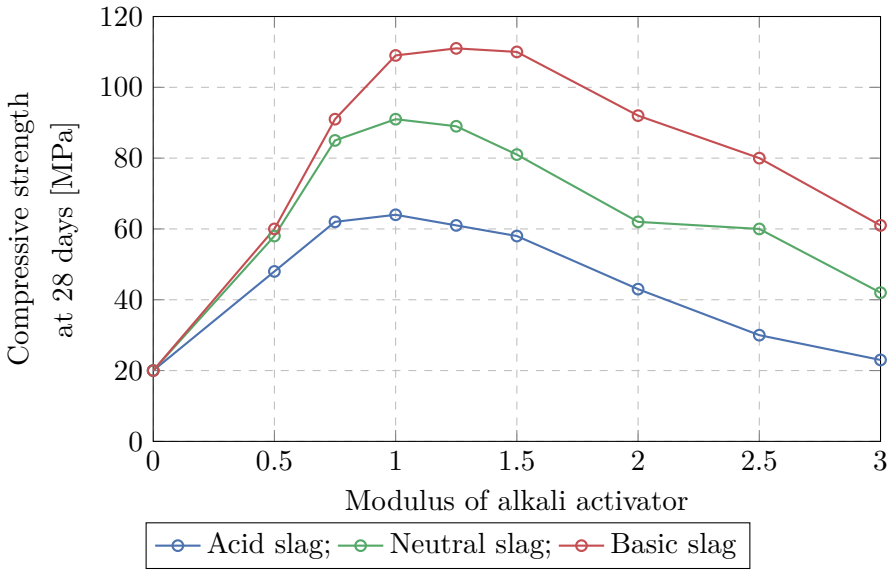

Figure 2.15: Compressive strength at different activator modulus values (Wang et al., 1994)

2.4.2.8 Water Content

The water content of AAMs is generally considered as the water within the alkaline activators, as well as the water added to the mix (Douglas et al., 1992). It should be noted that the water does not take part in the geopolymerisation process, but merely acts as a reagent (Rangan, 2008). However, the mechanical properties of AAMs are affected by the initial amount of water within the mixture.

Both Hardjito et al., (2004) and Lloyd et al., (2010) investigated the effect of the water-to-geopolymer solids ratio on the compressive strength of fly ash based AAMs. The geopolymer solids include the mass of the fly ash, the mass of sodium hydroxide flakes and the mass of sodium silicate solids. A decrease in strength was obtained as the water-to-geopolymer solid ratio increased.

Barnard, (2014) varied the percentage of sodium hydroxide solution replaced by water. Again the compressive strength decreased as more sodium hydroxide was replaced with water. It was also found that, with a high slag content, similar compressive strengths were obtained for 0 % and 10 % of the sodium hydroxide replaced by water. This is due to the calcium silicate hydrate (C-S-H) gel that forms in conjunction with the geopolymeric gel, when slag is also used as a binder (Barnard, 2014). These results are demonstrated in Figure 2.16.

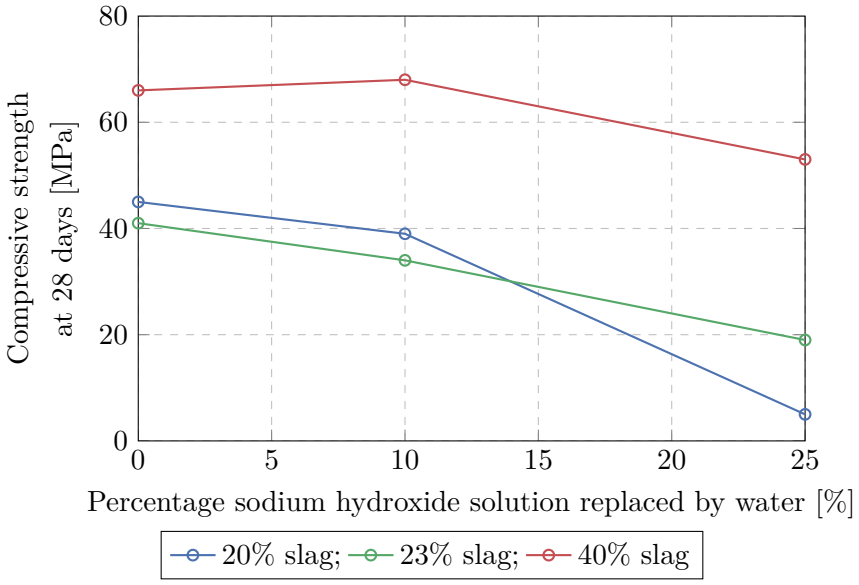

Figure 2.16: Effect of water content on compressive strength (Barnard, 2014)

The workability of fresh AAMs is also influenced by the water content. Lloyd et al., (2010) proposed a guideline, as shown in Table 2.5, which can be used to design fly ash based AAMs for a specific workability and strength.

Table 2.5: Proposed guideline for the design of fly ash based AAMs (Lloyd et al., 2010)

Water-geopolymer solids mass ratio	Workability	Design compressive strength [MPa]
0.16	Very stiff	60
0.18	Stiff	50
2	Moderate	40
0.22	High	35
0.24	High	30

2.5 Applications of AAMs

AAMs have several promising properties such as quick setting, acid resistance, high early age strength, fire resistance, and low cost; making it an ideal material for a wide range of applications (Lawson, 2009). A variety of applications has already been found, particularly since the 1970's, in the following fields: agriculture; industrial; residential; transportation; mining; and hydraulic. These different applications are summarised in Table 2.6 (Roy, 1999).

Table 2.6: Applications of AAMs (Roy, 1999)

	Construction	Nonconstruction
Roads	Heavy-duty pavements cast in situ and pre-cast; reinforced	Waste immobilization
Agriculture	Cast in situ and pre-cast concrete; storage	
Industrial	Acid-resistance buildings; garages; floors slabs; foundations	Bodies of machine tools
Residential	Pre-cast and in situ concrete buildings; slabs; foundations	Dies; moulds
Mining	Oil well grouts; ties; sealing; prevent water penetration	
Hydraulic	Irrigation systems; break waters	Linings

AAMs are predominantly used in the precast industry to produce sewer pipes, railway sleepers, cemetery crypts, box culverts and wall panels (Gourley, 2014). This is mainly due to the early age strength gain of AAMs and the fact that precast factories already use heat curing processes, resulting in an increase in the production rate of elements (Lloyd et al., 2010).

AAMs are also suitable to use in aggressive environments, due to the excellent resistance against chemical attack. It was found that AAM sewer pipes outperformed OPC concrete pipes in aggressive sewer conditions. Therefore, the durability of sewer networks could be improved, which reduces the need for maintenance (Lloyd et al., 2010).

2.6 Health and safety concerns of AAMs

As mentioned before, AAMs consists out of constituents such as slag, fly ash, sodium silicate sodium hydroxide and sodium carbonate. Some of these constituents are dangerous to work with and therefore safety precautions are required. According to safety rules, the constituents for AAMs can be classified into two categories: corrosive products and irritant products as shown in Table 2.7. The corrosive products are aggressive and needs to be handled with gloves, glasses and masks, while the irritant products are friendlier to work with (Davidovits, 2013).

Table 2.7: Safety classification for AAM constituents (Davidovits, 2013)

Corrosive products	Irritant products
CaO (quick lime), NaOH, KOH	$Ca(OH)_2$, Portland cement, Iron slag
Sodium metasilicate SiO_2:$Na_2O = 1$	Slurry soluble silicate/kaolin $1.25 < SiO_2$:$Na_2O < 1.45$
Any soluble silicate SiO_2:$Na_2O < 1.45$	Any soluble silicate SiO_2:$Na_2O > 1.45$

Sodium hydroxide is highly corrosive, especially when mixed with water. This is due to it being an intensely alkaline hydrophilic substance. The concentration of the sodium hydroxide is of utmost importance when determining the level of danger and necessary safety precautions. The effects of the solutions of sodium hydroxide can vary from irritating to non-irritating effects and immediate local effects at point of contact, such as skin and/or eye burns, to fatality when exposed to a large part of the skin or consumed orally. Thus, due to the corrosive effects, the use of sodium hydroxide solution concentrations > 2 % should be prevented. However, if sodium hydroxide is used in low concentrations, it is no longer hazardous. A safe concentration of sodium hydroxide is < 0.5 % in water. At these concentrations, the solutions will no longer be irritating or corrosive, and it will be safe to use (Evonik Industries, 2010).

The construction industry generally require labour intense processes. It is vital that the labourers are not put at risk and work with materials that do not raise health concerns. Therefore, the high sodium hydroxide concentrations (typically higher that > 2 %) which are used for AAMs will be problematic for the labour force on a construction site. The molar ratio for sodium silicate in AAMs is generally higher than 1.45, which are user-friendly conditions and safe for the labourers to use, without raising any health concerns (Davidovits, 2013).

2.7 Concluding summary

There is growing demand for alternative construction materials, such as AAMs, which are more environmental friendly than OPC concrete. This chapter provides background to the development, reaction mechanisms and constituents of AAMs. The mechanical properties and some applications of AAMs are also reported in this chapter.

Although AAMs have promising mechanical properties with several applications for this material, the design of the material is still not understood to the extent that OPC concrete is understood. Especially the mechanical properties and their influencing factors. Therefore, it is important that more knowledge is gained in order to obtain a broader understanding of AAMs.

In this study, the various parameters and their effect on the mechanical properties were investigated. The aim of this investigation was to obtain information that can be used to establish mix design methods for AAMs, as is commonly available for OPC concrete.

Chapter 3

Structural behaviour of reinforced concrete

3.1 Historical development

The earliest form of concrete dates back to 7000 BC in Israel, where it was used for floors. From about 2500 BC, concrete was also used as infill for the stone walls built by the Egyptians, while the Greeks used it as mortar during 500 BC. The Romans also used concrete from about 300 BC. For these early uses, burnt lime (quick lime) was used as the cement for the concrete (Benaim, 2008).

It was not until the second century that the Romans discovered stronger concrete was obtained by mixing pozzolanic materials with the lime. This revolutionised construction, enabling them to design and build concrete domes with large spans, such as the Pantheon in Rome and the Hagia Sophia in Istanbul. After resisting detrimental weather conditions and seismic activity, these domes are still in good condition. This is due to good design and the Roman's knowledge on the use of concrete. However, this knowledge on concrete was lost after the collapse of the Roman Empire (Benaim, 2008; Robberts et al., 2010).

In 1756, John Smeaton attempted to improve the strength and setting of concrete in order to build a lighthouse, as the existing cements were weak and had slow setting. Joseph Aspdin continued with experiments to create stronger concrete and took out the first patent for Portland cement in 1824. This was the start of modern concrete.

In order to overcome the weak tensile strength of concrete, reinforcement is typically used. Although the Romans attempted to use bronze bars as reinforcement, the difference in thermal expansion coefficients between the two material caused it to be unsuccessful. The discovery of iron or steel bars as reinforcement only occurred in the nineteenth century. Reinforced concrete was patented by William Wilkinson in 1854. Today, concrete is more versatile due to the inclusion of reinforcement (Benaim, 2008; Robberts et al., 2010).

3.2 Material properties of reinforced concrete

3.2.1 Concrete

One of the most important properties of concrete is the compressive strength. The 28 day characteristic compressive strength is used to specify concrete into strength classes, as shown in Table 3.1. Generally, cubes of either 100 mm or 150 mm is used to determine the compressive strength of concrete. Cylinders are also used, but due to the shape (height to cross-sectional ratio) the strength is lower than the cube strengths. According to the EN 1992-1-1, (2004), the cylinder strength is taken as 80 % of the cube strength. Both the cube strengths (f_{cu}) and cylinder strengths (f_{ck}) for the different strength classes are given in Table 3.1.

Table 3.1: Strength and deformation properties of concrete (EN 1992-1-1, 2004)

	Strength classes for concrete at 28 days				
f_{cu} [MPa]	20	25	30	45	60
f_{ck} [MPa]	16	20	25	35	50
E_c [GPa]	29	30	31	34	37
ε_c [‰]	1.9	2.0	2.1	2.25	2.45
ε_{cu} [‰]			3.5		

When considering the idealised stress-strain curve for concrete (Figure 3.1), the strain increases with a growing rate as the stress increases. At a certain strain (ε_c), a peak stress (ultimate compressive strength) is reached before the stress reduces. The reduction in stress continuous up until the ultimate strain (ε_{cu}) of 0.0035 (Reynolds et al., 2008). The strain at the ultimate compressive strength for the different concrete classes are also given in Table 3.1.

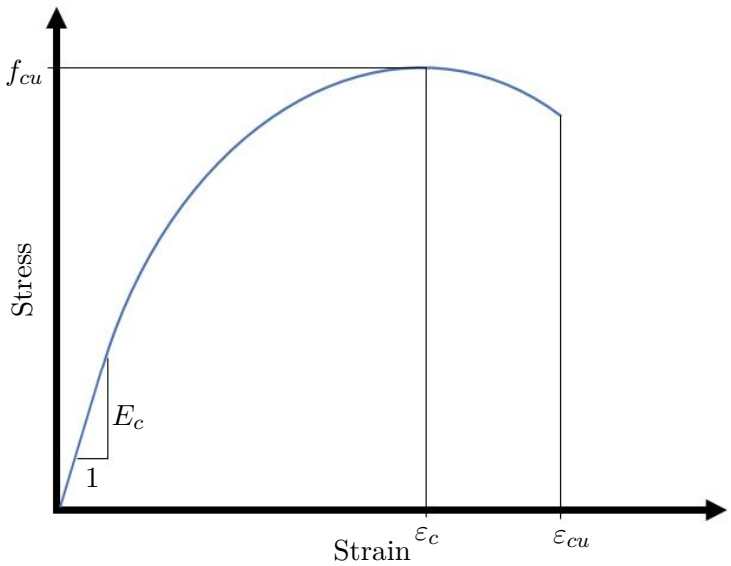

Figure 3.1: Typical stress-strain curve for concrete

The initial response is almost linear, while the concrete behaves plastic at higher stress levels. Even though the initial deformation is not truly linear, it is assumed to be linear-elastic (strain recovers upon unloading) up to approximately a third of the ultimate compressive strength (40 % of cylinder strength). The slope of this linear region is taken as the elastic modulus (E_c), which is also given in Table 3.1 for the different strength classes (Reynolds et al., 2008; Robberts et al., 2010).

3.2.2 Steel

A typical stress-strain response for steel reinforcement is demonstrated in Figure 3.2. Initially, the curve is linear, indicating the elastic behaviour of steel. The slope of this linear region is taken as the elastic modulus (E_s) for steel, with values ranging between 190 GPa and 210 GPa (typically taken as 200 GPa). The steel will start to deform permanently after the yield stress (f_y) is reached. The yield stress for reinforcement steel ranges between 400 MPa and 600 MPa. The strain will continue to increase without any increase in the stress. This region of the curve is referred to as yielding. After yielding, the stress increases again with strain up until a maximum stress, referred to as the ultimate stress (f_u). When this occurs, the steel undergoes strain hardening. The cross-section of a steel specimen decreases as it elongates. This occurs fairly uniform over the length up until the ultimate stress. However, the cross-section of a localised region will start to decrease just after the ultimate stress is reached. This is referred to as necking of the steel. When necking occurs, the stress decreases until the steel breaks (EN 1992-1-1, 2004; Hibbeler, 2014; Robberts et al., 2010).

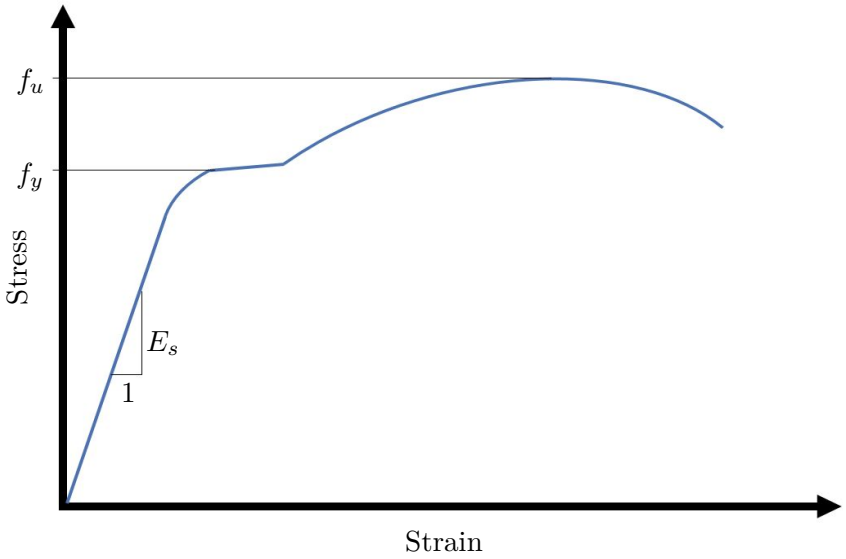

Figure 3.2: Typical stress-strain curve for steel reinforcement

The steel bars used for reinforcement are deformed in order to improve the bond between the steel and the concrete. Ribs are rolled onto the bars to obtain the deformed reinforcement (Benaim, 2008).

3.3 Reinforced concrete in bending

Reinforced concrete is typically used for structural elements such as beams, slabs and columns. Beams and slabs are primarily subjected to bending (flexure), while columns are subjected to bending and axial compression (Wight et al., 2012). For the purpose of this study, the bending behaviour of beams is discussed in terms of design and analysis specified by design codes.

When a load is applied onto a beam, the beam is subjected to an internal moment. The moment can either cause the top of the beam to be in compression, while the bottom is in tension (positive moment) or the top to be in tension, while bottom is compression (negative moment). The reinforcement is used within the tension zone, as the concrete is weak in tension. However, reinforcement can also be used within the compression zone for construction purposes and to assist the concrete in compression (Robberts et al., 2010; Wight et al., 2012).

Consider the doubly reinforced rectangular beam section subjected to positive bending, as shown in Figure 3.3. The internal moment is calculated by taking the moment of the internal forces (F_{cc} and F_{sc}) about the tension reinforcement (A_s):

$$M = F_{cc}z + F_{sc}(d - d') \tag{3.1}$$

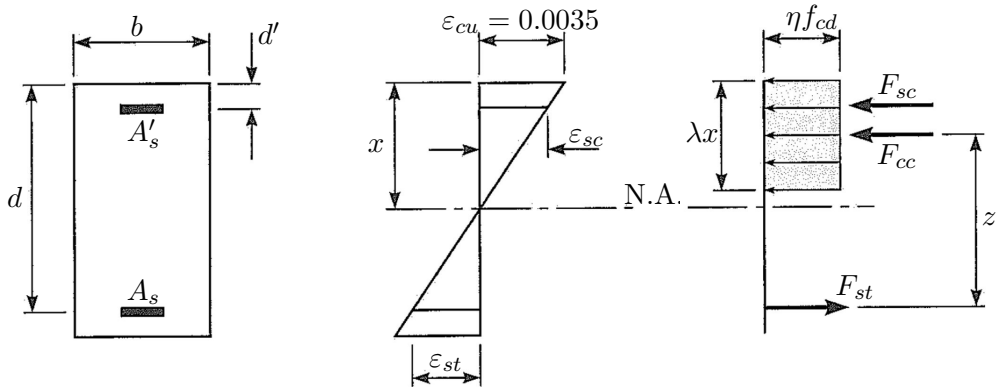

(a) Cross-section (b) Strain (c) Forces within section

Figure 3.3: Beam section for flexure design

The internal forces within the section (F_{cc}, F_{st} and F_{sc}) are taken as the stresses in the concrete and reinforcement, at ultimate, multiplied by the respective concrete and reinforcement areas. This is demonstrated as follows:

$$F_{cc} = \eta f_{cd} b(\lambda x) \tag{3.2}$$

$$F_{st} = f_{yd} A_s \tag{3.3}$$

$$F_{sc} = f_{ycd} A'_s \tag{3.4}$$

A rectangular stress block, as shown in Figure 3.3c, is assumed for the concrete. λ is used to define the effective height for the compression zone, while η is used to define the effective strength. According to the EN 1992-1-1, (2004), λ is taken as 0.8 and η as 1 for concrete strengths lower than 50 MPa. Partial factors are used to obtain the design strengths for the concrete and the reinforcement (f_{cd},f_{yd} and f_{ycd}):

$$f_{cd} = \alpha_{cc} f_{ck} / \gamma_c \tag{3.5}$$

$$f_{yd} = f_y / \gamma_s \tag{3.6}$$

$$f_{ycd} = f_{yc} / \gamma_s \tag{3.7}$$

The long term effects for the compressive strength of concrete, as well as the unfavourable effects from the applied loading are taken into account with α_{cc}. The EN 1992-1-1, (2004) recommends a value of 1 for α_{cc}. γ_c and γ_s are partial safety factors for concrete and steel reinforcement, with values of 1.5 and 1.15 respectively (EN 1992-1-1, 2004).

For the analysis of beams, horizontal equilibrium of the internal forces are taken in order to determine the neutral axis (x), resulting in:

$$x = \frac{F_{st} - F_{sc}}{\lambda \eta f_{cd} b} \tag{3.8}$$

It should be noted that the neutral axis is generally limited ($x < 0.6414d$) during the design. This is done to ensure that the tensile reinforcement yields before the concrete crushes. The compression reinforcement only yields when $d'/x \leq 0.5325$ (Robberts et al., 2010). Therefore, the strain relationship between the concrete and the reinforcement, as indicated in Figure 3.3b, is used to determine the actual internal force within the non-yielding compression reinforcement. This is done by means of the following:

$$F_{sc} = E_s \varepsilon_{sc} \tag{3.9}$$

with

$$\varepsilon_{sc} = (\frac{x - d'}{x}) \varepsilon_{cu} \tag{3.10}$$

3.4 Ductility of reinforced concrete

During the design of reinforced concrete beams, a large amount of attention is given to the flexural strength. However, another important factor to consider is the ductility of a beam (Kwan et al., 2002).

Except for the low bending strength of a plain concrete beam, the beam will also collapse without warning due to the brittle failure mode of the concrete in tension. Therefore, the concrete is reinforced with ductile steel bars. Consequently, the reinforced concrete beam will undergo

larger deflections with a small increase in the sustained load, before failure occurs. This ability of reinforced concrete beams to deform beyond the yield point without a significant loss of strength, is referred to as the ductility. Displacement, rotation, or curvature ratios are generally used to express ductility (Benaim, 2008; Wight et al., 2012).

Kwan et al., (2002) found that the concrete grade, tension steel ratio and compression steel ratio are the major influencing factors for the flexural ductility. However, sufficient flexural ductility is typically included when designing the beam to be under-reinforced. This ensures that the tensile reinforcement yields first before the concrete crushes (Kwan et al., 2002).

3.5 Deflection of reinforced concrete

The members within a structure will deform due to the loading that is applied. Under service load, the function and appearance of a structure should not be impaired by the deformation of the members. In design codes, this is avoided by limiting the deflections to span/250. A span/depth ratio is generally used to control the deflections. However, when the span/depth limit is exceeded, the deflections need to be calculated (Reynolds et al., 2008; EN 1992-1-1, 2004).

The EN 1992-1-1, (2004) provides an adequate prediction of the deformation, considering both uncracked and cracked conditions. A member is considered uncracked when the applied load does not cause the tensile strength of the concrete to be exceeded. The behaviour of a member that is cracked, but not fully cracked, will be in a manner intermediate between the uncracked and cracked conditions. The following expression is used to predict the deformation of structural members subjected to flexure:

$$a = \zeta a_{II} + (1 - \zeta) a_I \tag{3.11}$$

where

- a is the deformation parameter which may be, for example strain, curvature, rotation, or deflection,
- a_I, a_{II} are the values of the deformation calculated for the uncracked and fully cracked conditions respectively,
- ζ is an interpolation coefficient (allowing for the effect of tension stiffening at a section) given by the expression:

$$\zeta = 1 - \beta(\frac{\sigma_{sr}}{\sigma_s})^2 \tag{3.12}$$

where

- β is the coefficient accounting for the influence of the duration of loading or repeated loading on the average strain, taken as 1 for single short-term loading and 0.5 for sustained loads or multiple cycles of repeated loading,

σ_s is the stress in the tension reinforcement calculated on the basis of a cracked section under the load considered,

σ_{sr} is the stress in the tension reinforcement calculated on the basis of a cracked section under the loading conditions that cause first cracking

Note that σ_{sr}/σ_s may be replaced by M_{cr}/M for flexure or N_{cr}/N for pure tension, where M_{cr} is the cracking moment and N_{cr} is the cracking force.

The deflection of members under uncracked and cracked conditions, are typically calculated with formulas that are available in textbooks, such as Robberts et al., (2010) and SAISC, (2013). These formulas consider both the loading conditions and support conditions. The deflections are also largely dependent on the bending rigidity (EI), with the moment of inertia (I) calculated according to the uncracked and cracked conditions. The elastic modulus of the concrete E_c is used, while the member's cross-section is adjusted to consider the elastic modulus of the reinforcement E_s. This is done by multiplying the reinforcement width within the cross-section with a factor equal to E_s/E_c. The moment of inertia (I) is also calculated taking the adjusted cross-section into account (Robberts et al., 2010).

3.6 Cracking of reinforced concrete

As mentioned before, concrete has limited ductility, which causes the concrete to crack when it is exposed to tensile stress. Concrete is subjected to tensile stress during structural actions, such as beams experiencing bending and shear. Internal tensile stresses are also obtained when the reinforcement restrains the concrete from shrinking. The cracks caused by these tensile stresses, are not only unappealing in terms of appearance, they also reduce the durability of the concrete (Benaim, 2008). Therefore, it is essential that the cracking of concrete is considered during the design and construction of structures.

In order to control the amount of cracks and their size, the design codes generally provide limitations for the width and spacing of the cracks, while models are available to calculate the crack widths and spacings. Typically, these models are dependent on the reinforcement properties and dimensions. Therefore, the cracks are also controlled with limitations on the minimum amount of reinforcement that must be used (EN 1992-1-1, 2004).

3.7 Bond between concrete and reinforcement

When reinforced concrete elements are loaded, the stresses within the element has to be transferred between the concrete and the reinforcement in order for the reinforcement to resist the tensile forces. This ability of the concrete and the reinforcement to transfer forces between one another, is referred to as the bond (Wight et al., 2012).

Considering the differential element of a reinforcement bar along the embedded length, as shown in Figure 3.4. In order to maintain equilibrium, bond stresses ($\sigma_b(x)$) must exist on the surface of the reinforcement bar:

$$(\frac{\pi\phi^2}{4})d\sigma_s = (\pi\phi\sigma_b)dx$$

which can be simplified to

$$d\sigma_s = (\frac{4}{\phi}\sigma_b)dx \tag{3.13}$$

where

σ_s is the axial (tensile) stress in the reinforcement bar, in MPa,

ϕ is the nominal diameter of the reinforcement bar, in mm,

σ_b is the bond stress, in MPa, and

dx is length of the differential element

From Equation 3.13, it is evident that bond stresses are required between the concrete and the reinforcement when there is a change in tensile force (T) along the length of the rebar. Without the bond stresses, the tensile force will be zero and the rebar will pull out of the concrete. This will result in the concrete resisting the tensile stresses, causing the structural element to fail. Therefore, the development of tensile stresses are not possible without the bond between the concrete and the reinforcement.

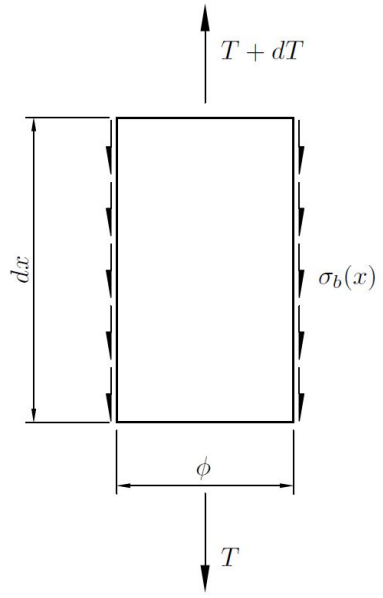

Figure 3.4: A differential element of length dx representing the tensile forces and bond stresses. Adjusted from Wight et al., (2012)

According to the Model Code, (2010), the relationship between the bond stresses and the slip of the reinforcement can be represented in terms of an analytical model. This is possible under

well-defined conditions and when short anchorage lengths are used. The analytical model is presented in Figure 3.5, where the bond between the concrete and the reinforcement is given in terms of the relative displacement of the reinforcement bar, parallel to the axial tensile force. The variables that are used include the bond stress (σ_b), the peak bond stress (σ_{bmax}), the residual bond stress (σ_f), slip of the reinforcement bar (S) and the characteristic slip values (S_1,S_2 and S_3). The bond stresses are given in MPa, while the slip is given in mm.

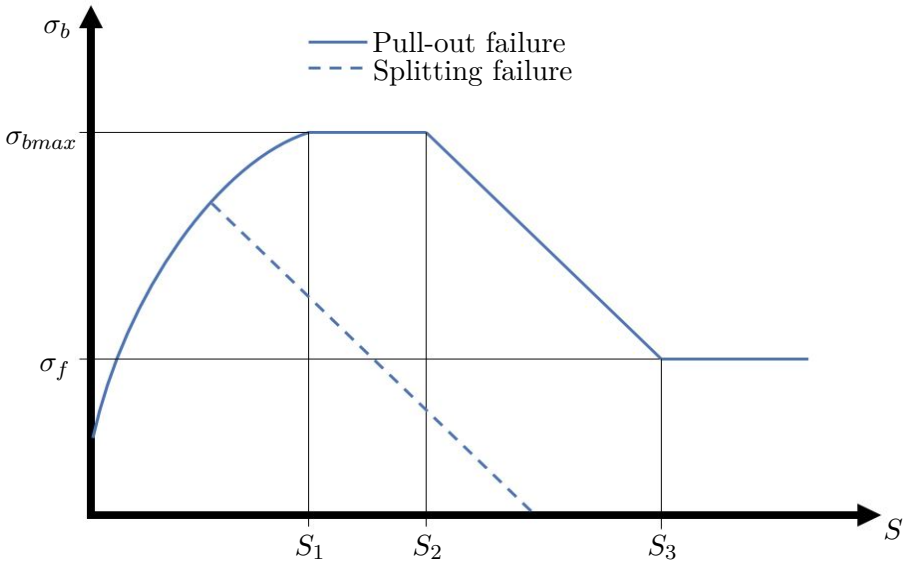

Figure 3.5: Analytical model of the bond-slip relation (Model Code, 2010)

A piecewise equation is used to predict the bond-slip envelope as given in Figure 3.5:

$$\sigma_b = \begin{cases} \sigma_{bmax}(\frac{S}{S_1})^{\alpha} & \text{for } 0 \leq S \leq S_1 \\ \sigma_{bmax} & \text{for } S_1 \leq S \leq S_2 \\ \sigma_{bmax} - (\sigma_{bmax} - \sigma_f)\frac{S-S_2}{S_3-S_2} & \text{for } S_2 \leq S \leq S_3 \\ \sigma_f & \text{for } S_3 \leq S \end{cases} \tag{3.14}$$

The values for the variables are given in Table 3.2. These values are influenced by the failure mode, as well as the bond conditions within each failure mode. The bond conditions are associated with the casting position (Model Code, 2010).

Table 3.2: Model parameters

	Pull-out failure $\varepsilon_s < \varepsilon_{s,y}$		Splitting failure $\varepsilon_s < \varepsilon_{s,y}$			
	Good bond cond.	other bond cond.	Good bond cond.		other bond cond.	
			Unconfined	Confined	Unconfined	Confined
σ_{bmax}	$2.5\sqrt{f_{cu}}$	$1.25\sqrt{f_{cu}}$	$7(f_{cu}/25)^{0.25}$	$8(f_{cu}/25)^{0.25}$	$5(f_{cu}/25)^{0.25}$	$5.5(f_{cu}/25)^{0.25}$
S_1	1.0	1.8	$S(\sigma_{bmax})$	$S(\sigma_{bmax})$	$S(\sigma_{bmax})$	$S(\sigma_{bmax})$
S_2	2.0	3.6	S_1	S_1	S_1	S_1
S_3	c_{clear}	c_{clear}	$1.2S_1$	$0.5c_{clear}$	$1.2S_1$	$0.5c_{clear}$
α	0.4	0.4	0.4	0.4	0.4	0.4
σ_f	$0.4\sigma_{bmax}$	$0.4\sigma_{bmax}$	0	$0.4\sigma_{bmax}$	0	$0.4\sigma_{bmax}$

with c_{clear} the clear distance between ribs of steel reinforcement
with ε_s and $\varepsilon_{s,y}$ being the reinforcement strain and yield strain respectively
with α the regression constant used for empirical data fit
with σ_f the residual bond capacity as a result of confinement steel

As demonstrated by the model, the bond-slip behaviour for embedded reinforcement can be divided into different stages. This is due to the mechanisms controlling the force transfer between the concrete and the reinforcement. The chemical adhesion between the concrete and the reinforcement is the first controlling mechanism. The slip of the reinforcement bar only initiates after adhesion breaks down. The Model Code, (2010) considers the adhesion bond as insignificant and therefore taken as zero. From the slip that was initiated, shear stresses develop causing frictional bond, while mechanical interlock occurs due to the concrete that crushes between the ribs of the reinforcement. These mechanisms increase the bond stress until failure occurs from the bar pulling free from the concrete (pull-out failure) or the concrete cracks and splits at the surface (splitting failure). This results in a decrease in the bond stress. For the pull-out failure, the residual bond (σ_f) is due to the confinement of the reinforcement (Penelis et al., 2014).

At the peak stress, a large amount of slip has already taken place. Therefore, this peak stress cannot be used during the design of structures, as slip should be avoided. According to the EN 1992-1-1, (2004), a design bond stress (σ_d) can be calculated, which is dependent on the tensile strength of concrete:

$$\sigma_d = 2.25\eta_1\eta_2 f_{ctd} \tag{3.15}$$

where

η_1 is the bond condition factor, taken as 1 for good bond conditions and 0.7 otherwise,

η_1 is the bar size factor, taken as 1 for $\phi \leq 32$ mm and $(\frac{132-\phi}{100})$ for $\phi \geq 32$ mm, and

f_{ctd} is the design tensile strength of concrete, in MPa, obtained from:

$$f_{ctd} = \alpha_{ct}(\frac{f_{ctk,0.05}}{\gamma_c}) \tag{3.16}$$

where

$f_{ctk,0.05}$ is the 5 % fractile value of the characteristic tensile strength for concrete,

α_{ct} is the coefficient taking account for the long term effects on concrete tensile strength ($\alpha_{ct} = 1$ recommended), and

γ_c is the partial safety factor for concrete

The values can be obtained from EN 1992-1-1, (2004).

Penelis et al., (2014) stated that the mean bond shear stress at which 0.1 mm slip occurs, can be used as the conventional σ_d value. Therefore, when a bond test is performed, the design bond stress (σ_d) is obtained by dividing the force in the reinforcement with the bond contact area, at a 0.1 mm free-end displacement (slip) of the reinforcement bar.

3.8 Concluding summary

There are a number of factors that needs to be considered when designing reinforced concrete structures. These factors include, but are not limited to: the mechanical properties of the materials; the flexural behaviour; ductility; cracks; and the bond between the concrete and the reinforcement. The behaviour of structural elements in terms of these factors are predicted, calculated and controlled with the use of design codes, such as EN 1992-1-1, (2004). These design codes also have to apply to AAMs, in order for AAMs to be used as a structural material. However, it must first be determined if similar structural behaviour is obtained between AAMs and OPC concrete. In this study, the structural behaviour of AAMs was tested and compared against OPC concrete. This was done with reinforced beam tests and pull-out tests.

Chapter 4

Experimental Design

A variety of studies have been done on alternative construction materials, such as AAMs, in order to reduce the negative environmental impact associated with OPC concrete. In this study, a fly ash/slag based AAM was investigated; aiming to determine the structural use of AAMs.

In order to reach this goal, four objectives were formulated. These objectives include: finding an alternative activator to hazardous sodium hydroxide (sodium hydroxide and sodium silicate are the main activators used); establishing relationships between constituents and the compressive strength for mix design of AAMs; improving the low modulus of elasticity of AAMs; and determining the behaviour of reinforced AAMs.

This study can be divided into two parts, namely: the mechanical properties of AAMs and the structural behaviour of reinforced AAMs. The mechanical properties, such as the compressive strength and the elastic modulus, were determined for the first three objectives, while reinforced beam tests and reinforcement pull-out tests were performed for the structural properties in the last objective.

The experimental preparation, test setups and methods, material specifications, and mix designs are given in this chapter.

4.1 Experimental preparation

Unless otherwise stated, the following preparation procedures were conducted to produce the specimens for each of the mixes. These procedures were based on that of Barnard, (2014).

4.1.1 Activator preparation

The sodium hydroxide was obtained in the form of flakes, while the sodium carbonate was in powder form. Thus, preparation was required for these activators in order to obtain solutions with specific concentrations. The method that was used for the concentration calculations is discussed in Section 4.3.3

The required mass of sodium hydroxide flakes (which is depended on the concentration) was first weighed, before normal tap water was added to obtain the specific mass of sodium hydroxide solution for a mix. The solution was stirred until all the flakes dissolved. As mentioned in Section 2.3.2.2, the solution of sodium hydroxide in water is an exothermic reaction. Therefore, the solution was left to cool down for approximately an hour before mixing. However, the sodium hydroxide solutions that was used to make the large mixes required for the beam- and pull-out specimens, reached temperatures up to 75 °C and took longer to cool down. These solutions were placed in a room with ambient temperature of 5 °C until they cooled to a temperature of approximately 25 °C.

The same preparation procedure was followed to produce the sodium carbonate solutions. However, the solution of sodium carbonate in water is not an exothermic reaction. Therefore, the solution was only left until all the solids dissolved.

In previous studies, the sodium hydroxide and sodium silicate was mixed together a day prior to mixing (Adam, 2009; Hardjito et al., 2005). This caused rapid setting. A possible explanation for this is the silica from the sodium silica solution that already starts to dissolve, which in turn accelerates the geopolymerisation process (Barnard, 2014; Davidovits, 2011). Therefore, the sodium hydroxide and sodium silicate was added separately to the mix.

4.1.2 Mixing procedures

The mixing procedures for both the AAM mixes and OPC mixes were kept the same as far as possible. This was done to obtain comparable results between the AAM mixes and OPC mixes.

In order to ensure that the mixes had a constant temperature during mixing, the dry constituents (aggregate and binder material) for the mixes were weighed and placed in a climate controlled room approximately 12 hours before mixing took place. A regulated temperature of 24 °C and a relative humidity of 65 % was maintained within the climate controlled room.

The mixing took place in rotary pan mixers with capacities of either 25 l, 50 l or 120 l, depending on the size of the mix required. The majority of the mixes had a volume of 10 l, which was mixed in the 25 l mixer. The 50 l mixer was used for the pull-out mixes with a volume of 25 l, while the beam mixes with a volume of 115 l were mixed in the 120 l mixer. Before mixing took place, the mixers were cleaned and dried.

The dry constituents were added first to the mixer in the following order: fine aggregate; binder material (fly ash and slag for AAM mixes and cement and limestone for OPC mixes); and coarse aggregate. These dry constituents were mixed for a minute before the liquids were added. The liquids for the AAM mixes consisted out of alkaline solutions and additional water, while the liquid for OPC mixes only consisted of water. The different alkaline solutions were added separately to the mixer as mentioned in Section 4.1.1. Mixing of all constituents continued for another three minutes. The mixing sequence and time was consistent for all the mixes.

The AAM mixes had self-compacting characteristics, which made it flow with ease. Therefore,

compaction was not required for these mixes after it was cast within the different moulds. However, the OPC mixes were compacted. All the OPC mixes, except the beam mixes, were compacted for approximately 30 seconds on a vibrating table. The OPC beam mixes were compacted with a poker vibrator.

4.1.3 Curing procedures

AAMs are cured differently to OPC concrete as water curing is not required. According to Barnard, (2014), a loss in strength is experienced when AAMs are cured in water. This is due to the activator being leached from the AAM (Andrew Heath, 19 April 2016, personal communication). The following curing procedures were used for the AAM mixes and the OPC mixes.

4.1.3.1 AAM curing

The binder material within AAMs determine the curing procedure. Low calcium based binder materials usually require heat curing in order to develop strength. In this study, the binder material consisted out of slag (calcium source) and fly ash. Thus, ambient curing was possible.

After casting, specimens were left to harden in the laboratory for approximately 24 hours before they were demoulded. The specimens were placed in the climate controlled room after demoulding. As mention before, the climate controlled room had a constant temperature of 24 °C and a relative humidity of 65 %. The specimens were left in the climate controlled room for the remainder of the time right up until they were tested

4.1.3.2 OPC curing

The OPC specimens were also demoulded approximately 24 hours after casting. The smaller specimens were placed in a curing bath with a temperature of 25 °C, while the beam specimens were placed on the laboratory floor and covered with blankets, as they could not be placed in the curing baths. The blankets were permanently soaked to ensure proper curing.

4.2 Test setup and methods

The first three objectives of this study focused on the mechanical properties of AAMs. Thus, tests were done to obtain the compressive strength, density, elastic modulus and stress-strain relationship for AAMs. The workability of the AAMs was also determined.

The structural behaviour of reinforced AAMs were investigated for the last objective. The reinforced beam test and the pull-out test were done to obtain information on the bending behaviour and bond performance of AAMs with reinforcement.

The tests for both mechanical properties and structural behaviour, are discussed in this section. Unless otherwise stated, the specimens for each of the different tests were tested at 28 days.

4.2.1 Workability

The workability of the AAMs were determined in order to obtain some information with regard to the flowability, consistency and finishability of AAMs. Due to different procedures and applications used during concrete construction, information on these properties could also be an essential part in the design method for AAMs.

As mentioned before, the AAMs exhibited self-compacting characteristics, resulting in flowable mixes. The large amount of fly ash within the mixes and the spherical shape thereof, both contributed to the self-compacting characteristics. However, the OPC mixes that was used did not have any self-compacting characteristics, as only the basic constituents for OPC concrete was used in order to attain similar strengths to that of the AAM mixes.

A slump test as specified by EN 12350-2, (2009) was performed to determine the workability of the OPC mixes. A slump cone was filled in three layers; each layer approximately a third of the volume. A steel rod was used to manually compact each of the layers with 25 strokes. The slump cone was then lifted upward and a measurement was taken of the vertical displacement (distance between the top of the concrete and the hight of the slump cone). The concrete was also inspected for segregation.

A slump flow test was used for the AAM mixes, due to the self compacting characteristics. Therefore, the slump cone was just filled with the AAM mix without any compaction with the steel rod. Again, the slump cone was lifted upward after it was filled. This was done without causing any obstruction to the flow of the AAM mix. The diameter of the AAM mix was measured after it stopped flowing. Two measurements were taken perpendicular to one another and the average was taken as the slump diameter. The consistency was also observed by looking whether the mix segregated and also whether the mix could keep the stone intact while flowing (carry the stone).

Self-compacting characteristics were not attained in some of the AAM mixes where alternative activators were used. For these mixes, the vertical displacement was measured, instead of the slump flow diameter.

4.2.2 Compressive strength

The compressive strength of concrete is one of the main properties that is used when designing a concrete mix. Due to the lack of mix design methods for AAMs, this was a critical mechanical property which was investigated during this study.

The compressive strength of the AAM mixes were obtained for both cube specimens and cylinder specimens. The compressive strength of four cube specimens were tested according to EN 12390-

3, (2002), while the three cylinder specimens were used to obtain the elastic modulus (Section 4.2.4) and the stress-strain curve (Section 4.2.5). The compressive strength for the cylinder specimens was taken from the stress-strain curve, which is discussed in Section 4.2.5.

The 100 x 100 x 100 mm cube specimens were tested in the 200t Contest Compression Testing Machine. A constant loading rate of 180 kN/min was used to load the specimens until failure. The load was applied perpendicular to the casting direction. At failure, the maximum force was recorded, which was used to calculate the compressive strength of each specimen:

$$f_{c,cube} = \frac{F}{A} \tag{4.1}$$

where

$f_{c,cube}$ is the compressive strength, in MPa,

F is the force at failure obtained from the contest, in N, and

A is the surface area over which the force is applied, in mm^2.

The compressive strength of a certain mix was taken as the average compressive strength of four cube specimens.

4.2.3 Density

The four cubes, as mentioned in Section 4.2.2 for the compressive strength test, were used to determine the density of each of the AAM mixes. The densities of the cubes were determined before they were crushed and the average was taken as the density for a specific AAM mix. The following equation was used to determine the density:

$$\rho = \frac{m}{V} \tag{4.2}$$

where

ρ is the density, in kg/m^3,

m is the mass of the AAM cube, in kg, and

V is the volume of the cube, in m^3.

The volume of the cube was determined by measuring the dimensions of the cube with a ruler to the nearest mm.

4.2.4 Elastic modulus

The elastic modulus was also an essential part of this study, as the elastic modulus for AAMs are generally relatively low. Because the elastic modulus is related to the stiffness of the concrete;

low elastic modulus values will result in structural elements with large deflections. Therefore, the elastic modulus was tested for all the mixes, in order to find a way to improve these low values.

As mentioned before, three cylinder specimens with a diameter of 100 mm and a height of 200 mm were tested for each mix. The elastic modulus for these specimens were tested according to EN 12390-13, (2013). The main concept of the test is to apply a compression load on the specimens until a limiting load is reached. This limiting load is lower than the capacity of the specimen. The related strains are recorded to produce a stress-strain plot of which the slope is taken as the elastic modulus for the specimen. Therefore, the strengths that was obtained for the cubes, as described in Section 4.2.2, was used as the capacity for each mix. The compressive strength of the cubes were multiplied by 0.8 (EN 1992-1-1, 2004), due to the slenderness of the cylinder specimens (aspect ratio of 2 versus aspect ratio of 1 for cubes) resulting in a lower yield strength.

Before the specimens were tested, the top of the cast end was ground in order to obtain a smooth and flush surface, as shown in Figure 4.1a. This was done in the Matest grinding machine, as shown in Figure 4.1b. After the preparation of the cylinder specimens, three linear variable displacement transducers (LVDT's) were placed around the test specimen at equidistant intervals of 120 degrees and a reference gauge length of 70 mm (Figure 4.2). The average of the three LVDT's was taken as the deformation.

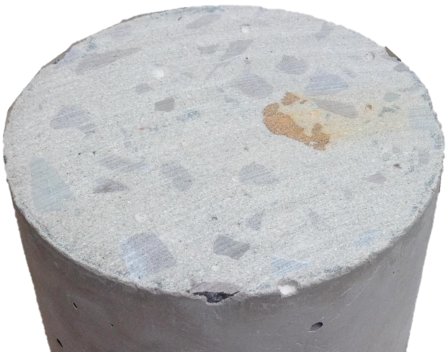

(a) Smooth and flush surface

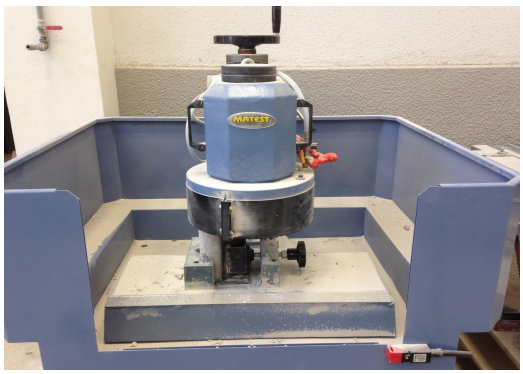

(b) Grinding machine

Figure 4.1: Preparation of cylinder specimens

The 2 MN Instron Testing Machine was used to apply the loading on the specimens. Once a specimen was in place, a preload was first applied for 20 seconds, which was followed by three loading cycles (Figure 4.3). The preload (σ_{p}) was taken as 0.5 MPa, while a third of the maximum cylinder compressive strength was used for the upper limit stress (σ_{u}). These loads were maintained for 20 seconds in each cycle. A constant loading rate of 0.6 MPa/s was used. A graphical representation of these loading cycles are given in Figure 4.3. The elastic modulus was calculated as follow:

$$E_c = \frac{\sigma_{\mathrm{u}} - \sigma_{\mathrm{p}}}{\varepsilon_{\mathrm{u},3} - \varepsilon_{\mathrm{p},2}} \tag{4.3}$$

where

E_c is the elastic modulus, in GPa,

σ_u is the stress on the specimen when the upper load is applied, in MPa,

σ_p is the stress on the specimen when the preload is applied, in MPa,

$\varepsilon_{u,3}$ is the strain recorded at the upper stress level on the third loading cycle, in mm/mm, and

$\varepsilon_{p,2}$ is the strain recorded at the preload level the second loading cycle, in mm/mm.

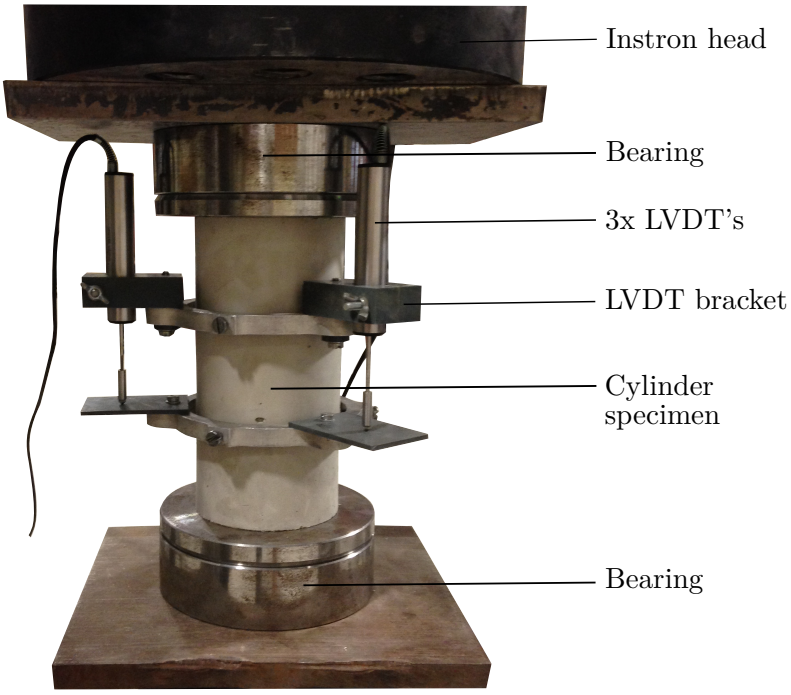

Figure 4.2: Elastic modulus test setup

The recorded force was divided by the specimen's cross sectional area to obtain the stress (σ_u and σ_p), while the strain was calculated by dividing the recorded deformation by the gauge length.

4.2.5 Stress-strain relationship

After the last load cycle for the elastic modulus, the test was continued to obtain the stress-strain curve of each specimen. This was done by applying a displacement controlled load up until the specimen failed. A constant loading rate of 0.02 mm/s was used. The stress-strain loading can be observed in Figure 4.3.

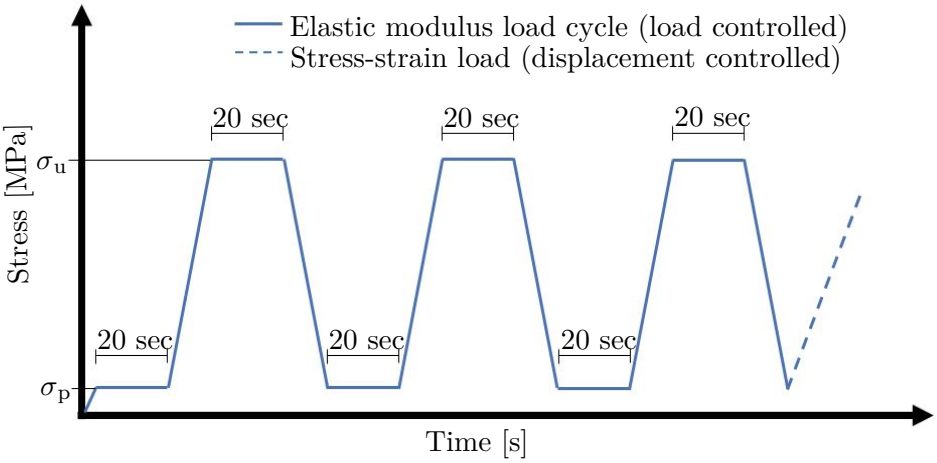

Figure 4.3: Load cycle for elastic modulus and stress-strain

The cylinder strength, stress percentage and the strain percentage were obtained from the stress-strain curve (Figure 4.4). The cylinder strength was taken as the point where failure occurred, therefore, at the ultimate stress ($f_{c,cyl}$). The yield stress (f_{cy}) was divided by the ultimate stress ($f_{c,cyl}$) to obtain the stress percentage, while the strain percentage was calculated by dividing the yield strain (ε_{cy}) with the strain at ultimate stress (ε_c). The yield- stress and strain was taken as the point where the stress strain curve no longer exhibited linear-elastic behaviour. This point was determined with the offset method similar to that described in ASTM E8/E8M-09, (2011). A line was plotted on the stress-strain graph, using the elastic modulus (E_c) as the gradient and intersecting the x-axis (strain) at 0.0001 mm/mm (0.01 %). The yield- stress and strain was assumed to be the point where the offset line and the stress-strain curve intersected.

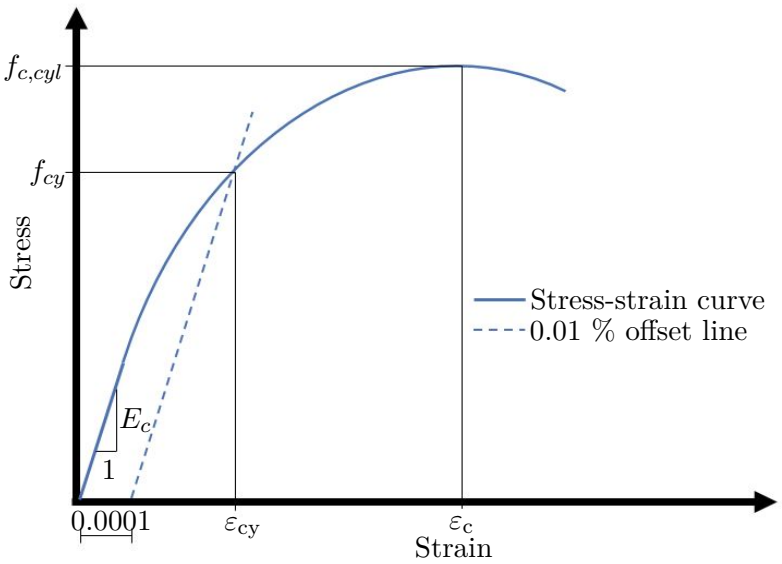

Figure 4.4: Determination of stress and strain percentages

The stress percentage gives an indication of the linear-elastic behaviour of the stress-strain curve. Thus, the stress-strain curve had a large linear-elastic portion with a high stress percentage, while a low percentage resulted in a small linear-elastic portion. The strain percentages demonstrated the deformation and the ductility of the specimens. Low strain percentages showed that the specimens had large deformations resulting in a high ductility if the stress percentage was large, while the deformations were small at high strain percentages indicating low ductility.

4.2.6 Reinforced beam tests

4.2.6.1 Introduction

The reinforced beam (RB) test was done to investigate the bending behaviour of AAMs. This test was performed by simply supporting the reinforced beam at the ends and applying two concentrated loads symmetrically over the span (four point bending). This ensured that the maximum moment occurred between the two loads, with no internal shear force. A similar test was also done by Sumajouw et al., (2006)

Two different AAM mixes were used for the RB test, which were compared against two OPC mixes with similar strength properties. The AAM mixes and OPC mixes are described in Section 4.4.3. Two reinforced beams, with the same reinforcement arrangement, were tested for all four of the mixes.

4.2.6.2 Beam specimens

The beams were designed according to EN 1992-1-1, (2004). The RB specimens were 150 mm wide by 220 mm deep in cross section, with a length of 3000 mm. Two 16 mm high tensile yield stress ribbed bars were used for the tension reinforcement while the compression reinforcement consisted out of one 12 mm bar of the same type. The stirrups was smooth mild steel bars which had a diameter of 6 mm and were placed at spacings of 120 mm along the length of the beam. Plastic spacers were used to provide a cover of 35 mm. The beam dimensions with the reinforcement details is given in Figure 4.5.

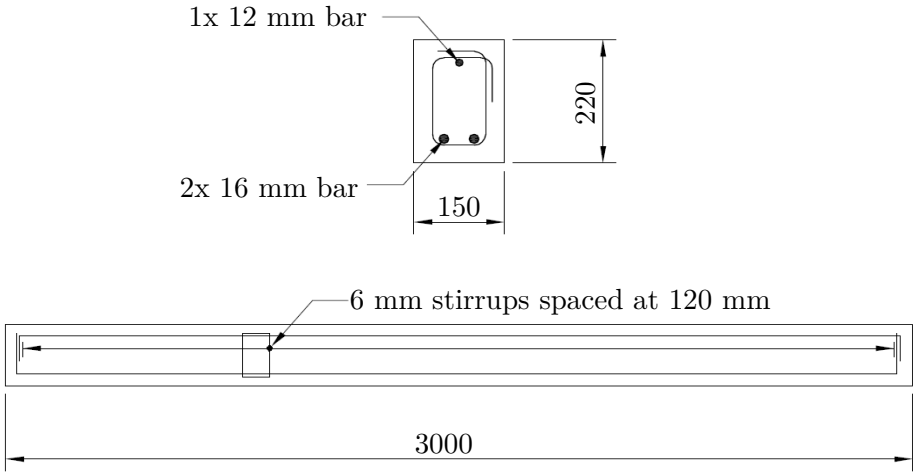

Figure 4.5: RB specimen dimensions with the reinforcement details

Wooden moulds were constructed for the RB specimens from 20 mm thick chipboard. These moulds were also painted to minimise the absorption of water, which ensured that the moulds could be used multiple times. The wooden moulds with the fitted reinforcement is shown in Figure 4.6a.

Hooks were cast into the beams in order to lift the beams with an overhead crane. The crane was used to place the beams in position for testing. 10 mm steel bars were also cast into the beams; directly above the support positions. The bars supported the steel tubes used for measuring the deflection of the beams, which is discussed in the following section. The demoulded RB specimen with the position of the lifting hooks and bars are shown in Figure 4.6b.

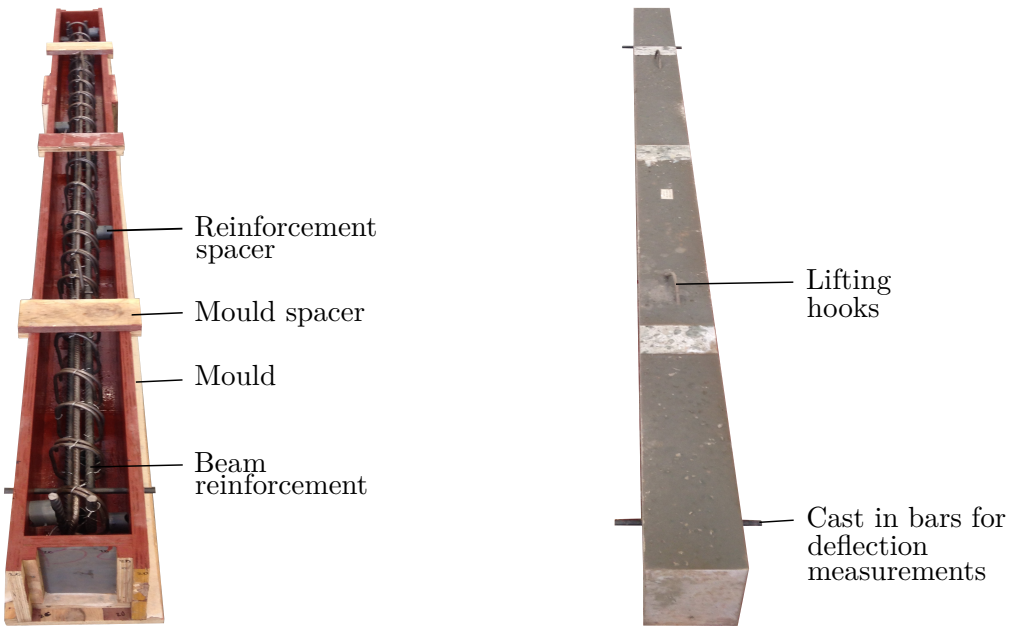

Figure 4.6: (a) RB specimen moulds, and (b) Demoulded RB specimen

4.2.6.3 Testing machine and setup

The RB specimens were simply supported over a span of 2700 mm, while a 500 kN Instron hydraulic actuator was used to apply the load. The actuator was fixed to a separate constructed frame, which is shown by the schematic drawing in Appendix B. A spreader beam was used to distribute the load from the actuator into two concentrated loads. These two loads were placed symmetrically over the span, resulting in a distance of 900 mm between the two loads. The RB test setup is shown in Figure 4.7 (see also Appendix B).

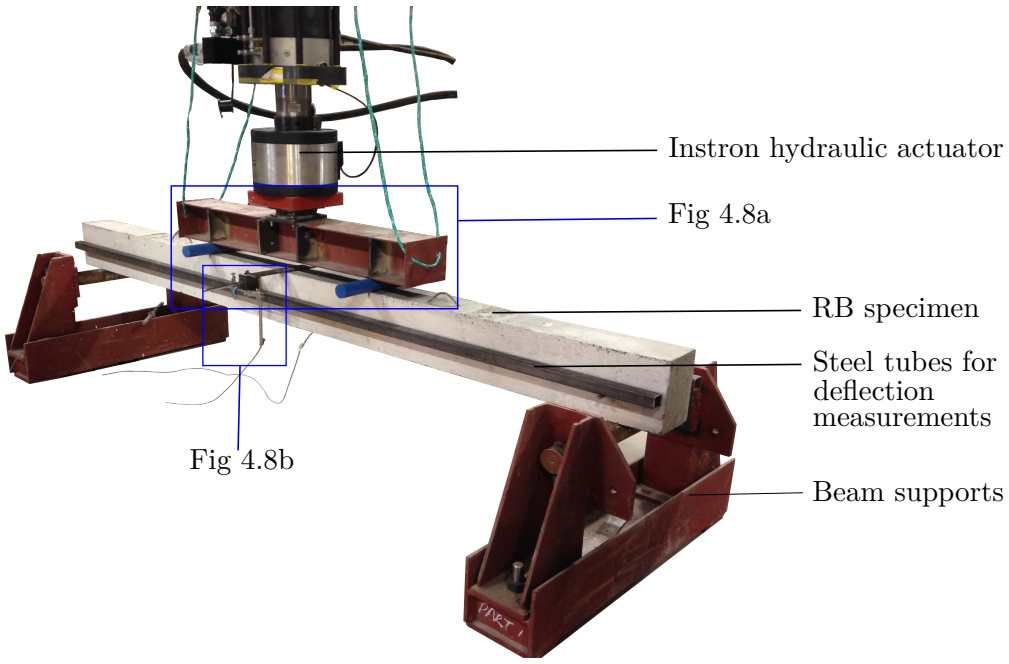

Figure 4.7: RB test setup showing the simply supported RB specimen with two concentrated loads applied

In order to obtain the two concentrated loads, the spreader beam was placed on two rollers, as shown in Figure 4.8a. At the locations of the rollers, the surface of the RB specimens were ground smooth to eliminate stress concentrations. The one side of each RB specimen was also white washed to help with the identification of cracks.

The deflection of the RB specimens were measured at the midspan. This was done with two LVDT's which were positioned on both sides of the RB specimen. A magnetic clamp, which was attached to the steel tube (Figure 4.7), was used to hold the LVDT's in place. The square tubing was simply supported between the bars cast in for defection measurements; also spanning at a distance of 2700 mm. Therefore, the square tubing remained horizontal keeping the LVDT's in position, while the beams deflected. At the midspan, a steel plate was fixed to the top of the RB specimens in order to press down on the LVDT's and determine the deflection of the beams. The LVDT's had a stroke length of 50 mm. Figure 4.8b demonstrates the setup used to measure the deflection of the beams.

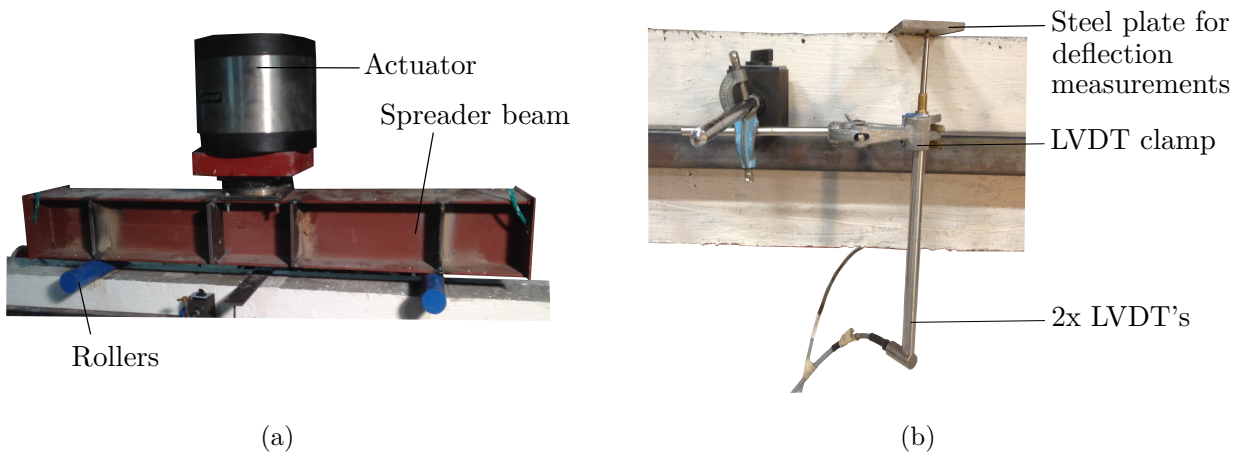

Figure 4.8: (a) Spreader beam used to obtain two concentrated loads, and (b) LVDT setup used to measure the deflection of the RB specimens

4.2.6.4 Loading state

As mentioned, the RB specimens were loaded symmetrically with two concentrated loads between the supports. The distance between the supports and the loads were equal to the distance between the two loads, as shown in Figure 4.9. This resulted in a maximum moment between the loads, while the shear force is zero; assuming that the self-weight of the beams is neglected. By doing this, the maximum moment occurred over a larger distance and was not influenced by the shear force over that distance. The shear force diagram and moment diagram is illustrated in Figure 4.9.

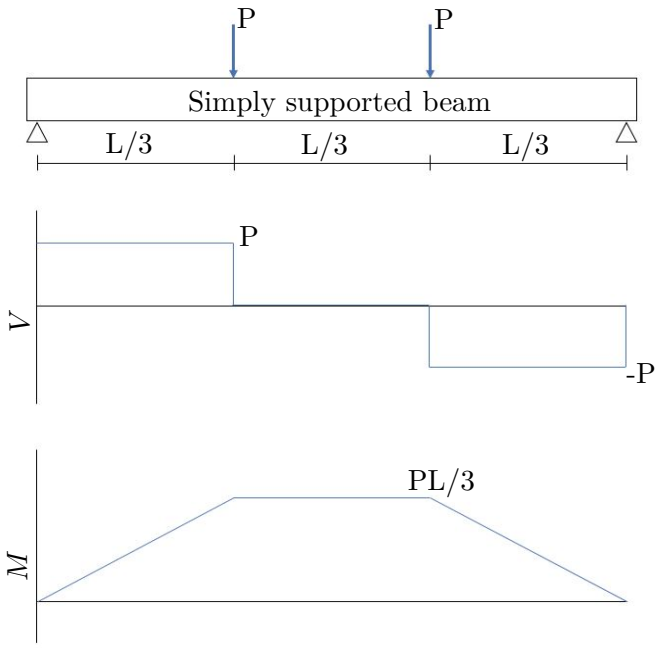

Figure 4.9: Schematic illustration of the shear and bending forces present when loading the specimens during the RB test

4.2.6.5 Loading rate

The displacement of the actuator was used to control the loading on the RB specimens, with a constant loading rate of 2 mm/min. At intervals of 15 kN (actuator load), the test was paused for approximately 5 minutes, keeping the actuator head in position. This was done to mark the cracks and measure the crack widths. The tests continued up until failure occurred (decrease in applied force).

4.2.7 Pull-out tests

4.2.7.1 Introduction

The pull-out (PO) test was performed in order to gain information on the bond performance between AAMs and reinforcement. The concept behind this test is to pull a steel bar from a cube specimen by applying a compression load on the face of the cube specimen where the embedded bar protrudes.

The PO test was done according to the ASTM C234, however, the standard was withdrawn in 2000. Due to the fact that there is no longer a standard available for the PO test, the ASTM C234 was used within this study as a valid comparison between AAMs and OPC concrete. The specification and procedures for the PO test were obtained from a previous study done by De Villiers, (2015a).

The PO test was performed on the same AAM mixes and OPC mixes as for the reinforced beam tests. Two PO specimens were tested for both the 12 mm and 16 mm reinforcement bars. A constant embedded length of 3ϕ was used, with ϕ taken as the nominal bar diameter. Thus, the embedded lengths for the 12 mm and 16 mm reinforcement were 36 mm and 48 mm, respectively.

4.2.7.2 Pull-out specimens

The PO specimens consisted of a reinforcement bar embedded into a 150 mm cube, as shown in Figure 4.10. The 500 mm reinforcement bar extended 330 mm from the one side of the cube, referred to as the loaded-end. The top 70 mm of the bar on this side was threaded in order to fix the specimen to the testing machine. The bar also protruded 20 mm on the other side of the specimen, referred to as the free-end. This was done to measure the bar slip without it being influenced by the elongation of the bar, as the slip on the loaded-end includes the slip and the elongation of the bar.

The embedded length was taken from the free-end side, while tape was used to de-bond the rest of the bar from the concrete. This ensured that the bond stresses within the embedded length were not influenced by the compression forces at the loaded-end.

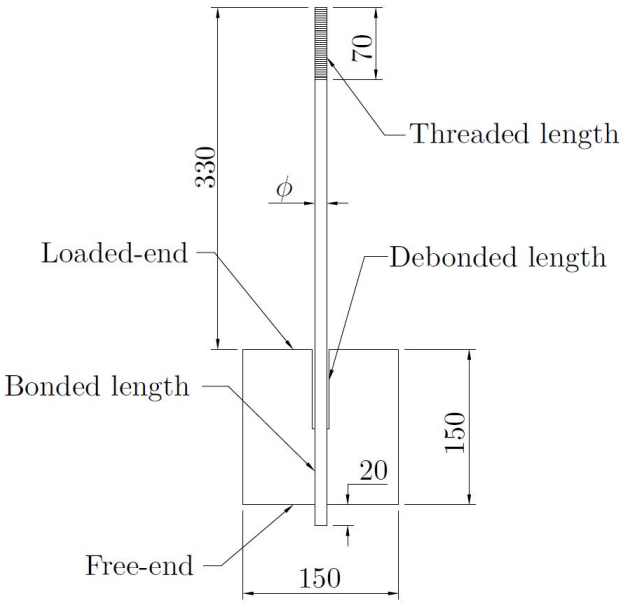

Figure 4.10: PO specimen dimensions

As mentioned before, an embedded length of 3ϕ was used for all of the specimens. According to Farghal Maree et al., (2014), the ASTM C234 specified an embedded length of 5ϕ, while other studies tested embedded lengths between 3ϕ and 5ϕ. However, a short embedded length was chosen to ensure that pull-out failure will occur, as longer embedded length could cause splitting failure. The splitting failure is due to stress build up and the formation of secondary cracks (Dae-Jin et al., 2014; De Villiers, 2015a).

Wooden moulds were used to cast the PO specimens, as shown in Figure 4.11a. Figure 4.11b shows a PO specimen after it was demoulded.

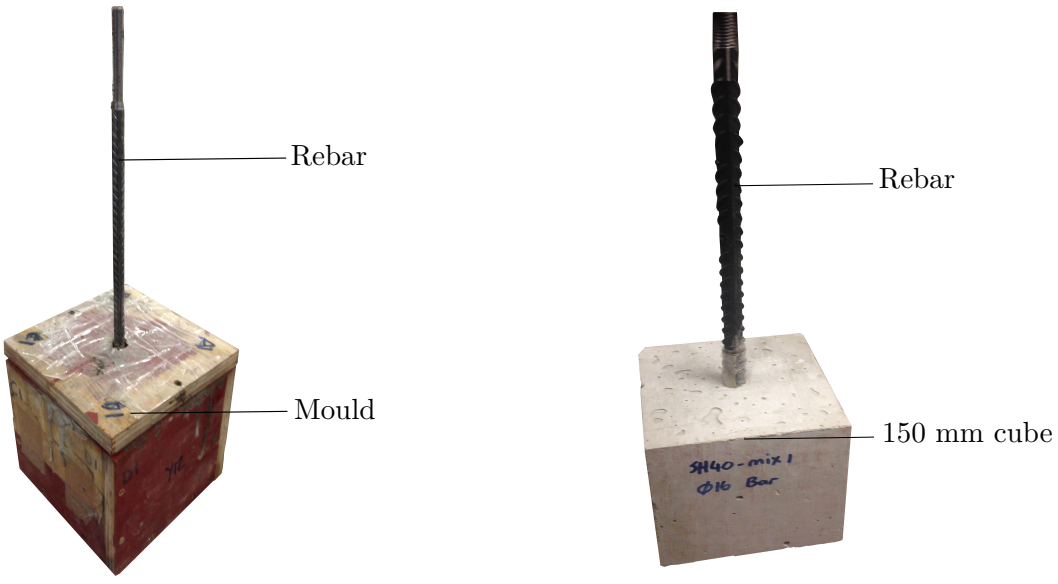

(a) (b)

Figure 4.11: (a) PO specimen moulds, and (b) Demoulded PO specimen

4.2.7.3 Testing machine and setup

The PO specimens were tested in the Zwick Universal Testing Machine with a capacity of 250 kN. The testing machine was adjusted in order to fit and test the specimens, as shown in Figure 4.12. This was done by removing the bottom clamp, enabling the specimen reinforcement bar to pass through the loading platform. This also ensured that the platform could exert a compression load on the top face of the PO specimen. The threaded top end of the bar was securely connected to the top clamp with a 20 mm plate, washer and bolt. This connection is showed in Figure 4.13a. The 12 mm bars were threaded to take a M10 nut, while a M16 nut was used for the 16 mm bars. The reduction in nominal diameter was taken into account during the design of the test, since there is a smaller cross sectional area to handle the tensile forces. Thus, for the 12 mm bars, a diameter of 8 mm (both the thread reduction and the thread depth were subtracted from the nominal bar diameter) was used to calculate the ultimate force.

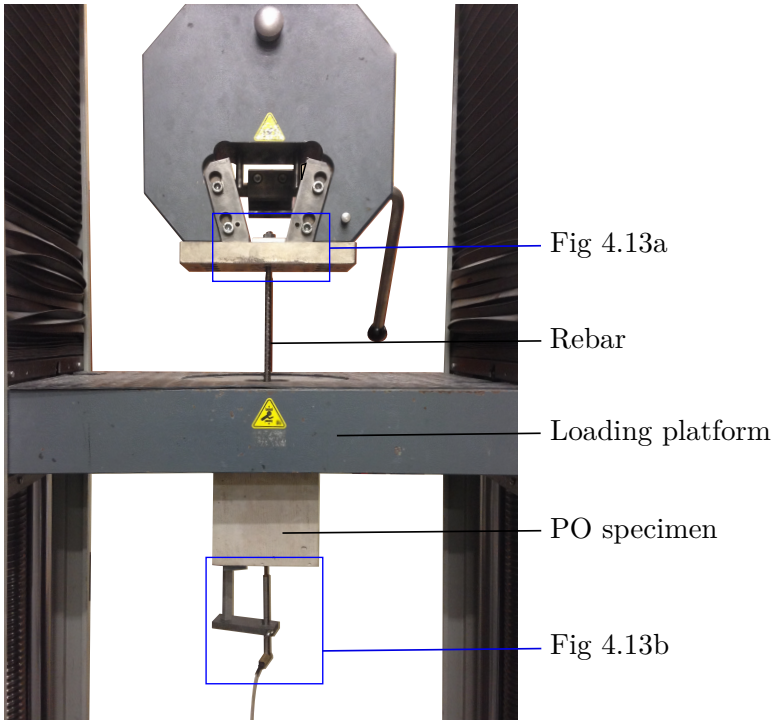

Figure 4.12: PO test setup showing the PO specimen fixed within the testing machine

A LVDT was fixed to the bottom of the specimen with a specially design LVDT bracket, as shown in Figure 4.13b. A 8 mm hole was drilled into the specimen to connect the LVDT bracket with a 8 x 40 mm screw and a wall plug inserted into the drilled hole. The hole was carefully drilled in the corner to avoid damage and cracks, which could influence the test, near the reinforcement bar. The bracket ensured that the LVDT with a stroke length of 10 mm, could be positioned over the free-end of the bar. During preparation, a slot was drilled into the free-end of the bar, which ensured that the LVDT could not slip from the bar.

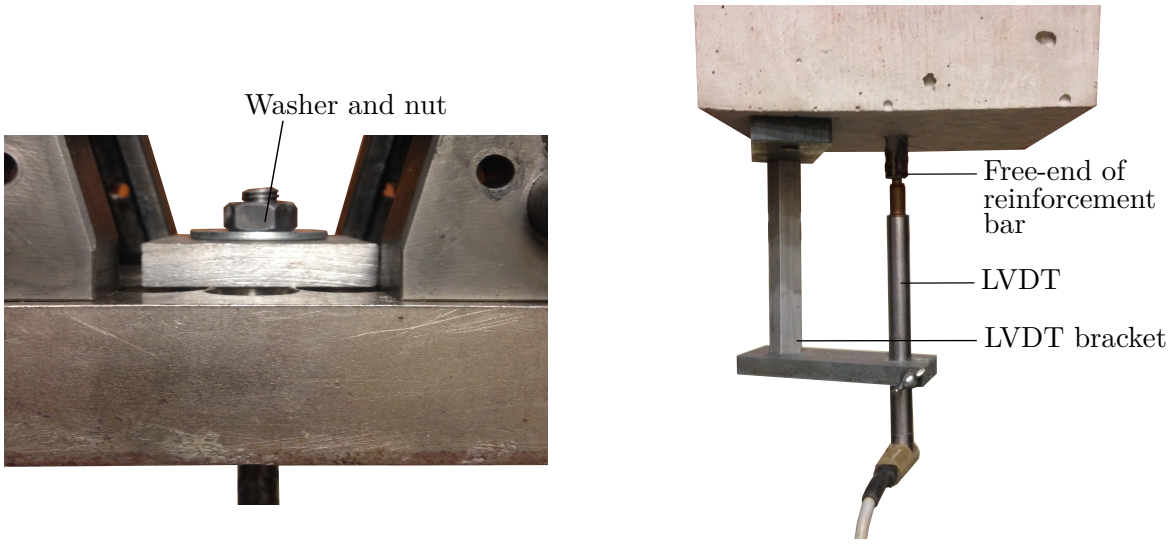

(a) (b)

Figure 4.13: (a) Connection of PO reinforcement bar with a washer and a nut, and (b) Free-end LVDT setup with specially designed positioning bracket

4.2.7.4 Loading rate

A displacement controlled loading rate of 0.1 mm/s was used for the PO test. This loading rate was also used by De Villiers, (2015a) and proved to be sufficient for the PO test in this study. The displacement of the crosshead (loaded-end) was used to control the loading rate.

4.3 Material specifications

The mechanical properties of AAMs are highly dependent on the materials that is used within the matrix. The chemical composition of these different materials also influences the mechanical properties. Therefore, it was important to ensure that the various materials remained consistent throughout all the mixes.

The materials that was used for both AAM mixes and OPC mixes are given in this section, which includes the origin and properties of the materials.

4.3.1 Aggregates

Fine- and coarse aggregate were used to produce both AAM mixes and OPC mixes. The fine- and coarse aggregates, which was obtained from a local company in Stellenbosch, are given in the following sections.

4.3.1.1 Fine aggregates

All the mixes contained a fine natural sand, locally known as Malmesbury sand. The grading of sand is given in Figure 4.14. The grading and the fineness modulus was determined according to SANS 201, (2008), while the relative density was determined according to SANS 5844, (2014). The fineness modulus and relative density are given in Table 4.1.

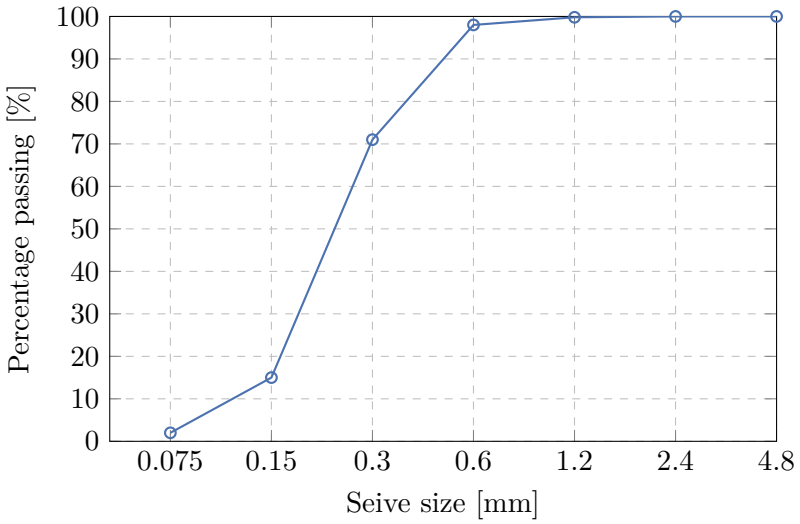

Figure 4.14: Grading of Malmesbury sand

4.3.1.2 Coarse aggregates

Two types of coarse aggregate was used in this study, namely Greywacke stone and Sand stone. The size of the Greywacke stone was also varied between 6 mm and 13 mm, while only 13 mm Sand stone was used. The majority of mixes consisted out of the 13 mm Greywacke stone. The relative densities of the coarse aggregates, as given in Table 4.1, were determined according to SANS 5844, (2014).

Table 4.1: Aggregate properties

Aggregate	Fineness modulus	Relative density
Fine Malmesbury sand	1.16	2.59
6 mm Greywacke stone	-	2.73
13 mm Greywacke stone	-	2.69
13 mm Sand stone	-	2.60

4.3.2 Binder materials

As mentioned in Section 2.3.1, there are several materials which can be used as the binder material for AAMs. In this study, slag and fly ash was used as binder material. Cement was

also used in some of the AAM mixes with alternative activators. The binder material for normal OPC concrete consists mainly out of cement, with fly ash, slag, and limestone generally used as extenders (Grieve, 2009). In this study, cement and limestone was used as binder material for the OPC mixes. These binder materials and their properties will be discussed in this section.

4.3.2.1 Slag

The Ground Granulated Corex slag (GGCS) used in this study, was obtained from PPC (Pretoria Portland Cement Co.). The slag was produced at the Saldanha Steel Factory in the Western Cape. The chemical composition of the slag is shown in Table 4.2. The slag had a relative density of 2.72.

4.3.2.2 Fly ash

The fly ash (FA) that was used, referred to as DuraPozz, was obtained from Ash Resources. DuraPozz is classified as ASTM Class F fly ash and complies with the chemical and physical requirements of SANS 50450-1, (2014), Category S. Therefore, more than 88 % of the fine particles were smaller than 45 μm. The chemical composition of the fly ash is given in Table 4.2. A relative density of 2.14 was obtained for the fly ash.

4.3.2.3 Cement

All of the mixes containing cement was produced with a CEM II/B-M 42.5N Portland cement. The cement was also obtained from PPC. The CEM II/B-M consists out of 66 % cement clinker, 28 % slag and 6 % limestone. The chemical composition of the cement is shown in Table 4.2, while the relative density was 3.14.

4.3.2.4 Limestone

Limestone was also incorporated in some of the OPC mixes. This was done to obtain a lower strength concrete, as limestone acts as a filler and only participate to a small extent in the chemical reactions of the concrete (Grieve, 2009). The limestone that was used is a dolomitic filler, referred to as Filla 15 (Cape Lime). The limestone contains ± 42 % $MgCO_3$ and 52 % $CaCO_3$, with the remainder consisting out of impurities which mainly constitutes silica. The relative density of the limestone was 2.6.

Table 4.2: Chemical composition of binder materials

Compostion	GGCS	FA	Cement	Limestone
SiO_2	33.27	56.00	22.73	6.30
Al_2O_3	13.90	29.55	6.50	2.93
CaO	35.57	4.61	57.34	27.06
Fe_2O_3	1.19	3.58	2.42	0.68
MgO	12.07	1.16	4.16	19.05
K_2O	0.68	0.89	0.64	1.03
MnO	0.04	0.03	0.06	0.02
Cr_2O_3	0.00	0.03	0.02	0.00
Na_2O	0.19	0.21	0.27	0.10
P_2O_5	0.01	0.48	0.11	0.04
TiO_2	0.48	1.56	0.28	0.12
L.O.I.	-1.48	0.36	2.88	40.10

4.3.3 Activators

Three alkaline activators were used in the this study. The combination of sodium silicate and sodium hydroxide was used as the main activator. Sodium silicate and sodium carbonate were used as alternative activators. The properties of these activators are given in the following sections.

4.3.3.1 Sodium silicate

The sodium silicate (SILCHEM 3379) was obtained from Protea chemicals, Western Cape. The sodium silicate had a chemical composition of 8.81 % Na_2O, 29.04 % SiO_2 (SiO_2:Na_2O = 3.3) and 62.15 % water by mass. The relative density of the sodium silicate was 1.395.

4.3.3.2 Sodium hydroxide

The sodium hydroxide was obtained from Protea chemicals, Western Cape. The sodium hydroxide was in flake form, with a specific gravity of 2.13 and a purity of 98 %. As mentioned in Section 4.1.1, the sodium hydroxide solutions were prepared to the specific concentrations by dissolving the flakes in tap water.

The following calculations were done to obtain the required mass percentage of sodium hydroxide flakes for each of the concentrations:

1. The mass of NaOH per litre of solution was determined. This was done by multiplying the specific concentration with the molecular weight of sodium hydroxide (40 g/mol). This

value is then also divided by the purity of the sodium hydroxide. Thus, the mass of NaOH per litre solution for an 8 M concentration is 8 x 40 = 320 g/l. Dividing by the sodium hydroxide purity, yields a value of 326.5 g/l.

2. The relative density was determined by adding the mass of NaOH per litre of solution to the amount of water per litre of solution. The amount of water per litre of solution was obtained with the volume of NaOH per litre of solution, which is calculated by dividing the mass of NaOH per litre of solution by the specific gravity of sodium hydroxide. The mass of water per litre of solution for an 8 M concentration is 1 - 0.327/2.13 = 0.847 kg/l, which will result in a relative density of 0.327 + 0.847 = 1.174.

3. The mass percentage of sodium hydroxide flakes is calculated by dividing the mass of NaOH per litre of solution with the relative density. This value is 0.327/1.174 = 27.83 % for an 8 M concentration.

Table 4.3 provides all the necessary values obtained with the above calculations for each of the concentrations that was used in this study. The last two rows of the table contains the mass percentages of sodium hydroxide flakes and water, per litre solution.

Table 4.3: Sodium hydroxide calculations

NaOH concentration (M)	4	6	8	12
Mass of NaOH per litre (kg)	0.163	0.245	0.327	0.49
Relative density	1.09	1.13	1.17	1.26
Mass % NaOH	15.03	21.67	27.83	38.88
Mass % water	84.97	78.33	72.17	61.12

4.3.3.3 Sodium carbonate

A powder form of sodium carbonate was obtained from Kimix chemicals, Western Cape. The sodium carbonate had a 100 % purity. The specific gravity and molecular weight for sodium carbonate are 2.54 and 105.99 g/mol, respectively. The same calculations, as discussed in Section 4.3.3.2 for sodium hydroxide, were done for sodium carbonate. However, the highest concentration that can be obtained for sodium carbonate is 2 M. This is due to solubility of sodium carbonate (30.7 g/100 g water at 25 °C) (Lide, 2005). The values for sodium carbonate calculations are given in Table 4.4.

Table 4.4: Sodium carbonate calculations

Na_2CO_3 concentration (M)	2
Mass of Na_2CO_3 per litre (kg)	0.212
Relative density	1.13
Mass % Na_2CO_3	18.78
Mass % water	81.22

4.3.4 Reinforcement

The reinforcement was selected from a batch supplied by D&E Steel, Western Cape. As mentioned, the reinforcement used in this study was high tensile steel with diameters of 12 mm and 16 mm. Additionally, smooth mild steel was used for the stirrups within the beams. The stirrups had a diameter of 6 mm. High tensile steel and mild steel have characteristic yield strengths of approximately 450 MPa and 250 MPa, respectively (Robberts et al., 2010).

Measurements were taken in order to obtain the dimensions of reinforcement geometry as indicated in Figure 4.15. This was done with a vernier scale. The reinforcement dimensions that was measured are given in Table 4.5.

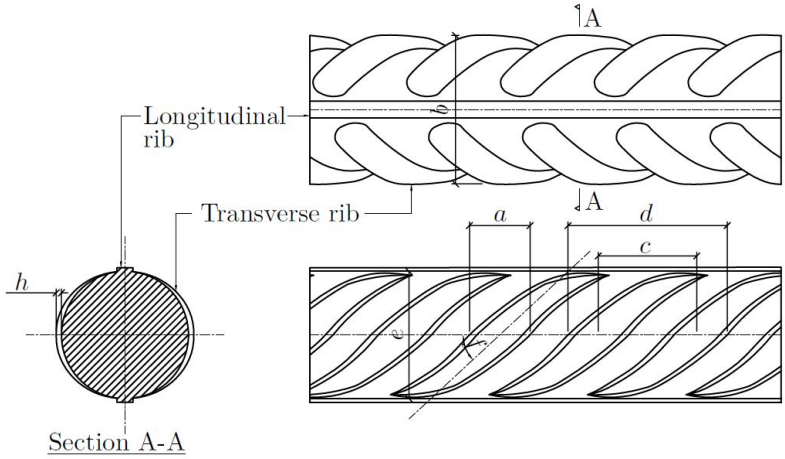

Figure 4.15: Drawing of the reinforcement geometry with the measured dimensions

Table 4.5: Reinforcement dimensions as indicated on Figure 4.15

Dimensions [mm]	Ø12 mm	Ø16 mm
a - rib with [mm]	3.55	5.5
b - outside bar diameter [mm]	11.59	18.32
c - center rib spacing [mm]	7.32	11.64
d - outer rib spacing [mm]	10.87	17.14
e - inside bar diameter [mm]	10.96	15.59
h - rib height [mm]	0.32	1.37
Ribs per meter length	137	86

Tensile tests, according to SANS 6892-1, (2010), were also conducted, in order to obtain the actual yield strength and elastic modulus of the reinforcement. The Zwick Universal Testing Machine was used to perform the tensile tests. The test setup is shown in Figure 4.16.

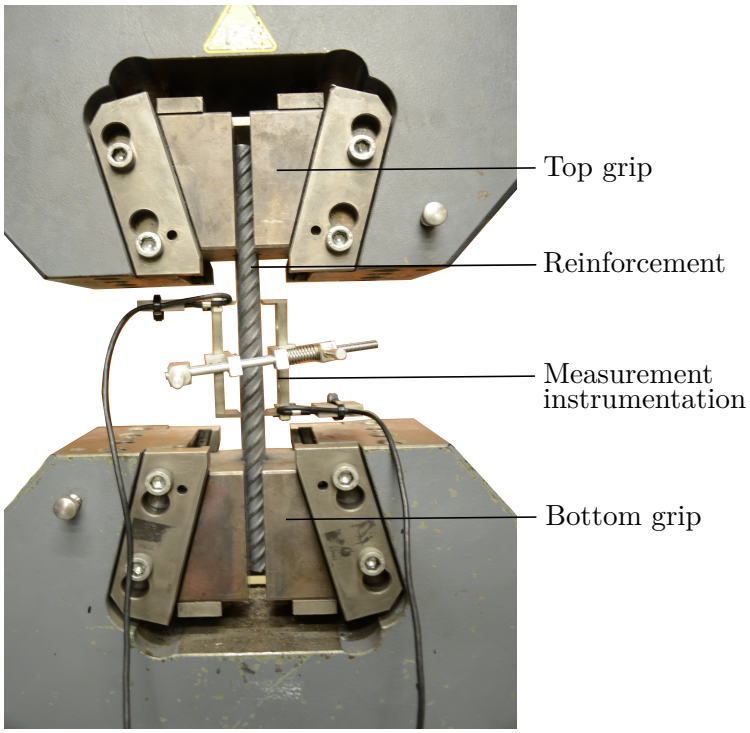

Figure 4.16: Tensile test setup for reinforcement

Three specimens were tested for both the 12 mm and the 16 mm reinforcement. These specimens were cut to a length of 300 mm. An extensometer, was fixed onto the specimens at a gauge length of 80 mm, to determine the deformation of the bar. Before the specimens were loaded at a constant loading rate of 600 N/s, a pre-load of 1000 N was applied. This was done to ensure that the specimens were securely fixed within the grips of the machine.

The yield stress and elastic modulus was determined from the stress-strain curve, as shown in Figure 4.17. The strain at each point was calculated by dividing the displacement measured by the extensometer with the original gauge length, while the applied force was divided by the cross sectional area to obtain the applied stress. The gradient of the linear potion was used as the elastic modulus (E_s) for the reinforcement. The yield stress (f_y) was determined with the offset method as described in ASTM E8/E8M-09, (2011). A line was plotted on the stress-strain graph, using the elastic modulus (E_s) as the gradient and intersecting the x-axis (strain) at 0.002 mm/mm (0.2 %). The intersection point between the offset line and the stress-strain curve was assumed to be the yield stress. The yield stress and elastic modulus of the reinforcement are given in Table 4.6.

Table 4.6: Reinforcement mechanical properties

Properties	Ø12 mm	Ø16 mm
Yield stress [MPa]	558	551
Elastic modulus [GPa]	222	204

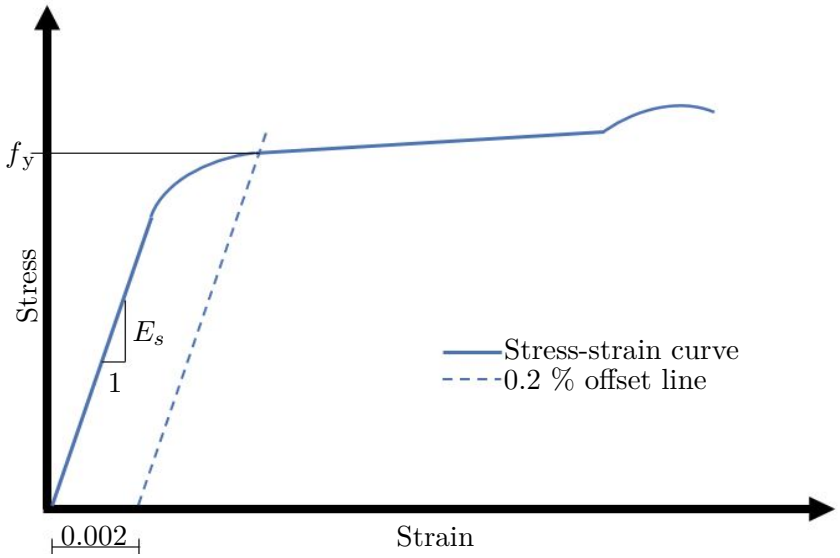

Figure 4.17: Determination of yield stress and elastic modulus

4.4 Mix Design

As mentioned in Chapter 1, specific mix design methods, as for OPC concrete, has not yet been established in order to produce AAM mixes. There are several methods that are used to design an OPC concrete mix. One of these methods is the C&CI method. When this method is used, the concrete is designed for a specific compressive strength. The water-to-cement ratio is the main factor that contributes to the strength of OPC concrete (Addis et al., 2009). AAMs have several constituents which influence the compressive strength. This makes it difficult to obtain a specific design strength for AAMs.

In this study, several AAM parameters and their effect on the strength were investigated. These parameters include: the type of activator; calcium content; activator concentration; activator dosage; activator modulus; and the aggregate content. Therefore, the mixes were designed to obtain specific values for each of the mentioned parameters.

Mix designs from previous research were used as a guideline to design and obtain typical constituent proportions for the new mixes which were used in this study. Initial trial mixes were made to obtain the aggregate and binder proportions, which were used throughout for all of the mixes. The amount of additional water was also determined with these trial mixes. The amount of aggregate, binder and additional water remained constant, while the amount of the alkaline activators were varied to obtain the required dosages and modulus values for the different concentrations.

The required dosages for the mixes were calculated by dividing the total mass of Na_2O within the activators with the total mass of binder within a mix. The mass of Na_2O within each of the activators was calculated by multiplying the mass of the individual activator with the percentage of Na_2O within the that activator. The sodium silicate contained 8.81 % Na_2O, while

solid forms of sodium hydroxide and sodium carbonate contained 77.5 % Na_2O and 58.5 % Na_2O, respectively. Therefore, the mass percentages as calculated in Section 4.3.3 were multiplied by the percentage of Na_2O for sodium hydroxide and sodium carbonate, which was then multiplied with the mass of the activator.

The activator modulus was calculated by dividing the SiO_2 mass with the mass of Na_2O. Similar to the Na_2O mass, the mass of SiO_2 was calculated by multiplying the mass of activator with the percentage of SiO_2 within that activator. Sodium silicate was the only activator containing SiO_2, with a percentage of 29.04.

The mass of the activators were varied until the required dosage and modulus values were obtained. Therefore, a mix with sodium silicate and sodium hydroxide as the activators; a binder content of 450 kg/m^3; a concentration of 8 M; a dosage of 5 %Na_2O/binder; and a modulus value of 1, would result in sodium silicate having a mass of 77 kg/m^3, while the sodium hydroxide has a mass of 72 kg/m^3, as shown below:

- 77 x 8.81 % = 6.78 kg Na_2O within the sodium silicate
- 72 x 77.5 % x 27.83 % = 15.53 kg Na_2O within the sodium hydroxide
- 77 x 29.04 % = 22.36 kg SiO_2
- Dosage = (6.78 + 15.53)/450 = 5 %Na_2O/binder
- Ms = 22.36/(6.78 + 15.53) = 1

It should be noted that there was variation in the volume between all of the mixes. This was due to the different alkaline activator amounts used for each of the mixes, while the other constituents remained constant. Effectively, some of the other constituents should have been changed to get the same volume, similar to the fine aggregate that is varied when designing OPC concrete. However, these constituents remained constant in order to compare the different mixes. All of the mixes still had a volume of approximately a 1000 l.

The initial trial mixes and the results that was obtained for them is first discussed in this section. The final mixes with the different values that was chosen for each of the parameters is then given, which is followed by the beam and pull-out mixes. An explanation is also given on the notation of the mixes, with a summary of all the mixes provided in Apendix D.

4.4.1 Initial trial mixes

Three preliminary mixes were designed and tested. This was done in order to obtain a mix with the appropriate properties of which the parameters (as given in the next section) could be changed. The workability and compressive strength, as discussed in Section 4.2, was tested to achieve this. The compressive strength was tested at 7 days.

The effect of compaction and curing methods were also established. Some of the cubes were vibrated, while others were only filled. Some of the cubes were also placed in the climate

controlled room right after they were cased. These cubes were then demoulded approximately 24 hours later with the cubes which was left in the laboratory to harden. This was done to determine whether temperatures influence the initial 24 hours of curing.

The preliminary mixes, as given in Table 4.7, was based on previous research. The binder content consisted out of 40 % slag and 60 % fly ash. The mixes were designed in order to obtain a dosage of 5 %Na_2O/binder and a modulus value of 1. The aggregate content varied from 70 % to 72 %. The second mix was obtained by reducing the water content and increasing the aggregate content of the first mix. This was done due to the workability and consistency of the first mix not being suitable. The third mix was obtained by adding all the extra water to the sodium hydroxide; therefore, reducing the sodium hydroxide concentration. The first two mixes both had a concentration of 8 M, while the third mix had a concentration of 3.6 M. The concentration was the only parameter that was changed in the third mix. This was done to determine the effect of adding the extra water separately or with the sodium hydroxide.

Table 4.7: Initial mixes

Constituents (kg/m^3)	Initial mix 1	Initial mix 2	Initial mix 3
Coarse aggregate	1025	1030	1030
Fine aggregate	655	690	690
Slag	180	180	180
Fly ash	270	270	270
Sodium silicate	77	77	77
Sodium hydroxide	72	72	147
Water	90	75	0

The first trial mix was very flowable giving a slump flow diameter of 615 mm. It was observed that the paste did not hold the stone while it was flowing. This is a problem, because the final matrix will not be consistent. Segregation was also observed while the moulds were filled. Therefore, the water was reduced by 25 kg/m^3 in the second preliminary mix to make the mix more consistent and eliminate segregation. The mix was still flowable, but a lower slump diameter of 490 mm was obtained. This mix showed better results in terms of both the consistency and segregation. The second mix kept the stone within the paste while it was flowing, as shown in Figure 4.18. Both mixes had relatively the same finishability and setting times. The workability and consistency of the third mix did not change much from the second mix, with a slump flow diameter of 495 mm and no segregation occurring. Again, the finishability and the setting times between the second and third mix was the same.

(a) (b)

Figure 4.18: Slump flow and consistency of initial mix 2

The first mix had considerably lower strength than the second, with values of 11.5 MPa and 23.7 MPa, respectively. This is attributed to the reduction of water in the second mix. The compressive strength of second and third mixes were exactly the same. This indicates that it makes no difference whether the extra water is added separately or with the sodium hydroxide. It also indicates that the concentration of the sodium hydroxide should take the extra water into account.

The strength of the mixes were not influenced by the compaction, as similar strengths were obtained for the cubes which were vibrated and the ones which were not vibrated. However, segregation occurred in the vibrated cubes, as the top layer from the casting side only contained paste and no stone. It was also found that the cubes left in the climate controlled room had the same strengths as those left to harden in the laboratory. Thus, it can be said that the controlled temperature of 24 °C for the first 24 hours of hardening does not influence the strength.

It was decided to use the the second mix as the reference mix, due to its favourable properties. The second mix was flowable without any segregation. It also had a higher strength than the first mix, due to the reduction in water. Even though similar strengths were obtained for the second and third mixes, it was decided that the extra water and the sodium hydroxide should be considered separately. This is due to the specific concentrations and dosages (%Na_2O/binder) that wanted to be obtained, as well as the extra water providing workability. It should be noted that the extra water actually reduces the concentration of the sodium hydroxide.

In conclusion: a stronger mix was obtained with a reduction in extra water; similar strengths are obtained when all of the extra water is added to the sodium hydroxide; the compaction does not influence the strength, but segregation occurs with vibration; and the strength is also not influenced by the temperature during the first 24 hours of curing. In the next section, the reference mix and the changing parameters are given.

4.4.2 Final mixes

As mentioned, the parameters which were varied are: the type of activator; calcium content; activator concentration; activator dosage; activator modulus; and aggregate content. These parameters were varied according to the reference mix, as given in Table 4.8.

Table 4.8: Reference mix

Constituents	kg/m^3
Coarse aggregate	1030
Fine aggregate	690
Slag	180
Fly ash	270
Sodium silicate	77
Sodium hydroxide	72
Water	75

The reference mix contained 72 % aggregate of which 60 % was coarse aggregate and 40 % fine aggregate. 13 mm Greywacke stone was used for the coarse aggregate. The binder material consisted out of 40 % slag and 60 % fly ash. The solution (sodium silicate, sodium hydroxide and water) to binder ratio was 0.5. The solution consisted out of 66.5 % alkaline activator, with a sodium silicate to sodium hydroxide ratio of 1.07. The sodium hydroxide had a concentration of 8 M. The alkaline activator had a dosage of 5 %Na_2O/binder and a modulus value of 1.

The different parameters which were changed are discussed in the following sections.

4.4.2.1 Type of activator

As mentioned before, two different types of alternative activators were used. These activators include: sodium silicate and sodium carbonate, which are not as hazardous as sodium hydroxide.

For the sodium silicate as the activator, two different mixes were tested. The solution to binder ratio was kept constant at 0.5 for the first, resulting in an activator dosage of 2.9 %Na_2O/binder. For the second, the solution to binder ratio was increased in order to obtain the same activator dosage as the reference mix (5 %Na_2O/binder). Due to these mixes only containing sodium silicate, the activator modulus was constant with a value of 3.3.

Three mixes were tested for the sodium carbonate activator. A combination of sodium silicate and sodium carbonate were used for two of the mixes, while the other mix only contained sodium carbonate. The solution to binder ratio, sodium carbonate concentration, dosage and modulus were the same for all three mixes at 0.5, 2 M, 3.5 %Na_2O/binder and 1, respectively. One of the mixes with sodium silicate and sodium carbonate as activators, only contained slag as the binder, while the other two mixes had the same binder content as the reference mix (40 % slag and 60 % fly ash).

OPC was also used with the alternative activators in order to improve the results. For these mixes, 20 % of the fly ash was replaced by OPC. Therefore, the binder consisted out of 40 % slag, 40 % fly ash and 20 % OPC. This was only done for the sodium silicate mix with the solution to binder ratio of 0.5 and a dosage of 2.9 %Na_2O/binder, as well as the mix with the combination of sodium silicate and sodium carbonate.

4.4.2.2 Calcium content

The main source of calcium in the AAM mixes were from the slag. Thus, the slag content was varied between 20 % and 40 % of the binder content. The total binder content remained constant at 450 kg/m^3. This resulted in a CaO content of 48.61 kgCaO/m^3 and 76.47 kgCaO/m^3 for the 20 % and 40 % slag, respectively. The rest of the mix variables were tested for both 20 % and 40 % slag content.

4.4.2.3 Activator concentration and dosage

The sodium hydroxide concentration was varied between 4 M, 6 M, 8 M and 12 M. With the reference mix having a concentration of 8 M and a dosage of 5 %Na_2O/binder, three different dosages were obtained by keeping the modulus value and the solution/binder ratio constant, while changing the concentration to 4 M, 6 M and 12 M. This resulted in an activator dosage of 3.5 %Na_2O/binder corresponding to the 4 M concentration, a dosage of 4.3 %Na_2O/binder corresponding to the 6 M concentration and a dosage of 5.8 %Na_2O/binder corresponding with the 12 M concentration. These dosages were used throughout the rest of the variations. The concentrations were chosen according to previous research.

The dosages were also varied between 3.5 %Na_2O/binder, 4.3 %Na_2O/binder, 5 %Na_2O/binder and 5.8 %Na_2O/binder, while keeping the concentration and activator modulus constant. This was done for the 4 M, 6 M, and 8 M concentrations, while the 12 M concentration was tested at dosages of 3.5 %Na_2O/binder, 5 %Na_2O/binder and 5.8 %Na_2O/binder. The modulus value remained constant at 1. It should be noted that not all of the above dosages were tested for the binder consisting out of 20 % slag, due to observations that were made for the 40 % slag mixes.

4.4.2.4 Activator modulus

In previous research, an optimum activator modulus value of approximately 1 was obtained when the activator modulus was varied between 0.5 and 3 (Adam, 2009; Bakharev et al., 1999). Therefore, the activator modulus was varied between 0.75, 1 and 2 for this study, while the other parameters were kept constant. This was done for the dosage of 3.5 %Na_2O/binder corresponding to the 4 M concentration, the dosage of 5 %Na_2O/binder corresponding to the 8 M concentration, and the dosage of 5.8 %Na_2O/binder corresponding to the 12 M concentration. The 4.3 %Na_2O/binder dosage corresponding to the 6 M concentration was not tested, as the 6 M concentration was not part of the original scope of this study.

4.4.2.5 Aggregate content

The influence of the coarse aggregate content was investigated in this study. As mentioned in Section 4.3.1.2, two different types of coarse aggregate were used, namely Greywacke stone and Sand stone. The percentage of coarse aggregate was varied between 50 %, 60 % and 70 % for both the types of stone. The Greywacke stone size was also varied between 6 mm and 13 mm, while only a 13 mm Sand stone was used. The other parameters remained constant as was used in the reference mix, including the total aggregate content.

4.4.3 Beam and Pull-out mixes

The results that was obtained for all of the mixes as discussed in Section 4.4.2, was used to determine the beam and pull-out mixes. It was decided to test two AAM mixes and compare these mixes against OPC concrete with similar strengths. The reference mix as given in Section 4.4.2 was used for the first AAM mix, while the slag content of the reference mix was reduced to 20 % for the second AAM mix. The AAM mixes and OPC mixes are given in Table 4.9. These mixes were used for both beam and pull-out tests. The first AAM mix was compared with the first OPC mix, while the second AAM mix was compared with the second OPC mix.

Table 4.9: Beam and pull-out mixes

Constituents (kg/m^3)	AAM-mix1	AAM-mix2	OPC-mix1	OPC-mix2
Coarse aggregate	1030	1030	1100	1100
Fine aggregate	690	690	769	827
Slag	180	90	-	-
Fly ash	270	360	-	-
Cement	-	-	328	232
Limestone	-	-	-	22
Sodium Silicate	77	77	-	-
Sodium hydroxide	72	72	-	-
Water	75	75	190	190

The C&CI method as given by Addis et al., (2009), was used to design the OPC mixes. The strengths that was obtained for the two AAM mixes were used to determine the water-to-cement ratio for each of the OPC mixes. A few trial mixes were made and adjusted to obtain the final mixes as given in Table 4.9. This resulted in a water-to-cement ratio of 0.58 for the first OPC mix, while the second OPC mix had a water-to-cement ratio of 0.82. The binder for the second mix also contained limestone with the cement. This was done to obtain a lower strength without reducing the water-to-cement ratio.

4.4.4 Specimen Notation

A special notation is used throughout this study to identify the AAM specimens according to the alkaline activator used, binder content, concentration, dosage, activator modulus and aggregate content. These variables and their corresponding codes are listed in Table 4.10.

Table 4.10: Notation used to identify AAM specimens

	Description	Code
Alkaline activator	Sodium silicate	S
	Sodium hydroxide	H
	Sodium carbonate	C
Binder content	40 % slag within the binder	40
	20 % slag within the binder	20
	20 % OPC also included in the binder	(20)
Activator concentration	The concentration is indicated with a "C" followed by the molarity of the concentration. The molarities varied between 2 M, 4 M, 6 M, 8 M and 12 M.	C#
Activator dosage	The dosages is indicated with a "N" followed by the percentage Na_2O/binder. The following dosages were tested: 2.9 %Na_2O/binder, 3.5 %Na_2O/binder, 4.3 %Na_2O/binder, 5 %Na_2O/binder and 5.8 %Na_2O/binder.	N#
Activator modulus	The activator modulus is indicated with a "M" followed by the SiO_2/Na_2O ratio. The modulus ratios of 0.75, 1 and 2 were used.	M#
Aggregate content	Greywacke stone is indicated by a "G", while sandstone is indicated with a "S". These letters are followed by the percentage course aggregate within the total aggregate content and varied between 50 %, 60 % and 70 %.	G# or S#
Aggregate size	6 mm Greywacke stone	6 mm

A specific notation format was used to assemble these codes. For example, the specimen code SH-40-C8N5M1-S60 indicates that: sodium silicate and sodium hydroxide was used as activators; the binder content consisted out of 40 % slag; the activator had a concentration of 8 M, dosage of 5 %Na_2O/binder and an activator modulus of 1; while the aggregate content consisted out of 60 % sandstone. If the stone content notation was omitted, the aggregate content of the reference mix was used (60 % Greywacke stone with a size of 13 mm). The concentration and the activator modulus could not be obtained for some of the alternative activator mixes. Therefore, the corresponding notations were omitted for these mixes.

The notations as given in Table 4.9, were used for the beam and pull-out mixes. All of the mixes that was tested are summarised in Appendix D. The constituent amounts for each mix is also included in this summary.

Chapter 5

Results and discussion: Mechanical properties

As stated in Chapter 4, several tests were conducted on 54 different mixes, in order to obtain a better understanding on the mechanical properties of AAMs and their influencing factors. These properties include: workability; compressive strength; density; elastic modulus; and the stress-strain relationship. The results for these tests are reported and discussed within this chapter. A summary of the results that was obtained for the mechanical properties of each mix, is also provided in Appendix A.

A statistical analysis was also performed on the results that was obtained for the compressive strength, density, elastic modulus and stress-strain relation. A single linear regression as well as a multiple linear regression was performed for the statistical analysis. The multiple regression was also done in order to observe the effect that the different variables have on one another. It should be noted that a full set of data, where all the parameters are tested at all levels, is required to perform a multiple regression analysis. However, due to limited time and practicality, the variables in this study were only tested at specifically chosen levels.

For the linear regression, the "R-squared" value and the p-value were obtained. The "R-squared" value gives an indication of how well the regression line approximates the real data points. The closer the "R-squared" value is to one, the stronger the regression line fits the data. If the regression line does not fit the data, the "R-squared" value will be close to zero. The p-value is the exact significance level within a statistical hypothesis. Therefore, the probability of obtaining a result that is equal to or more extreme than that observed when the null hypothesis is true. The null hypothesis refers to a statement that there is no relationship between specified variables. A small p-value (typically ≤ 0.05) will reject the null-hypothesis, therefore, indicating that a relationship exists between the variables. However, if the p-value is large (> 0.05), the null-hypothesis will not be rejected, resulting in no relationship between the variables.

The Beta values, p-values and "R-squared" value were obtained for the multiple regression. The multiple regression analysis produced an equation for the linear regression line, containing the effect of each of the variables. However, due to the variable having different units and quantities this line was normalised, which is represented by the Beta values. The "R-squared" value represents the fit of the multiple regression line to the data. The p-value again represents

the level of significance, but also includes the effect that the variables have on one another. Therefore, the p-value for the multiple regression is different to that of the single regression (Montgomery et al., 2007).

5.1 Workability

The results that was obtained for the workability of the AAM mixes are given in this section. These results include the slump flow diameters that were measured as well as the observations made on segregation and consistency.

Diameter slump flow readings of up to 770 mm were measured. However, for slump flow readings of more than 650 mm, segregation was generally observed. Segregation was indicated by the stone separating from the rest of the mix, due to the paste not being able to keep the stone intact while flowing. This typically occurred for the mixes with large solution to binder ratios.

5.1.1 Alkaline activator

The workability results for the alternative activator mixes are given in Table 5.1. As mentioned in Section 4.2.1, the normal slump test was performed on some of these mixes. These mixes were relatively stiff, with slump values ranging between 20 mm and 50 mm. However, mixes C-40-C2N3.5 and S-40-N5, gave diameter slump reading of 360 mm and 425 mm, respectively.

Table 5.1: The slump values of alternative activator mixes

Alternative activator mixes	mm
SC-40-C2N3.5M1	25
C-40-C2N3.5	Ø360
SC-100-C2N3.5M1	20
SC-40(20)-C2N3.5M1	-
S-40-N2.9	50
S-40-N5	Ø425
S-40(20)-N2.9	-

This indicates that the sodium silicate reduced the workability of the mixes containing sodium carbonate as an alternative activator. For the mixes with only sodium silicate as an alternative activator, the workability was improved with a higher solution to binder ratio.

The mixes that contained OPC (SC-40(20)-C2N3.5M1, S-40(20)-N2.9) were very dry and lumpy, as shown in Figure 5.1. Thus, the slump could not be measured for these mixes. The OPC within the binder could be the reason for these dry mixes. A larger amount of water is most probably necessary, due to the water requirement for cement hydration.

Figure 5.1: Alternative activator mixes containing OPC

5.1.2 Calcium content

The slag content contributed to the calcium content and was varied between 20 % and 40 % of the binder content. The workability decreased with an increase in slag content, as shown in Figure 5.2. This can also be observed in Figures 5.3 to 5.5. As mentioned in Section 2.3.1.2, the spherical shape of the fly ash is more mobile than the sharp slag particles, causing the fresh mix to flow easier. Therefore, the workability is improved with more fly ash in the binder.

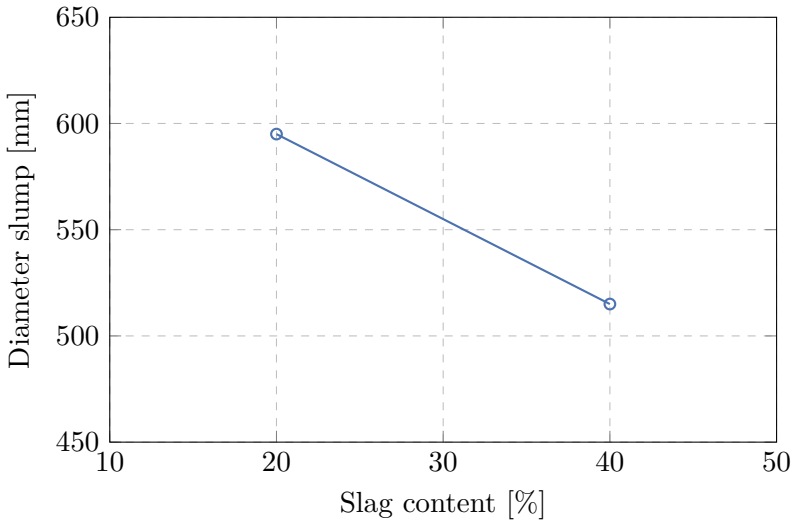

Figure 5.2: Influence of calcium content on the workability

5.1.3 Sodium hydroxide concentration

The influence of the sodium hydroxide concentration on the workability of the AAMs are given in Figure 5.3. It is evident that the workability decreased as the sodium hydroxide concentration

increased. Barnard, (2014) also obtained similar results.

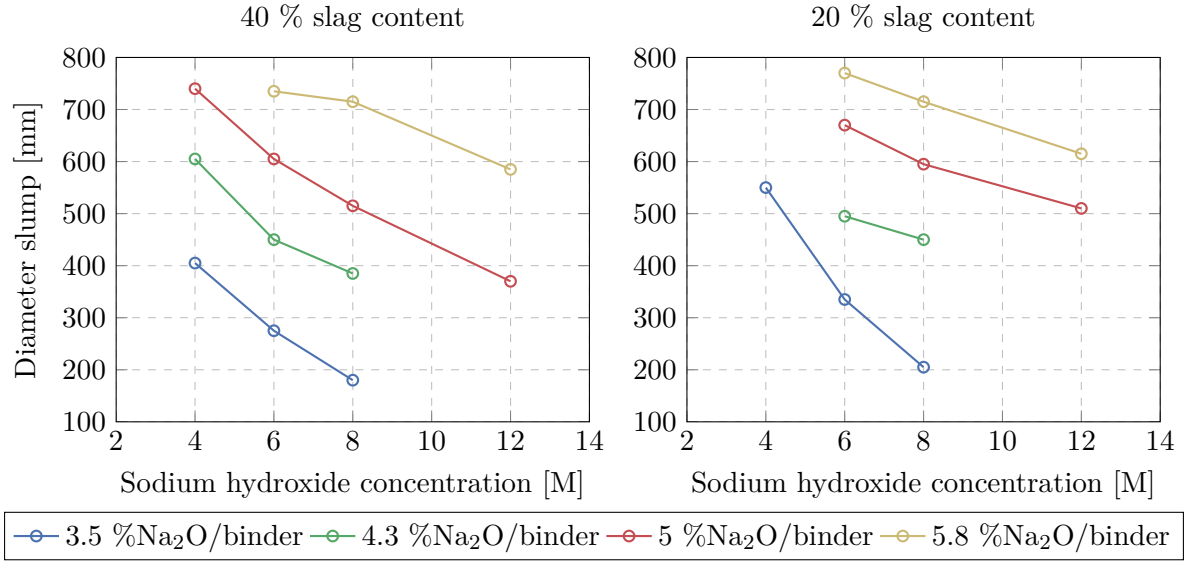

Figure 5.3: Influence of sodium hydroxide concentration on the workability

For the preparation of the sodium hydroxide, less water was added for higher concentration. Therefore, the solution to binder ratio reduced with higher concentrations (amount of sodium silicate remained constant), resulting in less flowable mixes.

5.1.4 Activator dosage

The workability results for the activator dosage are presented in Figure 5.4. The diameter slump measurements increased with an increase in activator dosage. This was mainly due to the solution to binder ratio that increased with dosage in order to obtain the same modulus value.

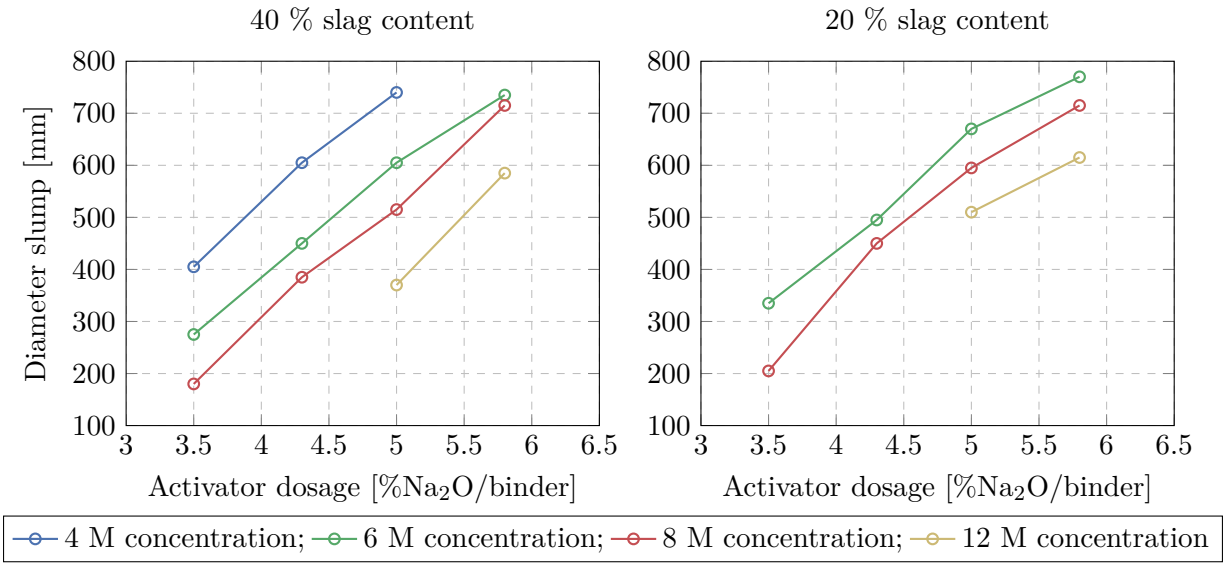

Figure 5.4: Influence of activator dosage on the workability

Mix SH-40-C4N5.8M1 was very flowable, while mix SH-40-C12N3.5M1 was very stiff. Therefore the slump measurements could not be taken for these mixes. Mix SH-40-C4N5M1 was also very flowable with a large amount of segregation. Again this was due to the solution to binder ratios, which were either to high or to low. Due to these workability results, the 20 % slag was not tested for these mixes (SH-20-C4N5M1, SH-20-C4N5.8M1 and SH-20-C12N3.5M1).

5.1.5 Activator modulus

Figure 5.5 illustrates the workability that increased as the activator modulus increased. Again, a larger solution to binder ratio was obtained with the higher modulus values. Therefore, the flowability of the mixes increased as the activator modulus increased.

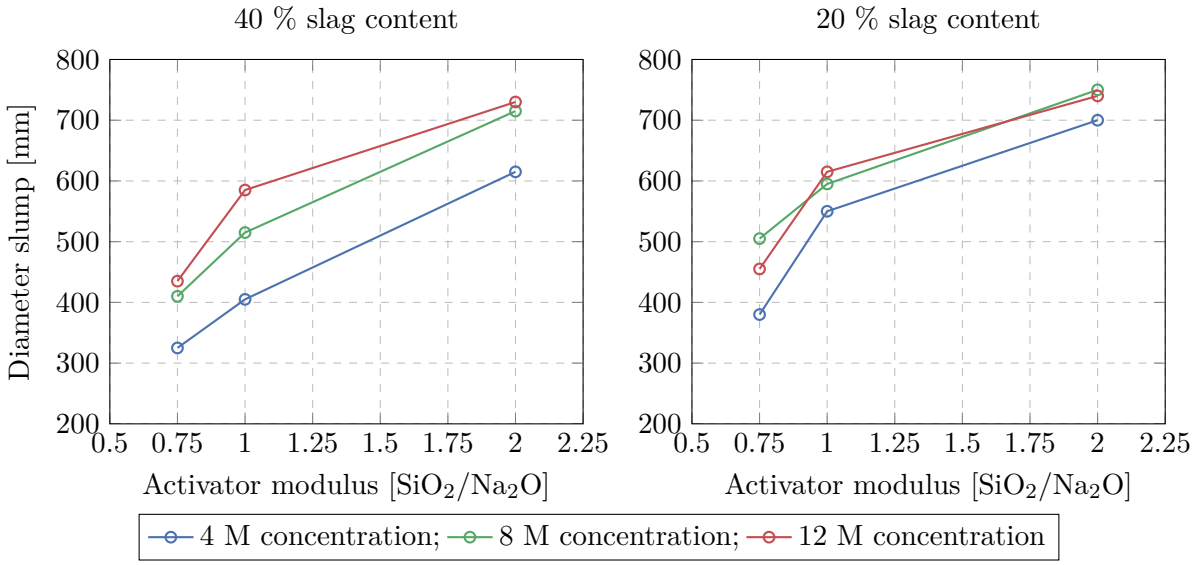

Figure 5.5: Influence of activator modulus on the workability

5.1.6 Aggregate content

The influence that the coarse aggregate content had on the workability is demonstrated in Figure 5.6. The slump flow diameter increased when the percentage coarse aggregate was increased. This could possibly be attributed to the smaller amount of sand, which caused the mix to be less sticky and flow more easily. However, segregation was observed at 70 % coarse aggregate content for the Greywacke stone. Due to the large amount of stone, the binder was not able to properly bind to the coarse aggregate.

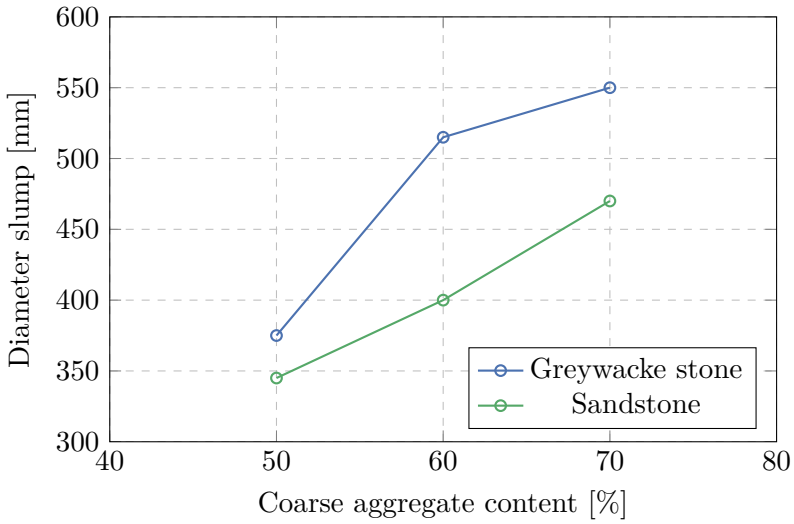

Figure 5.6: Influence of coarse aggregate content on the workability

The 13 mm stone size had a larger diameter slump flow than the 6 mm stone. This is displayed in Figure 5.7. A larger amount of small particles were present in the mix containing 6 mm stone, which caused the mix to be stiffer. The movement was also restricted due to the particles that had better interlocking.

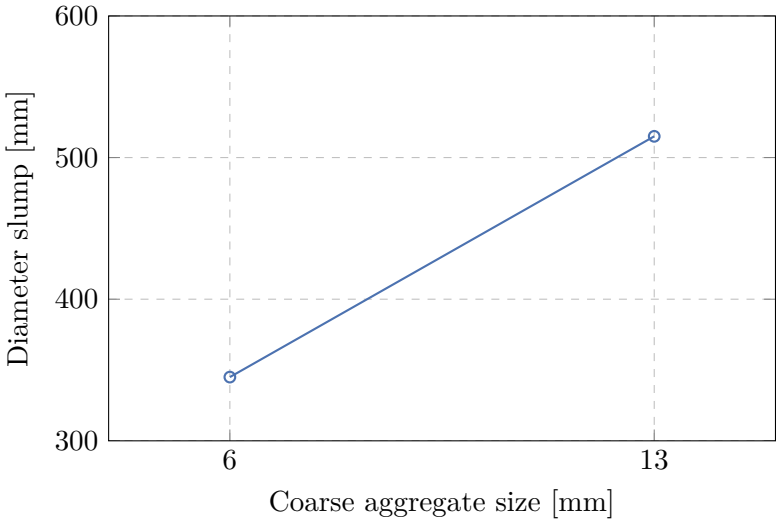

Figure 5.7: Influence of coarse aggregate size on the workability

5.1.7 Concluding summary

It can be concluded that fresh AAMs exhibited self-compacting characteristics, which is promising from a construction point of view. However, careful attention must be given to the proportions of the mix in order to ensure that the fresh AAM is not to stiff or segregates. The workability of the AAM mixes were predominantly influenced by the solution to binder ratio, as this was varied to obtain the specific values for the different parameters. A higher solution to binder ratio resulted in more flowable mixes.

5.2 Compressive strength

The results that were obtained for the compressive strength of all the mixes are given and discussed in this section. The compressive strength for the cube specimens varied between 6.4 MPa and 67.1 MPa. Several of the mixes, however, did not gain any strength.

The compressive strength for the cylinder specimens were also obtained, which varied between 5 MPa and 47.8 MPa. These results were compared with the cube strengths, which are discussed in Section 5.2.7.

5.2.1 Alkaline activator

The mixes where alternative alkaline activators were used did not gain any strength, except mix SC-100-C2N3.5M1. This is contradicting to previous research that was done on alternative activators containing sodium silicate and/or sodium carbonate. As mentioned in Section 2.4.2.4, both Wang et al., (1994) and Fernández-Jiménez et al., (2003b) found that the highest compressive strengths are obtained with mixes containing only sodium silicate. These studies also obtained comparable results between mixes containing sodium carbonate and sodium hydroxide as activators (Fernández-Jiménez et al., 2003b).

The strengths obtained in these studies could be attributed to heat curing that might have been used. However, it was unclear what curing methods were used by Fernández-Jiménez et al., (2003b). As mentioned in Section 2.2.2, OH^- ions are required to break down the aluminosilicate bonds within the binder and also acts as a catalyst during the geopolymerisation process. Thus, due to the lack of OH^- ions within the alternative activator mixes, the geopolymerisation process is not as efficient as when sodium hydroxide is used for the alkaline activator.

The compressive strength for mix SC-100-C2N3.5M1 varied between 8 MPa and 24 MPa. This indicates that the type of binder used has a significant influence on the strength of AAMs containing alternative alkaline activators. In this case, only slag was used as the binder material. Therefore, the increase in the calcium content resulted in more C-S-H reaction products, which contributes to the strength gain (Grieve, 2009). It should be noted that the strength varied significantly, which makes it difficult to predict the compressive strength.

The compressive strength of mixes SC-40(20)-C2N3.5M1 and S-40(20)-N2.9, containing OPC cement, could not be obtained. This was due to the poor workability of the mixes, as discussed in Section 5.1.1, which made it impossible to cast specimens for testing.

5.2.2 Calcium content

The influence of the calcium content on the compressive strength was determined by varying the slag content between 20 % and 40 % of the binder content. An increase in the slag content

(calcium content) resulted in higher compressive strengths, which is demonstrated by mixes SH-40-C8N5M1 and SH-20-C8N5M1 in Figure 5.8.

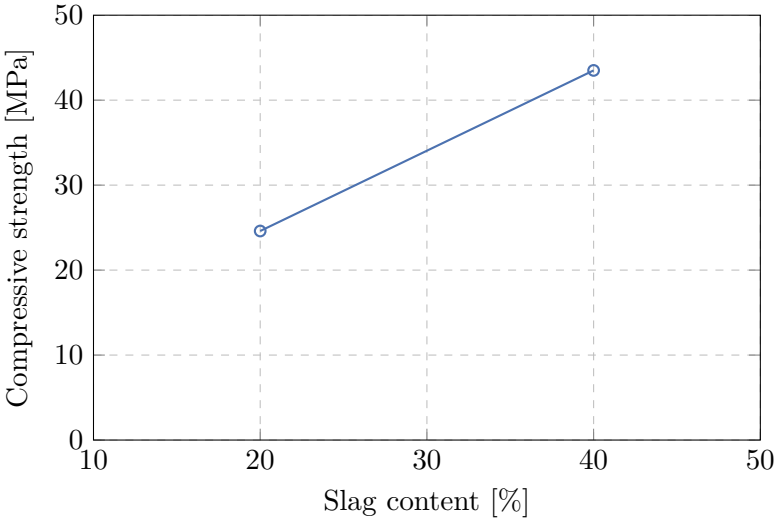

Figure 5.8: Influence of calcium content on the compressive strength

The increase in compressive strength with calcium content was also true for all of the mix variations (sodium hydroxide concentration, activator dosage and activator modulus). This is evident in Figures 5.9 to 5.11. From these figures it can be observed that the mixes with a 20 % slag content had very low strengths or no strength at all. According to Andrew Heath (19 April 2016, personal communication), heat curing is required when less than a third of the binder content consists out of slag. This could be the main reason why these strengths were so low. Another reason for the low strengths are the C-S-H reaction products that form in conjunction with the geopolymeric gel products in the presence of calcium. Due to the 20 % slag mixes containing less calcium, the formation of C-S-H reaction products are reduced and therefore the strength as well.

5.2.3 Sodium hydroxide concentration

The influence of the sodium hydroxide concentration on the compressive strength for both 20 % and 40 % slag content, are given in Figure 5.9. The different dosages are also provided on both the figures. As observed from the figure, the compressive strength increased with an increase in sodium hydroxide concentration. Therefore, these results correlates with previous research as mentioned in Section 2.4.2.5.

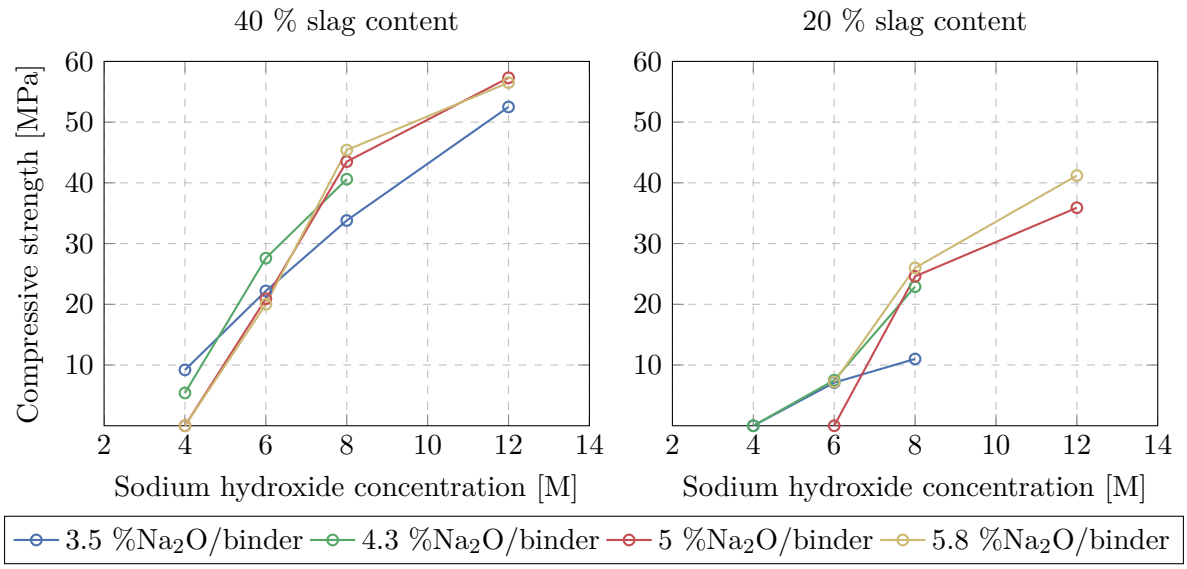

Figure 5.9: Influence of sodium hydroxide concentration on the compressive strength

For the binder consisting of 40 % slag, the compressive strength increased rapidly between 4 M and 8 M concentration, while a gradual increase is observed from 8 M to 12 M concentration. This rapid increase in concentration up until 8 M, which is followed by a gradual increase, was also observed by Barnard, (2014). However, this change in gradient, is only evident in the mixes with higher dosages. The strength increased linearly for the dosage of 3.5 %Na_2O/binder.

The gradient change at 8 M concentration was also obtained for the mixes containing 20 % slag. The compressive strength for the 5 %Na_2O/binder dosage does not follow the trend of rest of the dosages. In order for this to occur, one would expect mix SH-20-C6N5M1 to have a strength of approximately 7.3 MPa, instead of no strength. At 4 M concentration, the mixes also did not have any strength. These mixes include: SH-20-C4N3.5M1 and SH-20-C4N4.3M1.

The OH^- ions within the sodium hydroxide brakes down the aluminosilicate bonds within the binder material during the dissolution process. Thus, the higher the concentration of the sodium hydroxide, the more OH^- ions are available to dissolve the aluminosilicate. In turn an increase in strength is obtained (Fernández-Jiménez et al., 2006c).

5.2.4 Activator dosage

The relationship between the compressive strength and the activator dosage at different concentrations is represented in Figure 5.10 for both 20 % and 40 % slag content. The compressive strength for the 8 M and 12 M concentrations increased with activator dosage. For the 40 % slag content and 6 M concentration, a slight increase in strength was experienced at 4.3 %Na_2O/binder, before the strength decreased. The strength for the 20 % slag content and 6 M concentration remained relatively constant, except at 5 %Na_2O/binder. As mentioned in the previous section, this strength does not fit with the rest of results and one would expect the compressive strength to be approximately 7.3 MPa. Considering 4 M concentration, the

compressive strength decreased with dosage for the mixes containing 40 % slag content, while no strength was obtained for 20 % slag content.

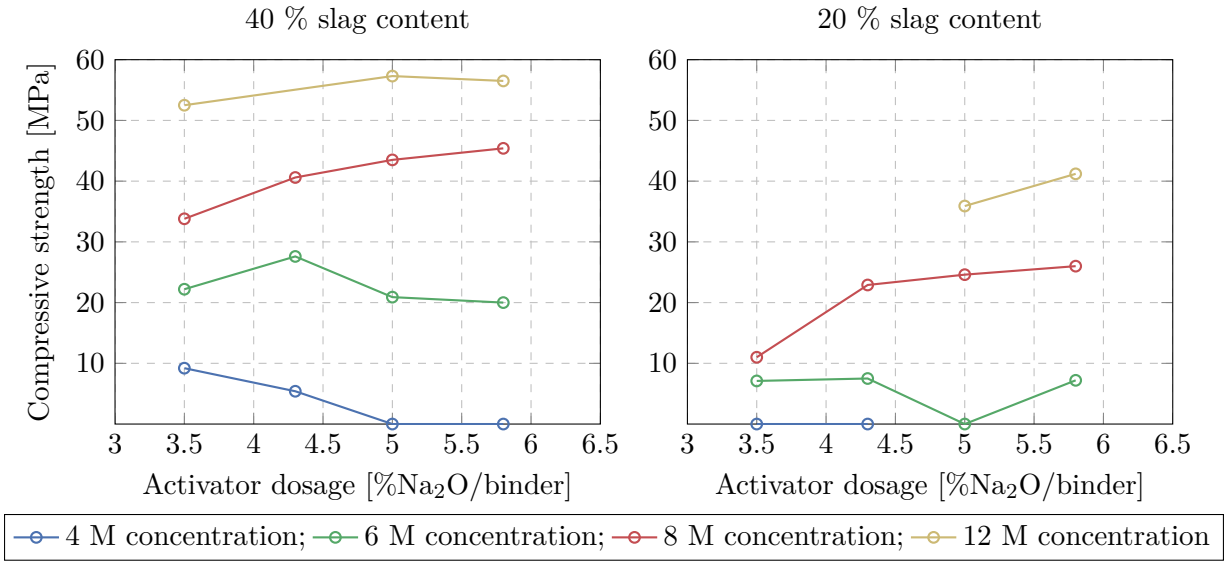

Figure 5.10: Influence of activator dosage on the compressive strength

Mix SH-40-C4N5M1 and mix SH-40-C4N5.8M1 did not gain any strength. As described in Section 5.1, the mixes were very flowable and segregation occurred, causing the specimen matrix to be inconsistent. The inconsistent matrix together with the low concentration of the mixes contributed to the lack in strength.

5.2.5 Activator modulus

Figure 5.11 demonstrates the effect that the activator modulus had on the compressive strength. The different concentrations are given for both 20 % and 40 % slag content. The compressive strength decreased with the increase of the activator modulus for both 8 M and 12 M concentration at 40 % slag content. For the 4 M concentration, the compressive strength decreased between activator modulus values 0.75 and 1, followed by an increase for the modulus of 2. As the activator modulus increased for the 20 % slag content, the compressive strength first increased before a decrease occurred. However, the mixes with 4 M concentration and 20 % slag content did not obtain any strength for activator modulus values 0.75 and 1.

As discussed in Section 2.4.2.7, the compressive strength generally increase with activator modulus until an optimum value is reached. The optimum strength is generally at an activator modulus between 0.75 and 1, which is then followed by a decrease in strength. This optimum compressive strength value at an activator modulus of 1, is clearly demonstrated by the 20 % slag content. Although one cannot observe a definite optimum modulus value for the 40 % slag, this value can most probably be assumed to be between 0.5 and 0.75. Therefore, the optimum modulus value seems to decrease as the slag content increases. However, further testing is still required to verify this statement.

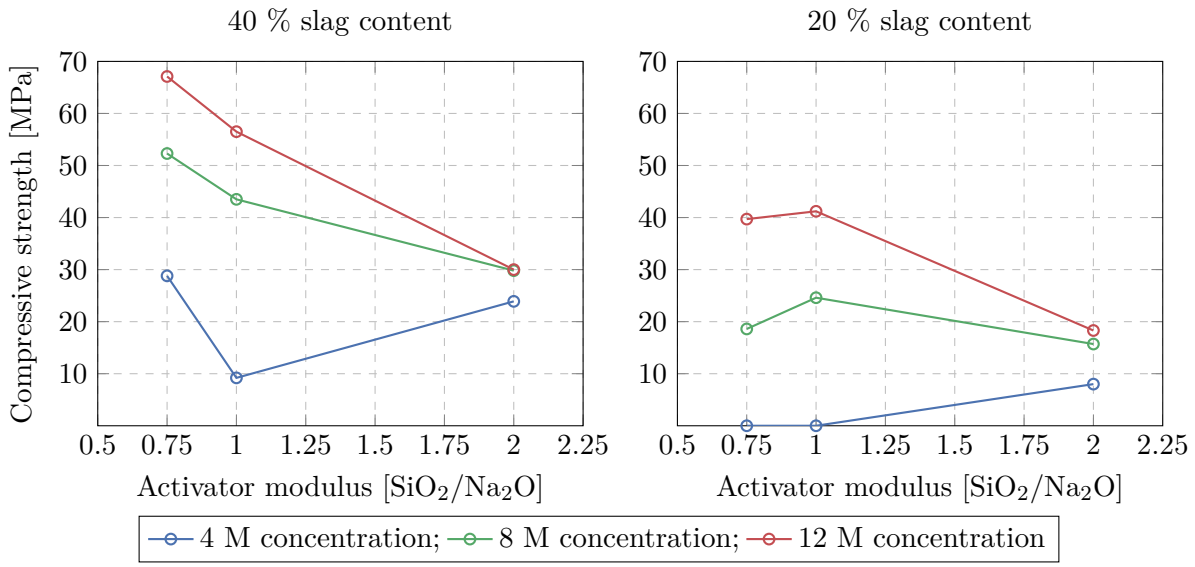

Figure 5.11: Influence of activator modulus on the compressive strength

The compressive strength that increased for the 4 M concentration after an activator modulus of 1, does not correspond with the rest of the results. However, the increase in strength could possibly be explained by the sodium silicate to sodium hydroxide ratio. Barnard, (2014) found that a sodium silicate to sodium hydroxide ratio between 1 and 2 yielded the highest compressive strengths. Due to the 4 M concentration containing less % Na_2O than the 8 M and 12 M concentrations, less sodium silicate is required to obtain a specific activator modulus. Therefore, the sodium silicate to sodium hydroxide ratios were 2, 3.76 and 5.26 at a modulus value of 2 for 4 M, 8 M and 12 M concentrations, respectively. The high ratios for the 8 M and 12 M concentrations resulted in a decrease in compressive strength, while the lower ratio for the 4 M concentration resulted in a increase in strength.

As mentioned before, mixes SH-20-C4N3.5M.75 and SH-20-C4N3.5M1 did not obtain any strength. This was mainly due to the low concentration of 4 M. The low slag content also contributes to the fact that no strength was obtained.

5.2.6 Aggregate content

The compressive strength and its relation to percentage coarse aggregate of the total aggregate content, is represented in Figure 5.12. Although the compressive strength results were similar for all of different coarse aggregate contents, a slight increase in compressive strength was obtained with a higher coarse aggregate content. This was true for both Greywacke stone and Sandstone, where the Sandstone had partially lower strengths than the Greywacke stone.

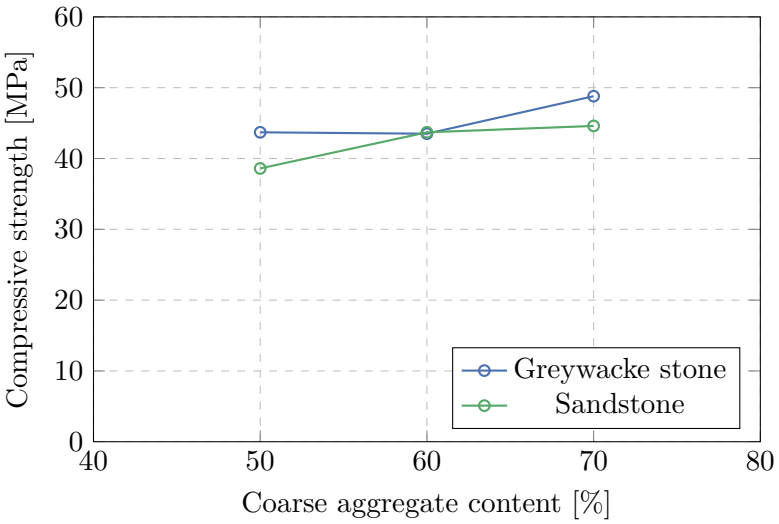

Figure 5.12: Influence of coarse aggregate content on the compressive strength

The influence of the stone size on the compressive strength is given in Figure 5.13. The compressive strength decreased from the 6 mm stone to the 13 mm stone. However, the decrease in strength is only 3 MPa, which is not significant.

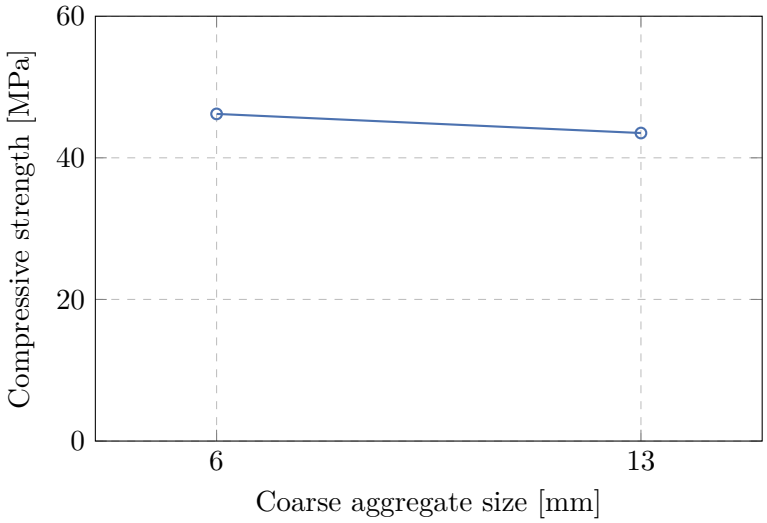

Figure 5.13: Influence of coarse aggregate size on the compressive strength

From these results, it is evident that the coarse aggregate type, content and size does not have a significant influence on the compressive strength of AAMs. The compressive strength of OPC concrete is also only influenced by the coarse aggregate when working with high strength concrete ($>$ 60 MPa)(Perrie, 2009).

5.2.7 Concluding summary

From the results presented, it is clear that the compressive strength is depended on a variety of parameters. The calcium content, sodium hydroxide concentration and the activator modulus had the largest influence on compressive strength, while the dosage did not seem to influence the compressive strength. This was also confirmed with the statistical analysis, as shown in Table 5.2. The p-values were all lower than 0.05, except for the dosage during the multiple regression (indicated in red). The low "R-squared" value for the dosage at single regression also demonstrates the small influence that the dosage had on the compressive strength. From the "β" value, it is evident that the calcium content and the sodium hydroxide concentration caused an increase in strength, while compressive strength decreased with the activator modulus. It should be noted that the water content also has a large influence on the compressive (Barnard, 2014). However, the water content remained constant for this study. Further research is still required for alternative activators, as these mixes did not obtain any strength. The aggregate content also did not have a large influence on the compressive strength.

Mix SH-40-C6N3.5M1 and mix SH-40-C6N5M1 had coefficient of variation (CV) values of 15.6 % and 10.4 %, respectively, while CV values for the rest of mixes were all lower than 10 %. A high variation was considered as a CV value larger than 10 %. The standard deviation (SD) and CV for the compressive strengths of each AAM mix, are given in Appendix A.

Table 5.2: Statistical analysis of compressive strength results

Variable	Single regression		Multiple regression (R^2=0.7302)	
	R^2	p	Beta (β)	p
Slag content	0.1708	0.0000	0.46	0.0186
Concentration	0.3797	0.0000	0.67	0.0000
Dosage	0.0977	0.0019	0.01	0.9125
Modulus	0.1401	0.0002	-0.34	0.0000

The cylinder strength is plotted against the cube strength in Figure 5.14. In the case of normal OPC concrete, the compressive strength for cylinder specimens are generally 80 % of the cube strength (EN 1992-1-1, 2004), as indicated by the line in Figure 5.14. It can be observed that the strengths for the AAMs also followed this trend. However, several of the mixes obtained sightly lower cylinder strengths than the cylinder strengths obtained by the line. Thus, the relationship between the cube and the cylinder compressive strength should be sightly adjusted for AAMs.

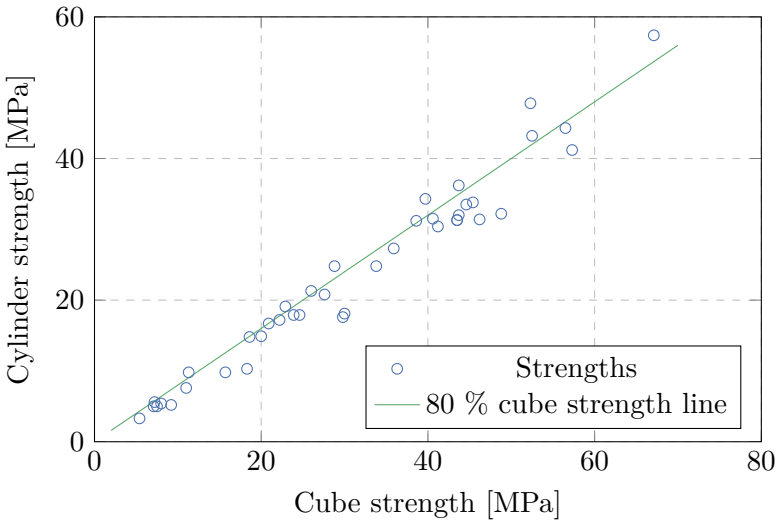

Figure 5.14: The cylinder strength compared to the cube strength

5.3 Density

The densities of all the mixes are given in this section. Density values between 2134.4 kg/m^3 and 2389 kg/m^3 were obtained, depending on the constituents within the matrix. This is lower than the typical density for OPC concrete (2400 kg/m^3). However, Barnard, (2014) also obtained similar density values.

5.3.1 Alkaline activator

The densities of the mixes with alternative activators are given in Table 5.3. The mixes with only sodium silicate as the activator had very low densities, while the sodium carbonate mixes had similar densities to the mixes with sodium hydroxide. Again, due to the workability of mixes SC-40(20)-C2N3.5M1 and S-40(20)-N2.9, the density could not be determined.

Table 5.3: Densities of alternative activator mixes

Alternative activator mixes	kg/m^3
SC-40-C2N3.5M1	2283.1
C-40-C2N3.5	2278.5
SC-100-C2N3.5M1	2285.8
SC-40(20)-C2N3.5M1	-
S-40-N2.9	2134.4
S-40-N5	2142.3
S-40(20)-N2.9	-

5.3.2 Calcium content

The influence of the calcium content on the density is represented by Figure 5.15. Similar to the compressive strength, the density increased with a higher slag content. This can also be observed in Figures 5.16 to 5.18. The slag had a higher relative density than the fly ash. Therefore, the more slag within the binder material, the higher the matrix density.

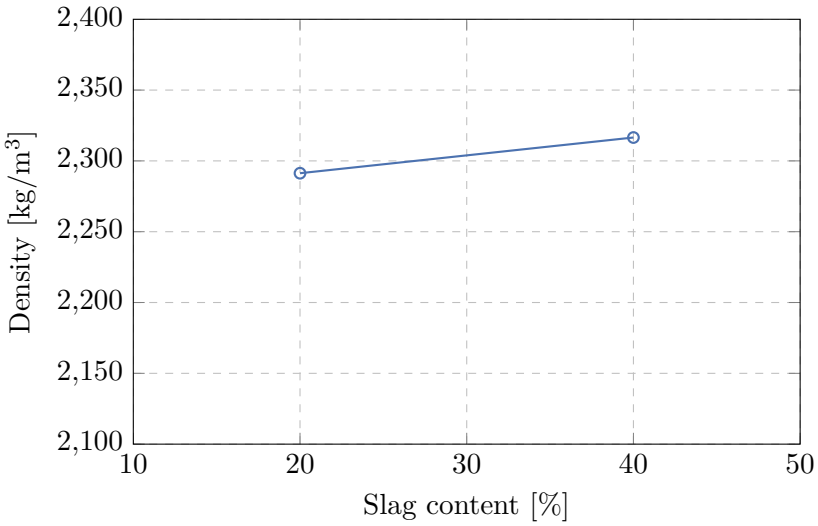

Figure 5.15: Influence of calcium content on the density

5.3.3 Sodium hydroxide concentration

Figure 5.16 demonstrates the influence of the sodium hydroxide concentration on the density of AAMs. For both 40 % slag and 20 % slag, the density increased as the concentration increased. At higher dosage, the concentration also seemed to have a larger effect on the density. The relative densities of the sodium hydroxide increased as the concentration increased (Table 4.3), resulting in a increase in the matrix density. The increase in density could also be due to more hydroxide ions available to dissolve the aluminosilicate. Therefore, a denser final matrix is able to form with more dissolved aluminosilicate.

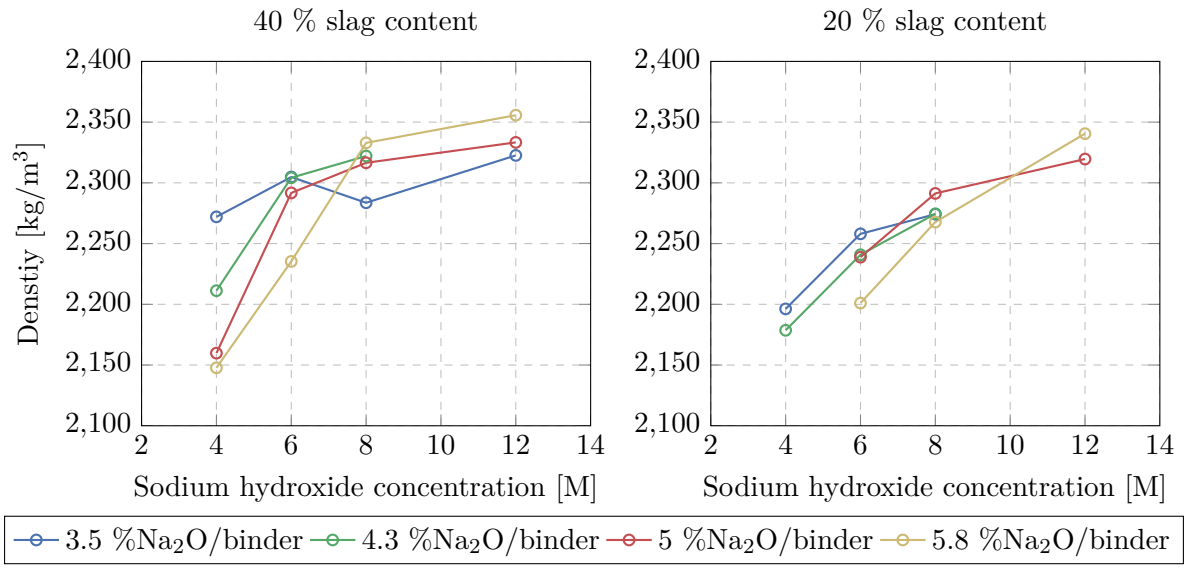

Figure 5.16: Influence of sodium hydroxide concentration on the density

5.3.4 Activator dosage

The densities in relation with the activator dosage is given in Figure 5.17. At the lower concentrations, the densities decreased with activator dosage, while the densities increased with dosage for the higher concentrations.

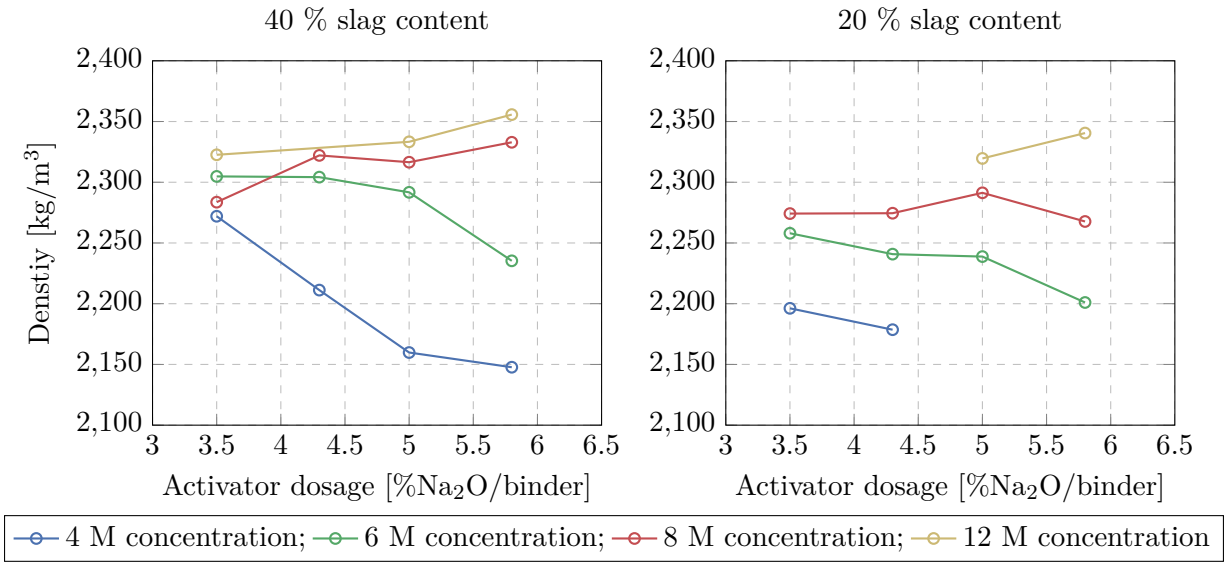

Figure 5.17: Influence of activator dosage on the density

5.3.5 Activator modulus

The influence of the activator modulus on the density, is given in Figure 5.18. For the 4 M concentration, the density remained relatively constant with an increase in modulus. For the 8 M concentration, the density decreased with an increase in activator modulus, while the 12 M

concentration experienced an increase in density at activator modulus of 1, which was followed by an decrease in density.

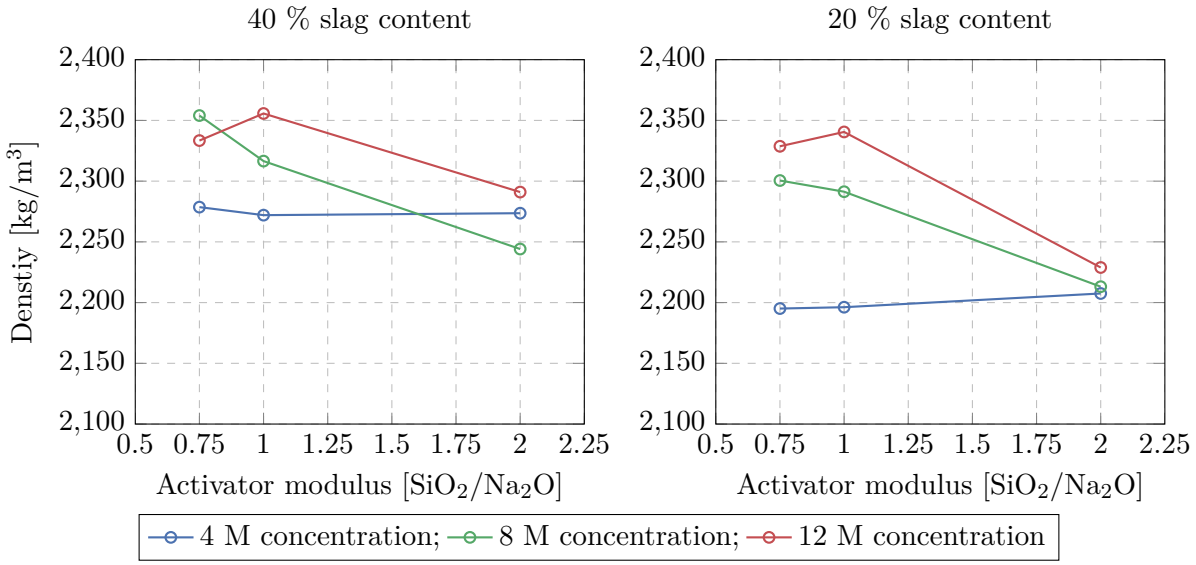

Figure 5.18: Influence of activator modulus on the density

5.3.6 Aggregate content

As shown in Figure 5.19, the density increased with an increase in the coarse aggregate content. The mixes with Greywacke stone had higher densities than the Sandstone, due to the smaller relative density of Sandstone. The coarse aggregate had a larger relative density than the fine aggregate. Therefore, the density increased with more coarse aggregate present in the matrix.

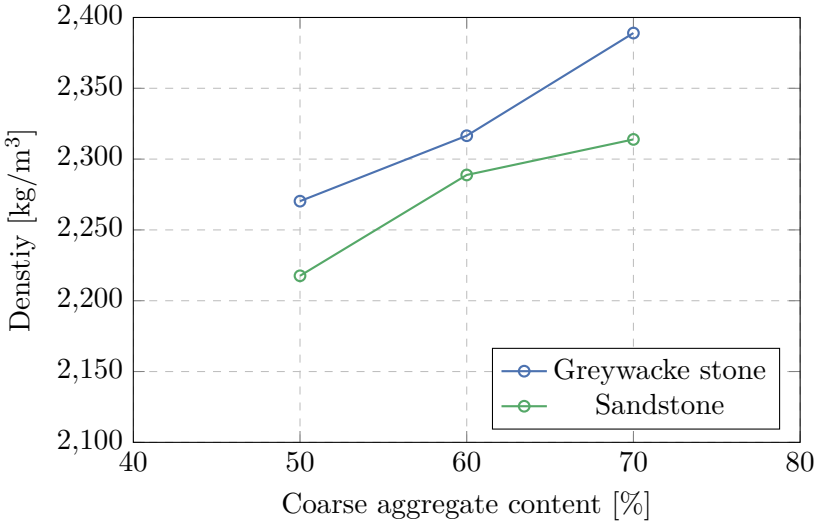

Figure 5.19: Influence of coarse aggregate content on the density

The stone size did not have an effect on the density, as displayed in Figure 5.20, with similar density's of 2315.8 kg/m^3 and 2316.5 kg/m^3 between the 6 mm and 13 mm stone, respectively.

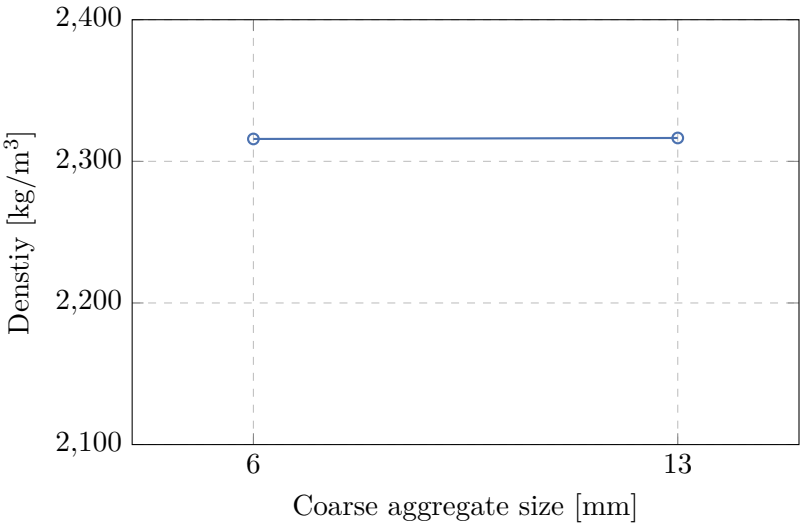

Figure 5.20: Influence of coarse aggregate size on the density

5.3.7 Concluding summary

Similar trends were found in the density results to that of the compressive strength. The calcium content and sodium hydroxide concentration caused an increase in the density, while the density decreased with activator modulus. The activator dosage had no influence on the densities. These results were verified by the statistical analysis, as shown in Table 5.4. The CV for al the mixes were lower than 2.5 (See Appendix A).

Table 5.4: Statistical analysis of density results

Variable	Single regression		Multiple regression (R^2=0.5969)	
	R^2	p	Beta (β)	p
Slag content	0.2629	0.0000	0.55	0.0000
Concentration	0.2080	0.0000	0.56	0.0000
Dosage	0.0265	0.1133	-0.08	0.3395
Modulus	0.0854	0.0039	-0.24	0.0004

5.4 Elastic modulus

The elastic modulus results that was obtained from the three cylinder specimens per tested variation, are presented in this section. The elastic modulus was determined for all of the mixes that gained strength, with values that varied between 8.2 GPa and 32.1 GPa.

5.4.1 Calcium content

The influence that the slag content (calcium content) had on the elastic modulus, is given in Figure 5.21. Mixes SH-40-C8N5M1 and SH-20-C8N5M1 were used to demonstrate the slight increase in elastic modulus caused by a higher slag content. The increase in elastic modulus corresponds with the strength that increased with slag content. However, the elastic modulus only increased by 9 %, while a 77 % strength increase was obtained for the higher slag content. The higher elastic modulus values with increased slag content can also be observed in Figures 5.22 to 5.24.

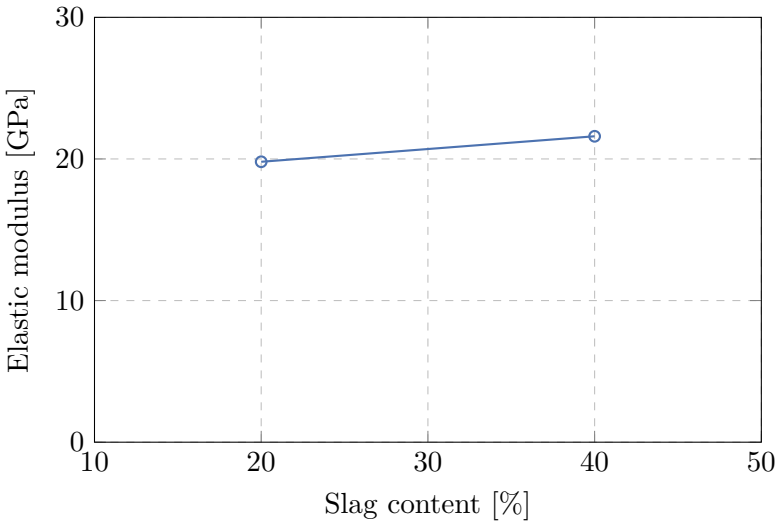

Figure 5.21: Influence of calcium content on the elastic modulus

5.4.2 Sodium hydroxide concentration

Figure 5.22 illustrates the effect that the sodium hydroxide concentration had on the elastic modulus. For both 20 % and 40 % slag content, the elastic modulus increased with concentration. Barnard, (2014) also observed an increase in the elastic modulus as the sodium hydroxide concentration increased. For the 40 % slag content, the elastic modulus increased rapidly until 6 M concentration , which was followed by a gradual increase until 12 M concentration. A rapid increase in elastic modulus also occurred for the 20 % slag content. However, the elastic modulus slightly decreased after 8 M concentration.

From these results it is evident that the bond strength between the aggregate and the binder was improved with higher sodium hydroxide concentrations. This is due to more available hydroxide ions to participate in the geopolymerisation process, ensuring that the process is more efficient. In turn, the Si, Al and Ca ions are also better interlocked together, which results in improved stiffness.

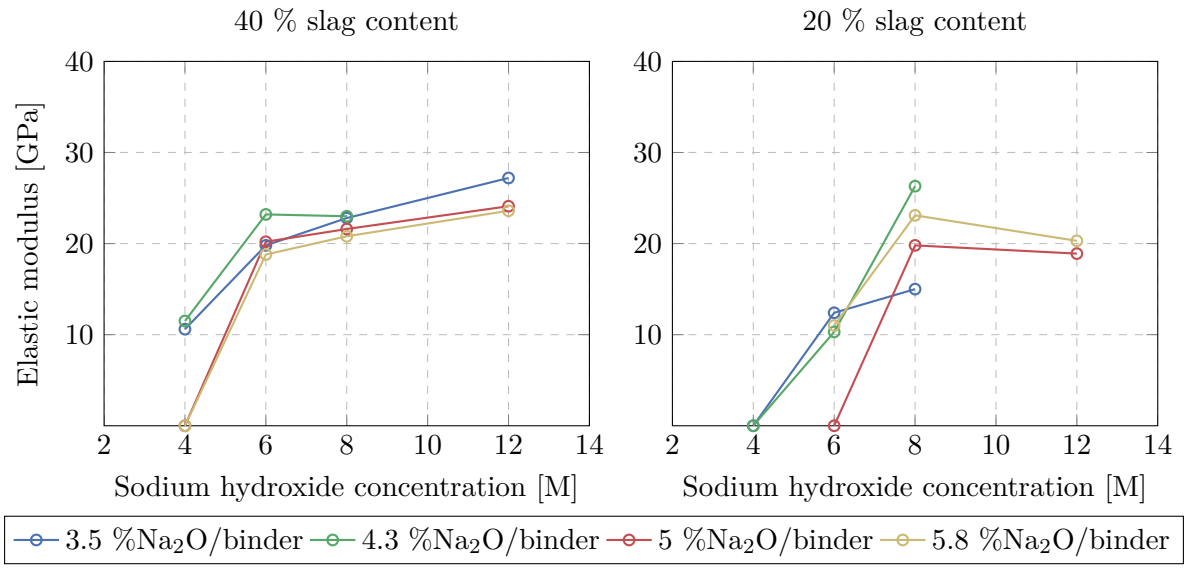

Figure 5.22: Influence of sodium hydroxide concentration on the elastic modulus

5.4.3 Activator dosage

The influence of the activator dosage on the elastic modulus is given in Figure 5.23. The elastic modulus decreased with activator dosage for the 40 % slag content. However, the decrease seem to be very small. For the 20 % slag content, the elastic modulus was very irregular, with no clear relationship with the activator dosage.

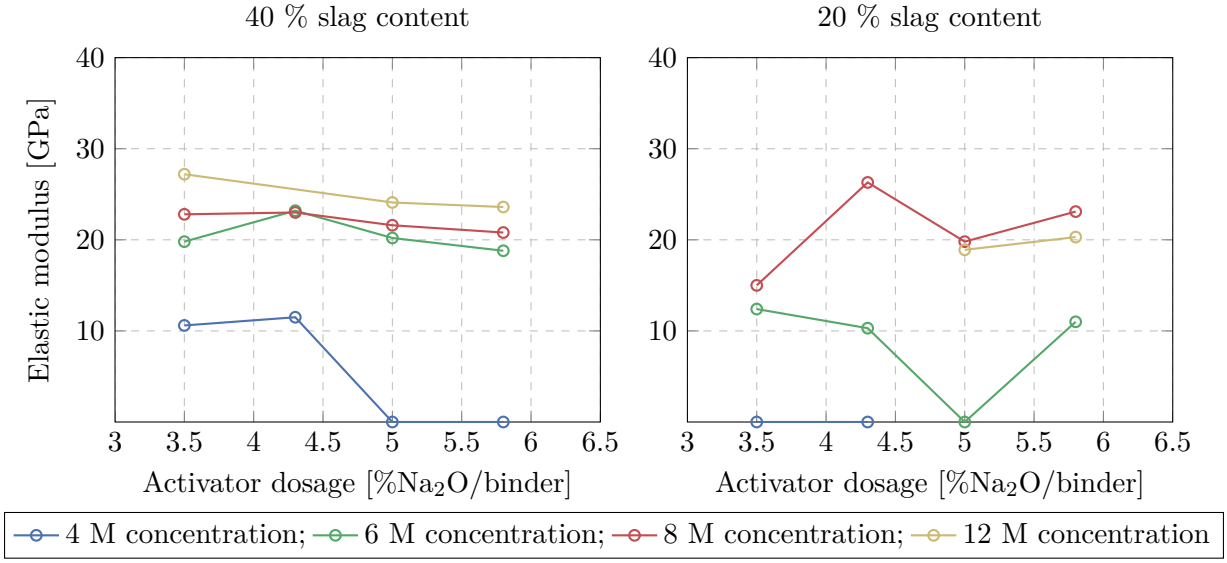

Figure 5.23: Influence of activator dosage on the elastic modulus

5.4.4 Activator modulus

The elastic modulus results for the the activator modulus is presented in Figure 5.24. For both 40 % slag and 20 % slag, the elastic modulus decreased with an increase of the activator modulus.

However, for the 4 M concentration, the modulus value of 2 caused an increase in the elastic modulus. These results are similar to strength results for the activator modulus. The strength also decreased with activator modulus, except for the 4 M concentration, which increased at a modulus value of 2. Therefore, the trends of elastic modulus results are similar to the strength results.

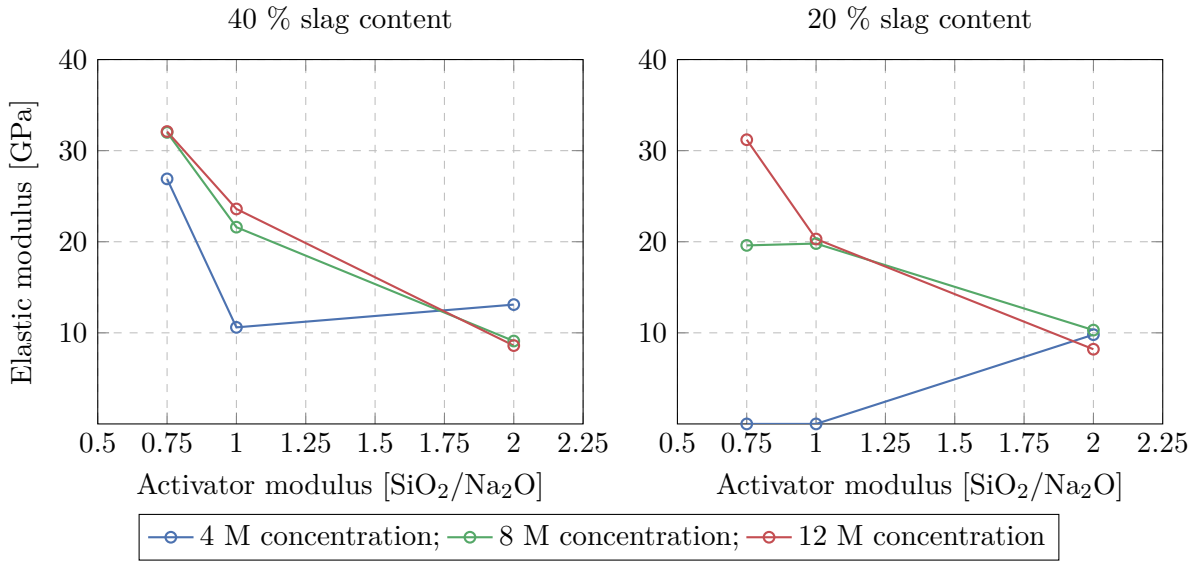

Figure 5.24: Influence of activator modulus on the elastic modulus

5.4.5 Aggregate content

The influence of the coarse aggregate content on the elastic modulus is given in Figure 5.25. The optimum coarse aggregate content is 60 % of the total aggregate. However, the variation between the elastic modulus values for the different coarse aggregate contents were small. This was true for both the Greywacke stone and Sandstone, with higher values obtained for the Greywacke stone. This corresponds to the EN 1992-1-1, (2004) which states that the elastic modulus is approximately 30 % less when sandstone is used.

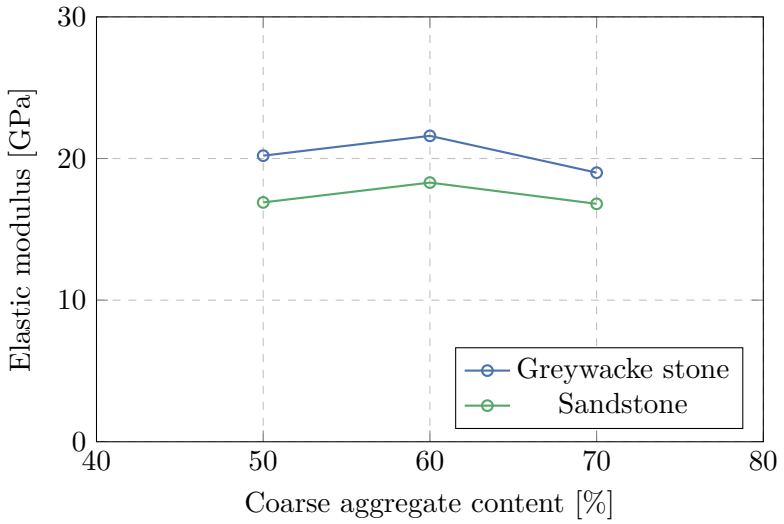

Figure 5.25: Influence of coarse aggregate content on the elastic modulus

As shown in Figure 5.26, the elastic modulus decreased with a larger stone size. This also correspond with the decrease in strength that was obtained for an increase in stone size. The smaller aggregate allows for more contact between the paste and the stone, as well as better interlocking of particles. Therefore, the stiffness is improved with a smaller stone size (Alexander et al., 2009).

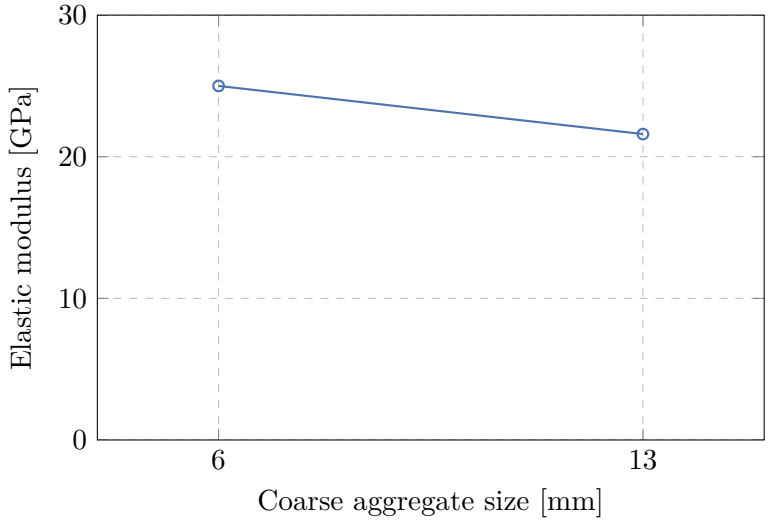

Figure 5.26: Influence of coarse aggregate size on the elastic modulus

5.4.6 Concluding summary

The elastic modulus is low for the AAMs in comparison with normal OPC concrete, ranging between 8.2 GPa and 32.1 GPa. From Table 3.1, it can be observed that the elastic modulus for normal OPC concrete is generally higher than 29 GPa. From a structural point of view, these low elastic modulus values for AAMs are insufficient, because they will cause large deflections. However, with the optimum mix parameters higher elastic modulus values can be obtained.

The parameters which had the largest influence include the calcium content, sodium hydroxide concentration and the activator modulus. Promising elastic modulus values were obtained at high calcium content, high sodium hydroxide concentration, as well as low activator modulus. The elastic modulus was very irregular with activator dosage. These trends were also observed in the statistical analysis, as shown in Table 5.5. It should be noted that the following mixes had large CV values: SH-40-C4N3.5M1, SH-40-C4N4.3M1, SH-40-C4N3.5M0.75, SH-40-C6N5M1, SH-20-C6N4.3M1, SH-20-C8N3.5M1, SH-20-C8N4.3M1, SH-20-C8N5.8M1.

Table 5.5: Statistical analysis of elastic modulus results

Variable	Single regression		Multiple regression (R^2=0.6382)	
	R^2	p	Beta (β)	p
Slag content	0.0652	0.0121	0.24	0.0004
Concentration	0.1104	0.0010	0.39	0.0000
Dosage	0.0157	0.2241	-0.05	0.5347
Modulus	0.4692	0.0000	-0.66	0.0000

5.5 Stress-strain relationship in compression

The stress-strain results that were obtained for the three cylinder specimens of the reference mix (SH-40-C8N5M1), are given in Figure 5.27. All three of the specimens gave similar stress-strain curves. However, the strain values at the ultimate stress varied for the different specimens.

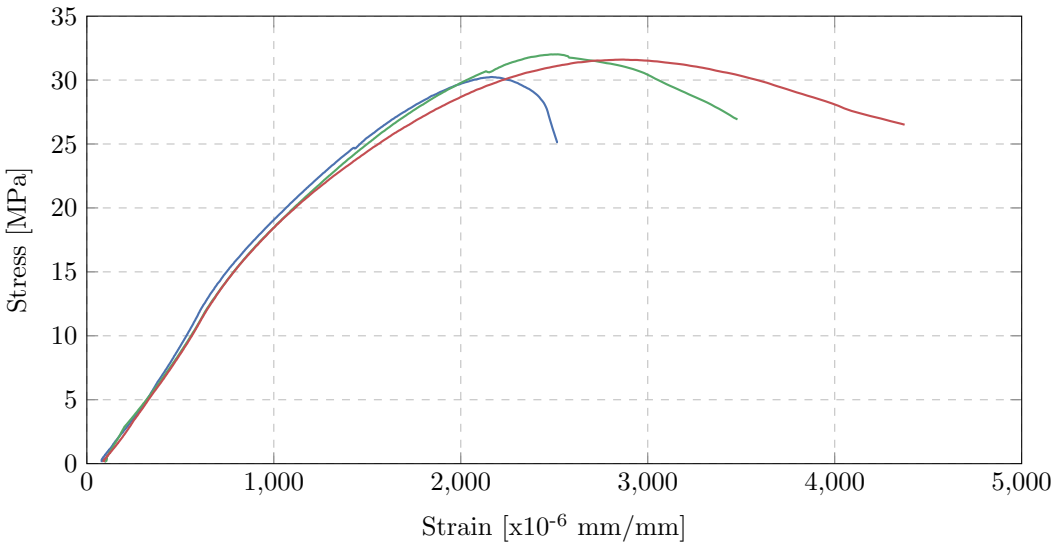

Figure 5.27: The stress-strain results for the reference mix (SH-40-C8N5M1)

The stress percentages for the reference mix were 70.5 %, 64.4 % and 65.3 %, respectively. This resulted in an average of 66.7 %, a standard deviation of 3.3 % and a CV of 4.95 %. Therefore, the specimens deviated from the linear-elastic behaviour after approximately 66 %

of the ultimate stress was reached. The rest of the mixes obtained average stress percentages between 58 % and 84 %. However, a definite relationship between the different variables and the stress percentage could not be observed. This was confirmed with the large p-values from the statistical analysis, as given in Table 5.6.

Table 5.6: Statistical analysis of stress percentage results

Variable	Single regression		Multiple regression (R^2=0.055)	
	R^2	p	Beta (β)	p
Slag content	0.0045	0.5171	0.04	0.6925
Concentration	0.0002	0.8815	0.09	0.4796
Dosage	0.0186	0.1850	-0.18	0.1535
Modulus	0.0308	0.0873	-0.17	0.1025

The strain percentages obtained for the reference mix were 53.5 %, 45.8 % and 40 %, respectively. The average strain percentage was 46.6 %, with a standard deviation of 6.56 % and a CV of 14.1 %. The large variance between the specimens were due to the different strain values that was obtained at ultimate stress. Average strain percentages between 22 % and 75 % were obtained for the other mixes.

It can be observed from the p-value in the statistical analysis (Table 5.7) that the activator modulus did not have an influence on the strain percentage for the single regression, while for the multiple regression the dosage did not have an influence. The sodium hydroxide concentration had the largest influence on the strain percentage, with a "R-squared" value of 0.296 and a "β" value of 0.62. It should be noted that most of the mixes had large CV values (between 2 % and 27 %). Therefore, even though the statistical analysis consider the variation between the different specimens of a mix, the relationships between the variables and the strain percentage, obtained from the statistical analysis, should be questioned.

Table 5.7: Statistical analysis of strain percentage results

Variable	Single regression		Multiple regression (R^2=0.5149)	
	R^2	p	Beta (β)	p
Slag content	0.1406	0.0002	0.43	0.0000
Concentration	0.2955	0.0000	0.62	0.0000
Dosage	0.0583	0.0178	-0.05	0.6080
Modulus	0.0353	0.0667	-0.15	0.0428

The stress- and strain percentages for all the other mixes are given in Appendix A.

5.6 Problems incurred

There were several problems that occurred during the mixing, casting and curing of the AAM specimens. These problems include: rapid setting; consistency of mixes; green discolouration of specimens; leaching of sodium bicarbonate; and small surface cracks. These problems are discussed in this section.

Some of the mixes hardened very rapidly, making it difficult to adequately cast the fresh AAMs within the moulds. This rapid setting also made it difficult to clean the mixer and mixing equipment. Therefore, the casting- and cleaning process had to be done relatively quickly to ensure that consistent specimens were obtained and that the AAMs did not harden in the mixer or onto the mixing equipment. The slag content and sodium hydroxide concentration had a significant influence on the setting times. Less C-S-H reaction products are formed with a lower slag content, which resulted in a longer final setting time. The setting time was also accelerated by a higher sodium hydroxide concentration, due to more OH^- ions being available to improve the efficiency of the geopolymerisation process.

As mentioned in Section 5.1, the solution to binder ratio had a large influence on the consistency of the mixes. Very flowable mixes with segregation were obtained when the solution to binder ratio was high, while low solution to binder ratios resulted in mixes that were to stiff to place in the moulds. Thus, it is recommended that a solution to binder ratio of between 0.4 and 0.62 is used.

After the cubes were demoulded, a green colour was visible on the surface of some of the AAM mixes, as shown in Figure 5.28a. This colour was mainly attributed to the slag content within the binder, as the mixes with 20 % slag had no or little discolouring. The discolouring of the 20 % slag and 40 % slag is compared in Figure 5.28b. The green colour disappeared after a few days of curing, but remained in the inside of the specimens.

(a) 40 % slag (b) 20 % slag

Figure 5.28: Green discolouring of AAMs with

A white crystal like efflorescence formed on the surface of some of the specimens. This is demonstrated in Figure 5.29. The efflorescence is sodium bicarbonate that is leached from the specimens due to an excess amount of sodium hydroxide in the matrix that has not reacted with the binder. Sodium hydroxide reacts with CO_2 in the atmosphere after it migrates to the drying surface (Davidovits, 2011). The leaching can be prevented with the proper curing conditions, where the specimens are placed in plastic bags in order to avoid contact with CO_2 (Andrew Heath, 19 April 2016, personal communication).

Figure 5.29: Efflorescence on surface of specimens

Surface cracks were also observed on a few of the specimens. These cracks were very fine, as shown in Figure 5.30. Even though the cracks were small, they still raise concern in terms of durability. From previous research (Barnard, 2014), it was found that the slag content and the water content were the main contributing factors to these cracks. The amount and size of the cracks increases with a higher slag content. Slag starts to hydrate when it is activated with an alkaline solution. Before the polycondensation process occurs, the hydrate goes through dehydroxylation (loss of water). Uneven volume change is caused by the loss of water, resulting in cracks. Less cracks are formed when more water is added to the matrix (Barnard, 2014).

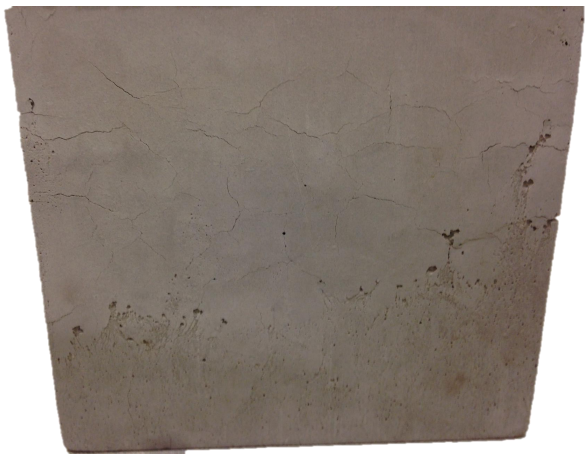

Figure 5.30: Surface cracks on specimens

The rapid setting and consistency of the mixes will cause difficulties during the mixing and casting of AAMs. The leaching of sodium bicarbonate and the small service cracks are unappealing and also raise concern with regards to the durability of AAMs. In order to avoid these problems, attention has to be given to the constituents used during the design of AAMs and the correct curing procedures has to be used.

Chapter 6

Results and discussion: Structural behaviour

The structural behaviour of reinforced AAMs were investigated in terms of bending behaviour and bond between the reinforcement and the AAMs. As stated in Chapter 4, a four point bending test was performed on reinforced AAM beams to determine the bending behaviour, while the bond was tested with pull-out tests. For both tests, two AAM mixes were tested and compared to two OPC mixes with similar compressive strengths. The results that was obtained for these tests are presented and discussed in this chapter.

6.1 Reinforced beam tests

The reinforced beam (RB) specimens were prepared and tested according to the specifications set out in Section 4.2.6. The beams deflected as the load increased, causing flexural cracks to form along the span. The beams were tested until failure occurred. The moment-deflection curve (at mid-span) was plotted to obtain the flexural capacity, mid-span deflections at serviceability load, as well as the ductility and energy dissipated for each beam. The crack formations were also recorded at different load increments. These results are represented in this section.

6.1.1 General behaviour of reinforced beams

The typical flexural behaviour of reinforced beams are demonstrated by the load-deflection curve at mid-span, in Figure 6.1. Distinct events, which takes place during a RB test, can be identified from this curve. These events include: the cracking of the concrete (A); tensile reinforcement that yields (B); the concrete crushing at the compression face (C); the load slightly dropping after the ultimate load is reached (C'); and the concrete in the compression zone disintegrating due to the yielding of the compression reinforcement (D) (Robberts et al., 2010; Sumajouw et al., 2006).

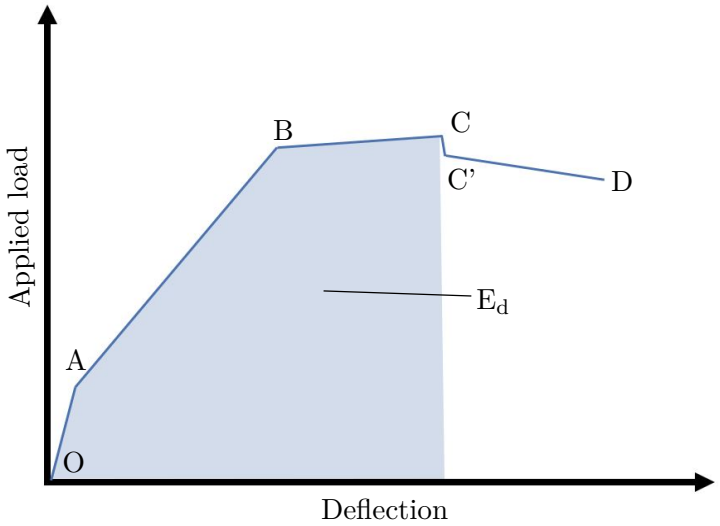

Figure 6.1: Idealised load-deflection curve at mid-span

The RB specimens in this study were designed to be under-reinforced ($x < 0.6414d$); therefore the tensile reinforcement yielded before the beams failed. This resulted in similar flexural behaviour for all the beams. However, it should be noted that the distinct events as demonstrated in Figure 6.1, were not all clearly visible for the different beam specimens. The beams were also only tested until a slight drop in the recorded load occurred (C'). This was done to avoid the complete destruction of the beams, as the beams still needed to be lifted out of the test setup.

6.1.2 Moment-deflection curve

The moment-deflection curves for all the RB specimens are given in Figure 6.2. The moment and deflection was taken at the mid-span of the beams. The results of the two RB specimens tested for each mix showed repeatability, as similar moment-deflection curves were obtained.

The moment-deflection curves for AAM-mix1 were lower than the OPC-mix1 curves, resulting in higher deflections for AAM-mix1. This is due to the low elastic modulus of AAM-mix1, resulting in a decrease in stiffness. AAM-mix2 compared relatively well with OPC-mix2, with the curve only being slightly lower. The elastic modulus for AAM-mix2 was higher than that of AAM-mix1. Therefore, improved flexural behaviour was obtained for AAM-mix2, which was almost similar to that of OPC-mix2.

From Figure 6.2, it can be observed that cracking of the concrete (A) started to occur at a moment of approximately 6 kN.m for the OPC-mixes, while for the AAM-mixes the cracks initiated at the start of loading. This could be due to the shrinkage cracks that formed during the curing of the AAM-mixes. For all the mixes, a clear point for when the reinforcement yields (B) is not evident on the moment-deflection curves. The crushing of the concrete at the compression face (C) and the drop in load after ultimate load (C') occurred at different stages for the different mixes. The flexural capacity (ultimate load) for the mixes are given and discussed in the following section.

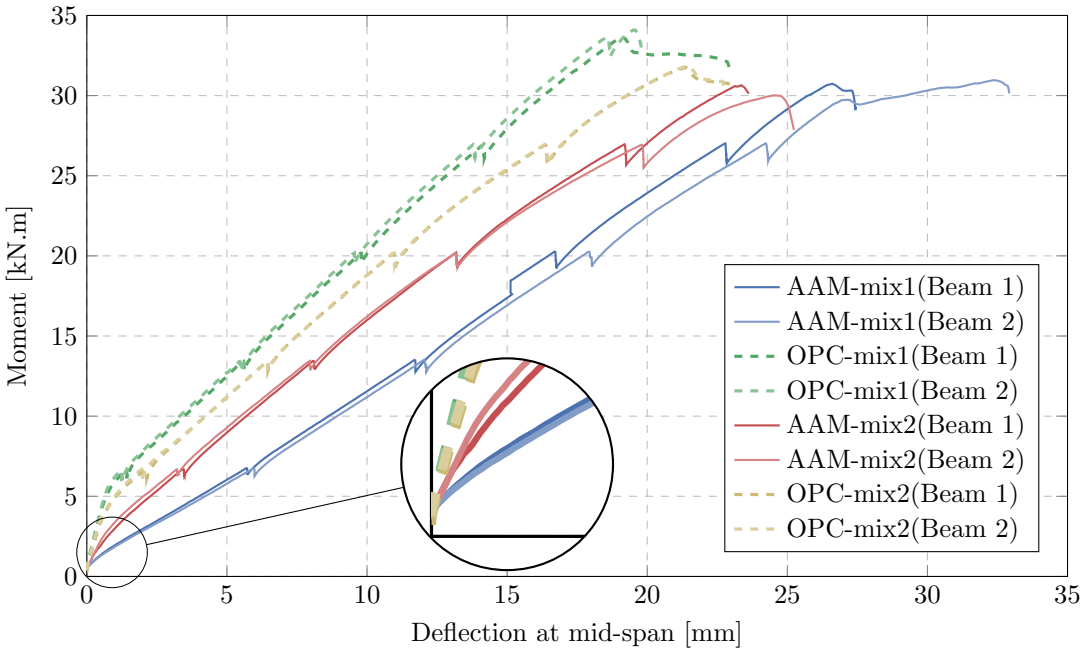

Figure 6.2: Moment-deflection curves for RB specimens

6.1.2.1 Flexural capacity

The cylinder strength ($f_{c,cyl}$), elastic modulus (E_s) and ultimate moment (M_u) for all the RB specimens are given in Table 6.1. It can be observed that AAM-mix1 had a cylinder strength of approximately 26 MPa, which was lower than the strength obtained for the reference mix (SH-40-C8N5M1). It should be noted that the two mixes are identical. This resulted in different strengths between AAM-mix1 and OPC-mix1, as the same cylinder strength as the reference mix (35 MPa) wanted to be achieved. The elastic modulus for AAM-mix1 was also lower than that of mix SH-40-C8N5M1. Although different mechanical properties were obtained for AAM-mix1 and OPC-mix1, a comparison was still made between the two mixes. The mechanical properties for AAM-mix2 were quite similar to mix SH-20-C8N5M1, with only the elastic modulus being higher for AAM-mix2. Therefore, a good comparison could be made between AAM-mix2 and OPC-mix2, as the strengths were close to the desired cylinder strength of roughly 20 MPa (Same cylinder strength as mix SH-20-C8N5M1). The strengths and elastic modulus for mixes SH-40-C8N5M1 and SH-20-C8N5M1 can be found in Appendix A. It should be noted that the elastic modulus for the OPC-mixes were relatively high compared to the typical elastic modulus values, as given in Section 3.2.1.

Both the AAM-mixes had lower ultimate moments than the OPC-mixes; with only a small difference between the second mixes. This was due to the smaller strengths of the AAM-mixes. Although AAM-mix1 had a higher strength than AAM-mix2 and OPC-mix2, the ultimate moments were lower than that of OPC-mix2.

The ultimate moment for each RB specimen was also calculated according the method described in Section 3.3. However, the safety factors were omitted and the actual cylinder strength instead

of the characteristic strength was used to determine the actual ultimate moment. It can be observed from Table 6.1, that the experimental moments compared well with the calculated moments, with only a slight difference between the two. This indicates that the design of structural elements with AAMs can be done according the design codes, such as EN 1992-1-1, (2004).

Table 6.1: Flexural capacity of RB specimens

Specimen	$f_{c,cyl}$ [MPa]	E_c [GPa]	Ultimate moment (M_u)[kN.m]		
			Experimental	Calculated	% error
AAM-mix1 (Beam 1)	27.0	12.2	30.7	33.1	7.8
AAM-mix1 (Beam 2)	25.9	12.3	31.0	32.9	6.1
OPC-mix1 (Beam 1)	35.6	44.6	33.7	34.7	3.0
OPC-mix1 (Beam 2)	36.8	46.1	34.1	34.9	2.4
AAM-mix2 (Beam 1)	21.2	25.3	30.7	31.8	3.6
AAM-mix2 (Beam 2)	20.7	25.2	30.0	31.6	5.3
OPC-mix2 (Beam 1)	23.3	33.1	31.2	32.3	3.5
OPC-mix2 (Beam 2)	23.5	36.8	31.9	32.4	1.6

6.1.2.2 Deflection

The deflections at the service load (P_s) were determined from the test data plotted in Figure 6.2. These loads refer to the load exerted by the actuator. For the purpose of this study, the service load was taken as 67 % of the ultimate load, similar to Sumajouw et al., (2006). The deflections at service load, were also calculated with Equation 3.11 in Section 3.5. For ζ, β was taken as 1 and M_{cr}/M was used instead of σ_{sr}/σ_s. M_{cr} was calculated with the tensile strength of concrete (f_{ctm}), specified according to the EN 1992-1-1, (2004). The self-weight of the beams were neglected in these calculations. The deflections are summarised in Table 6.2.

Table 6.2: Mid-span deflection of RB specimens

Specimen	P_s [kN]	Deflection (Δ_s) [mm]		
		Experimental	Calculated	% error
AAM-mix1 (Beam 1)	45.5	17.38	14.46	16.8
AAM-mix1 (Beam 2)	45.9	18.69	14.57	22.0
OPC-mix1 (Beam 1)	49.9	11.20	10.81	3.5
OPC-mix1 (Beam 2)	50.5	11.08	10.85	2.1
AAM-mix2 (Beam 1)	45.4	13.73	11.43	16.8
AAM-mix2 (Beam 2)	44.5	13.57	11.28	16.9
OPC-mix2 (Beam 1)	47.1	11.83	11.08	6.3
OPC-mix2 (Beam 2)	47.2	11.83	10.81	8.6

The largest deflections were obtained for AAM-mix1. This was due to the small elastic modulus of 12.2 GPa, as given in Table 6.1. These large deflections for AAM-mix1 also occurred at lower strengths compared to OPC-mix1. The deflections for AAM-mix2 and OPC-mix2 were almost the same, with AAM-mix2 deflecting a little more than OPC-mix2. Due to the higher elastic modulus of AAM-mix2, smaller deflections were obtained for AAM-mix2 compared to AAM-mix1. It is interesting to note that the OPC-mixes had relatively similar deflections. However, the loads at which these deflections occurred, are different.

The calculated deflections for the OPC-mixes were very similar to the experimental deflections, while the experimental deflections for AAMs were larger than the calculated values. The AAM-mixes already cracked at the initial load, which will cause larger deflections. As mentioned before, the low cracking moment of AAM-mixes can be attributed to the shrinkage cracks that occurred during curing. Therefore, the cracking moment (M_{cr}) should be adjusted for the calculation of the deflections. However, the calculated deflections increases only slightly when the cracking moment of the AAM-mixes is taken as zero, with a deflection of approximately 14.8 mm for AAM-mix1 and 11.7 mm for AAM-mix2. Thus, it seems that the EN 1992-1-1, (2004) is conservative in terms of the deflection calculations for AAMs and requires further investigation.

From these results, it is evident that the deflection of structural elements will be a major concern when using AAMs. The large deflections are caused by the low stiffness of AAMs. Thus, the elastic modulus for AAMs has to be improved to obtain smaller deflections. This was demonstrated by AAM-mix2, which had smaller deflections due to a higher elastic modulus.

6.1.2.3 Ductility and energy dissipated

The ductility and the dissipated energy for the RB specimens were also determined. The ductility, given as the ductility index (μ_d), was taken as the ratio of deflection at the ultimate load (Δ_u) to the deflection at the yield load (Δ_y). As there was no clear indication of the yield points, Δ_y was taken as the displacement at the service load. This was also done in the study by Sumajouw et al., (2006). The dissipated energy (E_d) was determined from the moment-displacement curves by calculating the area under the curve up until the ultimate moment, as demonstrated in Figure 6.1. Table 6.3 gives the ductility index and energy dissipated for each RB specimen.

The ductility index for all the RB specimens were quite low compared to the results found by Sumajouw et al., (2006) (obtained values between 1.7 and 4.95). The unclear yield point on the moment-deflection curves, indicate that the reinforcement yields close to ultimate moment where concrete crushing occurs. This resulted in a low ductility as indicated by the ductility index values in Table 6.3. All of the RB specimens had relatively the same ductility.

The energy dissipated for AAM-mix1 was higher than that of OPC-mix1. The high energy dissipation of AAM-mix1 was due to the large deflections, while the ultimate moment was relatively the same as the other mixes. Again, a good comparison between AAM-mix2 and OPC-mix2 was obtained, with both having the same amount of energy dissipated.

Table 6.3: Ductility and dissipated energy of RB specimens

Specimen	Ductility index $\mu_d = \Delta_u/\Delta_y$	Energy dissipated E_d [kN.m^2]
AAM-mix1 (Beam 1)	1.53	0.450
AAM-mix1 (Beam 2)	1.73	0.572
OPC-mix1 (Beam 1)	1.71	0.372
OPC-mix1 (Beam 2)	1.76	0.392
AAM-mix2 (Beam 1)	1.70	0.407
AAM-mix2 (Beam 2)	1.81	0.410
OPC-mix2 (Beam 1)	1.81	0.404
OPC-mix2 (Beam 2)	1.81	0.406

6.1.3 Crack formation

The crack patterns that was obtained for the RB specimens, are given in Figures 6.3 to 6.6. The typical flexural crack formation for beams were obtained, with cracks that initiated within the pure bending zone and more cracks forming along the span of the beam as the load increased, while the existing cracks propagated. Inclined cracks were obtained in the shear zone, due to the shear force.

The measured crack widths and crack spacings for all the RB specimens, are given in Appendix C. These results were used to obtain the crack distribution and average crack widths, which are given in the following section in terms of applied load and the mid-span deflection. For each mix, the crack distribution and average crack widths were taken as the average between the two tested beams.

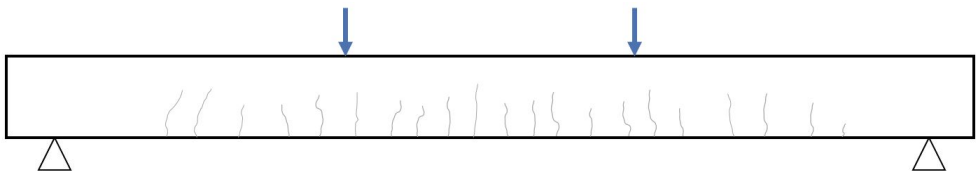

(a) Beam 1

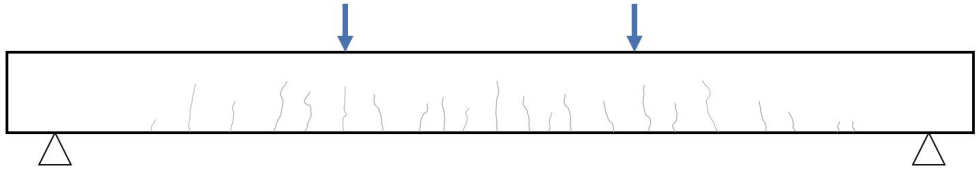

(b) Beam 2

Figure 6.3: Crack patterns for AAM-mix1 RB specimens

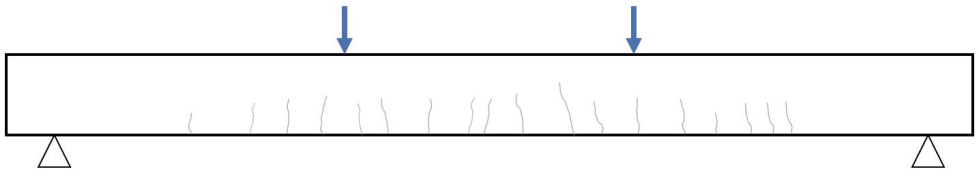

(a) Beam 1

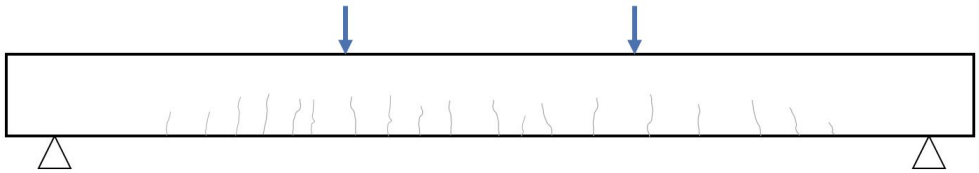

(b) Beam 2

Figure 6.4: Crack patterns for OPC-mix1 RB specimens

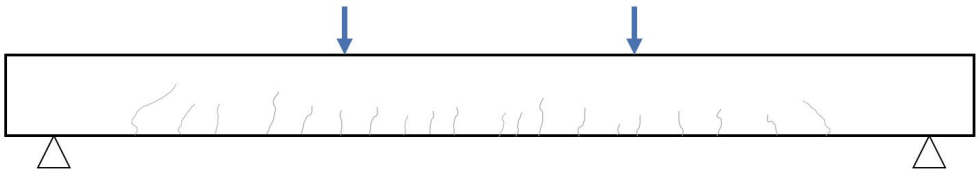

(a) Beam 1

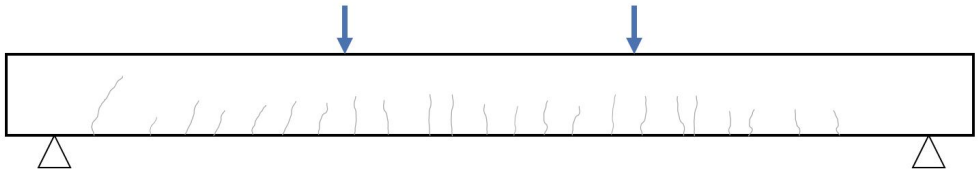

(b) Beam 2

Figure 6.5: Crack patterns for AAM-mix2 RB specimens

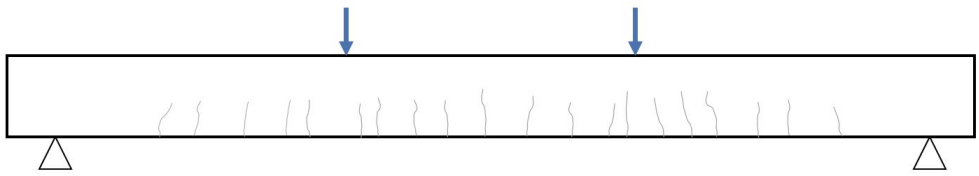

(a) Beam 1

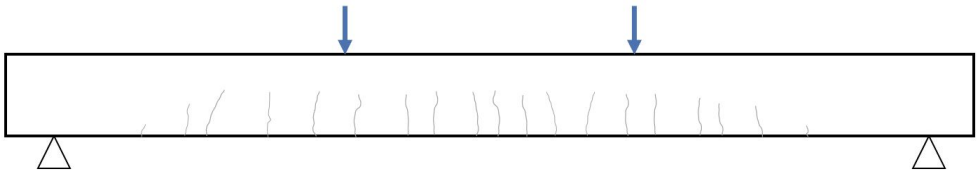

(b) Beam 2

Figure 6.6: Crack patterns for OPC-mix2 RB specimens

6.1.3.1 Crack distribution

The crack distribution is considered as the number of cracks per meter length; with the meter length extending between the two concentrated loads. In Figure 6.7, the crack distribution is given in terms of the paused load increments. As the load increased, the number of cracks also increased. For the AAM-mixes, most of the cracks already formed at 15 kN, with a steady increase in the number of cracks up until 45 kN. The large amount of cracks at 15 kN could possibly be attributed to the initial shrinkage cracks that occurred during curing. The OPC mixes only had a small number of cracks at 15 kN, which increased rapidly at 30 kN and was stable after 45 kN. OPC-mix1 had less cracks than AAM-mix1 for all the load increments, while AAM-mix2 and OPC-mix2 had the same number of cracks after 30 kN.

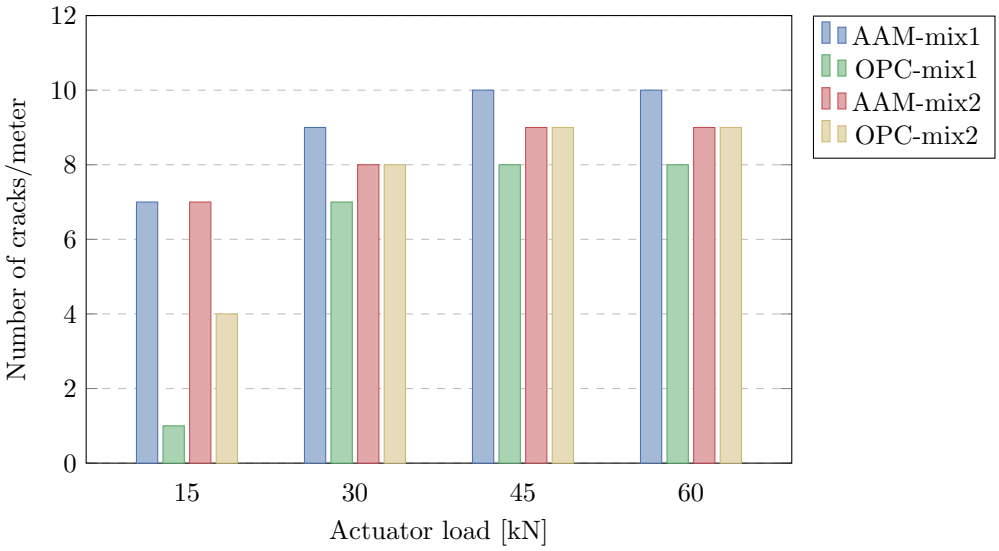

Figure 6.7: Number of cracks per meter length at paused load increments

The crack numbers per meter length in terms of the mid-span deflection is given in Figure 6.8. These results can be used to explain the number of cracks that formed for each mix. AAM-mix1 had a large mid-span deflection, which caused more cracks to form. Therefore, OPC-mix1 had less cracks than AAM-mix1, as the mid-span deflection was smaller. The larger deflections for the AAM-mixes, also caused more initial cracks to form (See initial jump in Figure 6.8). Although, AAM-mix2 had more initial cracks than OPC-mix2, the two mixes had the same number of cracks at 30 kN up until 60 kN. This was due to AAM-mix2 only having a slightly larger mid-span deflection than that OPC-mix2.

A more defined development of the crack distribution would have been obtained if the cracks were measured at smaller load increments. However, the results were still sufficient to compare the crack distributions for the AAM-mixes and the OPC-mixes.

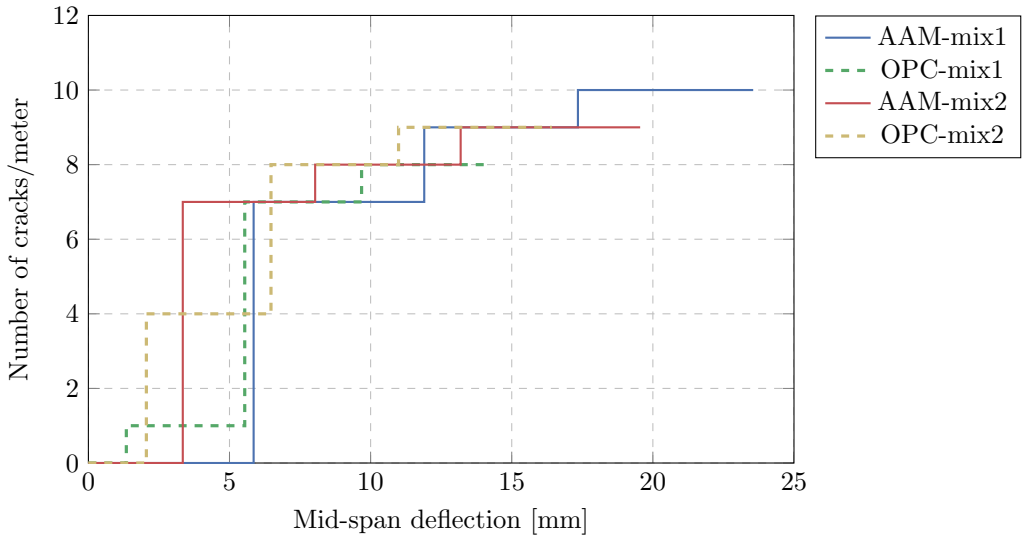

Figure 6.8: Number of cracks per meter length vs deflection

6.1.3.2 Crack widths

The average crack widths, which is considered between the two concentrated loads, at the different load increments are given in Figure 6.9. Although all the mixes had the same average crack widths at 15 kN, it should be noted that there was a difference in the number of cracks, with the AAM-mixes having more cracks over the considered length. For the other load increments, both the AAM-mixes had larger crack widths than the OPC-mixes.

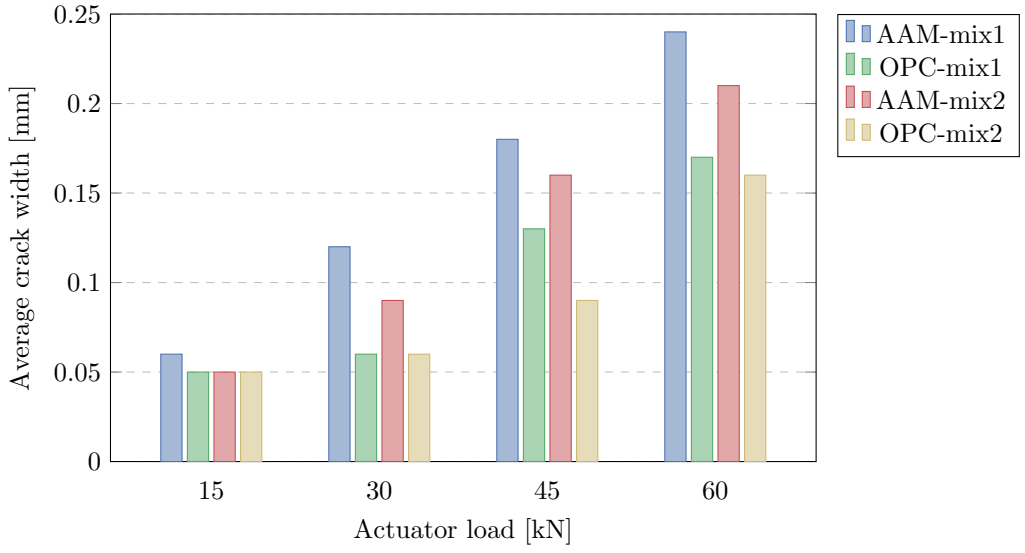

Figure 6.9: Average crack width at paused load increments

In Figure 6.10, the average crack widths are given in terms of the mid-span deflection. Again, the deflections for the different mixes clarified the crack widths that was obtained. The deflections for the OPC-mixes at the different load increments were smaller than the AAM-mixes. This resulted in smaller crack widths for the OPC-mixes, while the cracks for the AAM-mixes were

wider to accommodate for the large deflections.

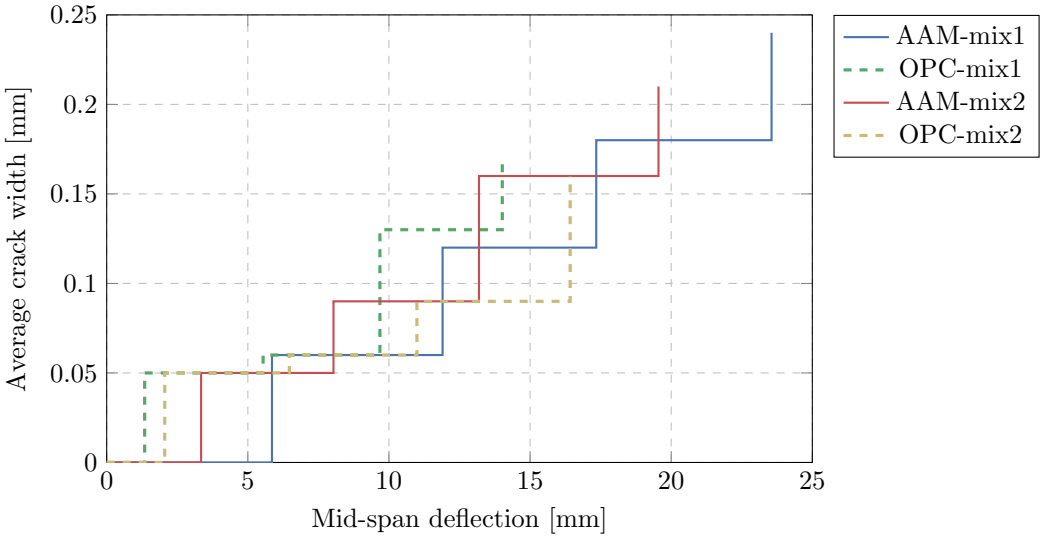

Figure 6.10: Average crack width vs deflection

These larger crack widths for AAMs, is a major concern in terms of durability. This allows for the ingress of aggressive agent, which deteriorates the concrete and causes the reinforcement to corrode (Ballim et al., 2009). Therefore, attention should be given to the crack widths of AAMs in order to find ways to reduce them.

6.1.4 Conclusion of reinforced beam results

The typical reinforced beam behaviour was obtained for both AAM-mixes and OPC-mixes. This was demonstrated with the moment-deflection curves as well as the crack formations that occurred for each RB specimen.

The flexural capacity of AAM-mix1 was only slightly lower than that of OPC-mix1, while AAM-mix2 and OPC-mix2 obtained similar values. The calculated ultimate moments were also relatively close to the experimental moments. This indicates that the current design codes can be used for the design of AAM structures in terms of flexural capacity. However, careful attention has to be given to the deflections of AAMs, as the AAM-mixes had larger deflection than the OPC-mixes. This was due to the low elastic modulus for AAMs. Although AAM-mix2 had a large deflection, the mix demonstrated that the deflections can be improved with a higher elastic modulus. Further investigation is also required for the deflection calculations of reinforced AAMs, as the EN 1992-1-1, (2004) seems to be conservative. Both the AAM-mixes and OPC-mixes had relatively the same ductility and dissipated energy.

The AAMs had a larger crack distribution with wider cracks than the OPC mixes. The large deflection for AAMs contributed to these crack formation. Effectively, this should improve if the deflections are reduced.

6.2 Pull-out tests

The results for the pull-out (PO) test, which is described and specified in Section 4.2.7, are provided in this section. The bond stress was plotted against the free-end slip of the reinforcement bar. This was done to obtain specific points on the bond-slip curve (referred to as the pull-out envelope in this study), which include adhesion loss, design bond stress, and the bond stress and free-end slip at peak failure. The results were also compared to the analytical model for the bond-slip behaviour, proposed by the Model Code, (2010).

6.2.1 General pull-out behaviour

As discussed in Section 3.7, bond stresses occur between the concrete and the reinforcement in order to transfer the tensile force in the reinforcement to the concrete matrix. These bond stresses increase as the tensile force increase, effectively causing the bar to slip from the concrete. This bond-slip behaviour is demonstrated by the analytical model proposed by the Model Code, (2010), in Figure 3.5 (See Section 3.7).

When a tensile force (T) is applied axially onto an embedded bar, two failure modes generally exists, namely pull-out and splitting failure. These failure modes are associated with the internal stresses that occur during the tensile loading, as shown in Figure 6.11. The chemical adhesion between the concrete and the reinforcement is considered as the adhesion stresses (v_a), and the first indication of loss of bond capacity due to micro-slip. After adhesion is lost, the bond is resisted by the bearing (v_b) and shear (v_s) stresses, considered as the mechanical bond. The bearing stress is taken as the pressure of the reinforcement bar ribs on the concrete, which effectively causes the concrete keys, between the ribs, to crush and bar slip to occur. The slip of the bar causes shear stresses on the surface of the concrete located in the cylindrical portion between the ribs (De Villiers, 2015a).

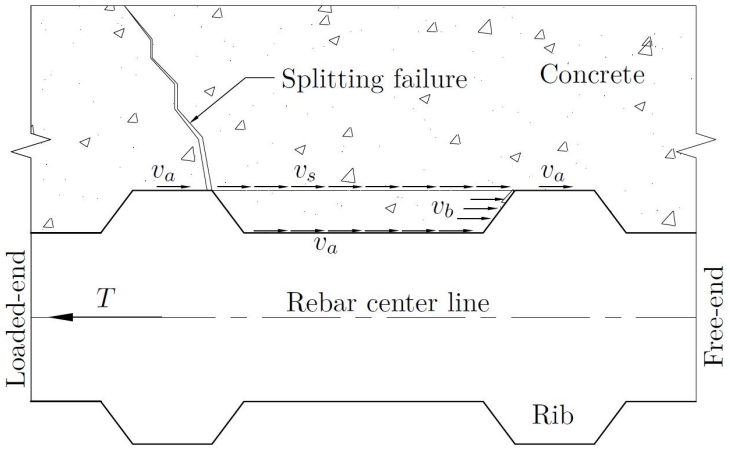

Figure 6.11: Stresses present during the axial tensile loading of embedded reinforcement bar, which include the adhesion stress (v_a), bearing stress (v_b) and shear stress (v_s) (De Villiers, 2015a).

When the combination of the shear stress and the bearing stress reaches the capacity of that for concrete, a slip failure surface is created. This will result in the bar being pulled out of the concrete (pull-out failure), where the only resisting force is friction between the concrete surfaces. In the case where the bar slip (caused by the bearing stress crushing the concrete) is resisted by the shear capacity, internal cracks start to form at the surface of the bar once the concrete tensile or strain capacity is reached. Splitting failure occurs due to the secondary cracks that form as a result of the internal cracks propagating to the surface of the concrete (Pedziwiatr, 2008).

These failure modes are highly dependent on the parameters of the reinforcement geometry. Stronger direct transverse stresses are generated with larger relative rib areas and bar diameters. This results in more aggressive formation of internal cracks, therefore, ensuring that splitting failure occurs. The embedded lengths also influences the failure mode. Pull-out failure is typically obtained with shorter embedded lengths, while longer embedded lengths causes splitting failure. The force required to pull the bar from the concrete, increases with larger embedded lengths. This causes larger internal stresses, resulting in the formation of internal cracks (De Villiers, 2015a). In this study, a short embedded length of 3ϕ was used to obtain pull-out failure. However, it should be noted that splitting failure occurred for some of the specimens.

The stress at adhesion loss (σ_a) was obtained from the pull-out envelopes, as presented in Figures 6.12 to 6.15. Adhesion loss is considered as the first failure of the bond resistance and assumed to be at the first measurement of free-end slip. Adhesion starts to develop at the loaded-end and progresses to the free-end. Therefore, at the first free-end measurement, the entire embedded length has lost adhesion. In this study the loss of adhesion was taken at the free-end LVDT measurement of 0.001 mm. The design bond stress was also obtained from the pull-out envelopes. As discussed in Section 3.7, the design point was taken at the free-end slip of 0.1 mm (Penelis et al., 2014).

In order to improve the presentation of the adhesion loss and the design point on the pull-out envelopes, the region on the graph between a slip of 0 mm and 0.2 mm, was enlarged with a factor of 5. The background in this region was left in white, while a grey background was used for the rest of the graph. It should be noted that the change of gradient in the pull-out envelopes obtained at the transition between the enlarge and normal regions, are only due to the transition of scaling and not a physical phenomena. At 0.1 mm a vertical dashed line is used to indicate the design point.

It was assumed that a constant and uniform bond stress distribution acted on the bar surface, as short embedded lengths were used. Therefore, the tensile force in the bar was divided by the surface area in contact to obtain the uniform bond stress. The surface area in contact was taken as a cylinder with a diameter equal to the nominal bar diameter and a height equal to the embedded length.

6.2.2 Pull-out envelope

The AAM-mixes are compared with the OPC-mixes in the PO envelopes, as shown in Figures 6.12 to 6.15. The different bar diameters (12 mm and 16 mm) for each of the mixes (mix 1 and mix 2) were plotted on separate graphs. The analytical model from the Model Code, (2010) for each mix and bar diameter were also plotted on the respective graphs. As expected, the majority of the PO specimens exhibited pull-out failure. A summary of the stress at adhesion loss, design bond stress, and the peak bond stress with the slip occurring at this point, is provided in Tables 6.4 and 6.5 for all the PO specimens. The design bond stress was also calculated according to the EN 1992-1-1, (2004) for each mix. The calculated design bond stress divided by the experimental value provides a factor that indicates how conservative the calculated values are. Low factor values indicate the calculated values are more conservative, while higher factor values indicate less conservative calculated values.

Figure 6.12 demonstrates the pull-out behaviour for AAM-mix1 and OPC-mix1 containing 12 mm reinforcement. Both the OPC-mix specimens obtained similar PO envelopes, while the results for the two AAM-mix specimens were different. Comparing the AAM-mix with the OPC-mix, it can be observed that the AAM envelopes were significantly lower than the OPC envelopes. Thus, the AAM-mix had smaller peak stresses than the OPC-mix, while less slip also occurred at these peak stresses (refer to Table 6.4). The bond stress is dependent on the compressive strength of the material. Therefore, the lower compressive strength for the AAM-mix, as given in Table 6.6, resulted in smaller bond stress values. However, the stress at adhesion loss was higher for the AAM-mix than for the OPC mix. This indicates that the AAM-mix had a better initial bond with the reinforcement compared to the OPC-mix. AAM-mix1 (Specimen 1) also obtained a higher design bond stress than the OPC-mix. The design bond stress between AAM-mix1 (Specimen 2) and the OPC-mix was similar. Both the AAM-mix and the OPC-mix had lower calculated design bond stresses than that obtained from the PO envelope, while the design bond factors for the AAM-mix was more conservative than the OPC-mix. This indicates that shorter embedded lengths can possibly be used with the higher design bond stress for the AAM-mix.

It should be noted that the loss of adhesion stress and design bond stress for AAM-mix1 (Specimen 1) were close to the specimen's peak stress and also higher than that obtained for AAM-mix1 (Specimen 2). Therefore, the stresses used during the design should be lower than that given for AAM-mix1 (Specimen 1) in order to be conservative. The values that was obtained for these specific stresses, as mentioned above, are given in Table 6.4.

The analytical model proposed by the Model Code, (2010), was lower than the measured results for the OPC-mixes. These higher peaks for the OPC concrete in comparison to the model, was also reported by De Villiers, (2015a). Except for the initial bond stresses, the PO curve for AAM-mix1 (Specimen 1) followed the trend of the analytical model reasonably well. However, for AAM-mix1 (Specimen 2), the measured results were lower than the model after the peak bond stress was reached. Therefore, the analytical model should be adjusted for AAMs.

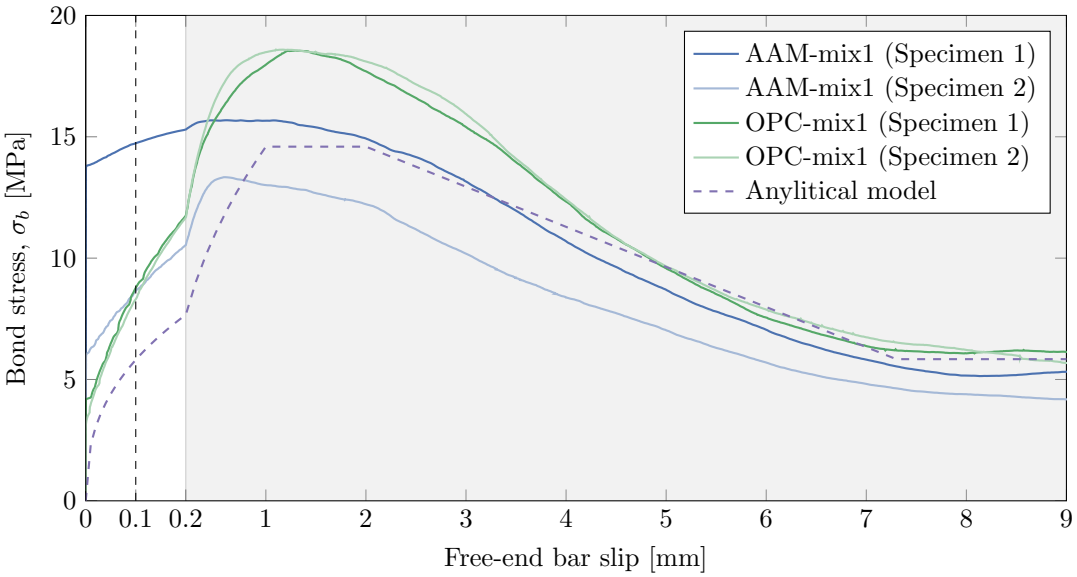

Figure 6.12: The uniform bond stress development versus free-end bar slip for the 12 mm reinforcement PO tests with AAM-mix1 and OPC-mix1. The graph also includes the analytical bond-slip model proposed by the Model Code, (2010)

The bond stress development for the 12 mm reinforcement embedded in AAM-mix2 and OPC-mix2, are given in Figure 6.13. Again, the PO envelopes were higher for the OPC-mix than for the AAM-mix due to the difference in the compressive strength (See Table 6.6), while the AAM-mix had a better adhesion loss. The design bond stresses varied for both the AAM-mix and the OPC-mix, with a high design bond stress for AAM-mix2 (Specimen 1) and OPC-mix2 (Specimen 1), while AAM-mix2 (Specimen 2) and OPC-mix2 (Specimen 2) had lower design bond stresses. The high design bond stress for the OPC-mix can be attributed to the sharp initial increase in the bond with little slip after adhesion was lost, while the AAM-mix had a high design bond stress due to the large stress at the loss of adhesion. Again, the calculated design bond stresses were lower than the experimental values, demonstrating that it is possible to calculate the design bond stress for AAMs, using the EN 1992-1-1, (2004). Table 6.4 provides a summary of the specific stress values that was obtained for each specimen.

For the OPC-mix, the measured values after the peak stress was lower than the analytical model obtained for the second mixes (note that this model has a lower peak value than the model for the first mixes in Figure 6.12). However, peak bond stresses that was measured for the OPC-mix correlated with the peak stress of the model. This is unexpected, as the model generally gives a lower bound solution in comparison with measured results for OPC concrete (De Villiers, 2015a). Similar to the OPC-mix, the bond stress for AAM-mix2 (Specimen 1) was lower than the analytical model after the peak bond stress. AAM-mix2 (Specimen 2) followed the model up until the measured peak stress, after which the bond stress was lower than the analytical model. This also demonstrates that the analytical model cannot be used for AAMs and must be adjusted.

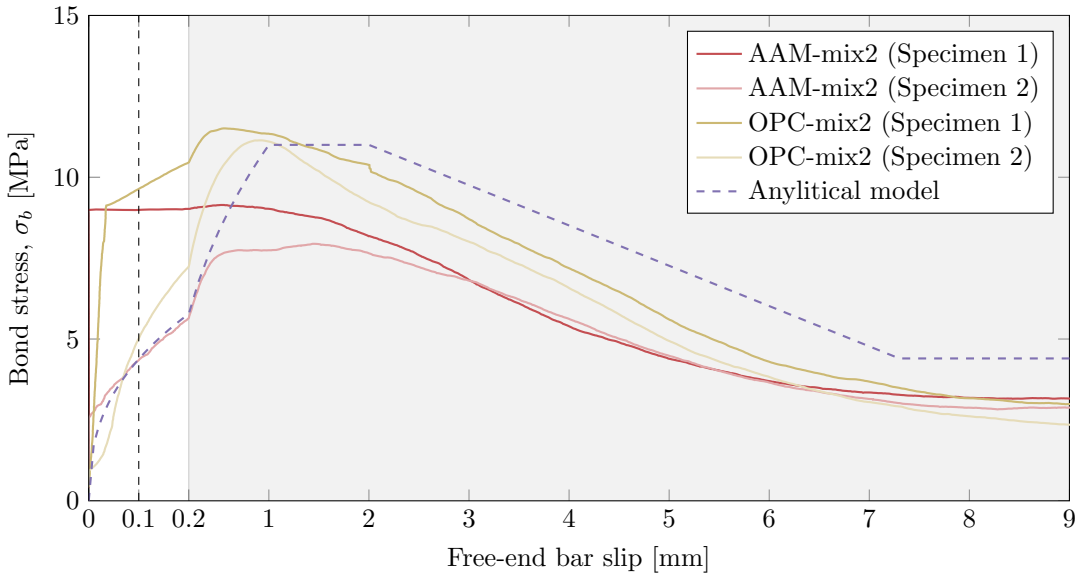

Figure 6.13: The uniform bond stress development versus free-end bar slip for the 12 mm reinforcement PO tests with AAM-mix2 and OPC-mix2. The graph also includes the analytical bond-slip model proposed by the Model Code, (2010)

The values that was obtained for loss of adhesion stress, design bond stress and the peak bond stress of the PO-specimens with 12 mm embedded reinforcement bar, are given in Table 6.4. The slip that occurred at the peak stresses is also provided.

Table 6.4: Results obtained from the PO envelopes for the 12 mm reinforcement PO specimens

Specimen	σ_a [MPa]	Design bond stress (σ_d) [MPa]			Peak	
		Experimental	Calculated	Factor	σ_{bmax} [MPa]	free-slip [mm]
AAM-mix1 (Specimen 1)	13.78	14.74	2.25	0.15	15.68	0.613
AAM-mix1 (Specimen 2)	6.02	8.69	2.25	0.25	13.34	0.594
OPC-mix1 (Specimen 1)	4.19	8.78	3.75	0.43	18.55	1.294
OPC-mix1 (Specimen 2)	3.24	8.31	3.75	0.45	18.59	1.101
AAM-mix2 (Specimen 1)	8.99	9.00	1.95	0.22	9.14	0.521
AAM-mix2 (Specimen 2)	2.59	4.35	1.95	0.45	7.94	1.454
OPC-mix2 (Specimen 1)	0.54	9.64	2.70	0.28	11.51	0.548
OPC-mix2 (Specimen 2)	0.92	5.01	2.70	0.54	11.14	0.916

The pull-out envelopes for the 16 mm reinforcement embedded within AAM-mix1 and OPC-mix1, are given in Figure 6.14. Similar results were obtained between the AAM-mix and the OPC-mix, with the envelope for each specimen being close to one another. However, splitting failure occurred in AAM-mix1 (Specimen 2), as a sudden drop in the bond stress occurred after the peak stress was reached. The reason for the different failure modes for the two AAM-mix specimens, could be due to small internal cracks that already existed within AAM-mix1 (Specimen 2). Therefore, the higher internal stresses caused by the larger bar diameter and rib areas of the 16 mm reinforcement, contributed to these internal cracks propagating to the surface and in turn causing splitting failure. Similar results were obtained for all the specimens in terms

of the stress at adhesion loss, the design bond stress and the peak stress, with only OPC-mix1 (Specimen 1) obtaining a lower adhesion loss stress and a design bond stress (See Table 6.5). The lower compressive strength for the AAM-mix, resulted in a lower calculated design bond stress. Therefore, the calculated design bond stress for the AAM-mix was more conservative than the OPC-mix, as similar experimental values were obtained. This is demonstrated by the factors in Table 6.5.

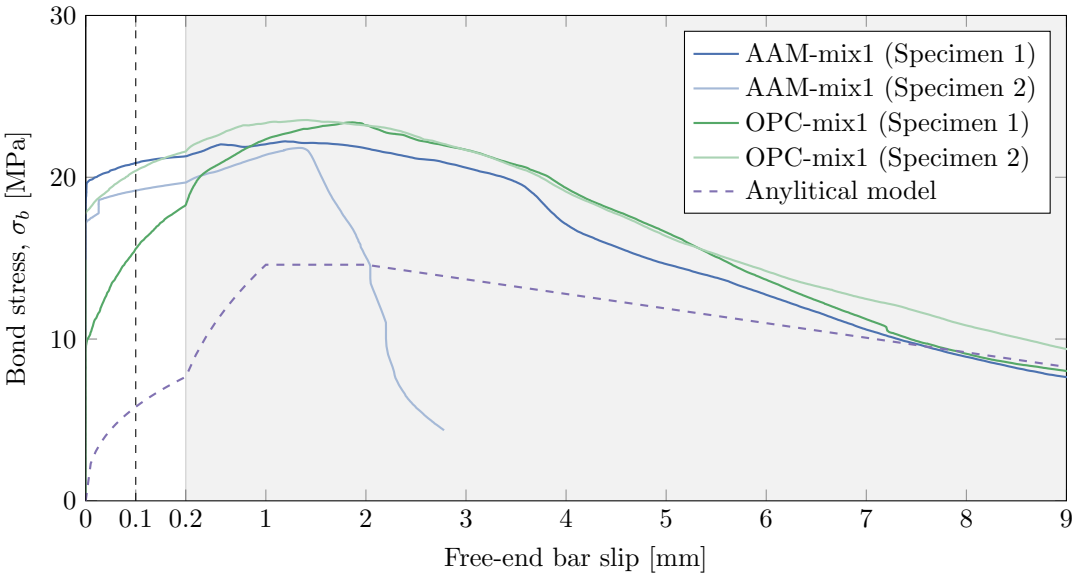

Figure 6.14: The uniform bond stress development versus free-end bar slip for the 16 mm reinforcement PO tests with AAM-mix1 and OPC-mix1. The graph also includes the analytical bond-slip model proposed by the Model Code, (2010)

A lower bound solution was obtained for the analytical model in terms of both AAM-mix1 and OPC-mix1 containing 16 mm reinforcement. It should be noted that the analytical model does not consider the effect of the bar dimensions on the bond stress. An increase in bond stress is obtained for reinforcement with larger diameters and rib areas. This increase in the bond stress between the 12 mm and 16 mm bar, can be observed when comparing the results in Figures 6.12 and 6.13. Therefore, the peak stress for the analytical model should be higher.

In Figure 6.15, the pull-out results are given for AAM-mix2 and OPC-mix2 containing 16 mm reinforcement. Pull-out occurred for all of the mixes, but OPC-mix2 (Specimen 2) eventually exhibited splitting failure. The splitting failure is demonstrated with the slip value at the peak stress, first increasing before the bond stress had a sudden drop. Again this failure mode can be attributed to the larger bar diameter and rib areas, which contributed to the development of internal cracks that might have existed within OPC-mix2 (Specimen 2). The peak stresses for the AAM-mix were lower than the OPC-mix, with both obtaining relatively the same slip values (approximately between 1 mm and 1.5 mm) at this point. At the adhesion loss, the AAM-mixes had larger stresses than the OPC-mix, while similar design bond stresses to OPC-mix2 (Specimen 2) were obtained for the AAM-mix. Therefore, the initial bond between AAM-mix and the 16 mm bar is also stronger than that for the OPC-mix. The calculated design bond stresses for the AAM-mix were again more conservative than the OPC-mix as a result of the

compressive strength. The values for the stresses at the specified points, are given in Table 6.5.

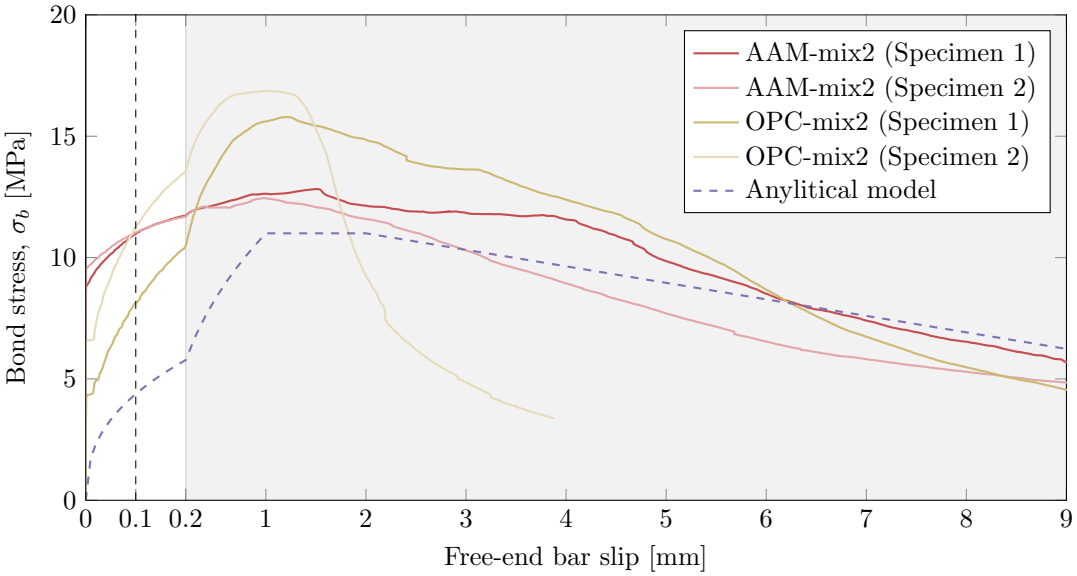

Figure 6.15: The uniform bond stress development versus free-end bar slip for the 16 mm reinforcement PO tests with AAM-mix2 and OPC-mix2. The graph also includes the analytical bond-slip model proposed by the Model Code, (2010)

The analytical model was again lower than the measured results for the AAM-mix and the OPC-mix with 16 mm embedded bar, due to the model not taking the reinforcement dimensions into account. If the bond stress for the analytical model was increased to consider the reinforcement dimensions, the bond stress for the AAM-mix will be lower than the model. This is due to the peak stresses for the AAM-mix only being slightly higher than the analytical model, as given in Figure 6.15.

The stress at adhesion loss, bond stress and peak stress with the slip occurring at the peak stress, are given in Table 6.5 for all the specimens containing 16 mm reinforcement.

Table 6.5: Results obtained from the PO envelopes for the 16 mm reinforcement PO specimens

Specimen	σ_a [MPa]	Design bond stress (σ_d) [MPa]			Peak	
		Experimental	Calculated	Factor	σ_{bmax} [MPa]	free-slip [mm]
AAM-mix1 (Specimen 1)	18.98	20.88	2.25	0.11	22.22	1.194
AAM-mix1 (Specimen 2)	17.21	19.18	2.25	0.12	21.81	1.333
OPC-mix1 (Specimen 1)	9.65	15.58	3.75	0.24	23.39	1.863
OPC-mix1 (Specimen 2)	17.84	20.40	3.75	0.18	23.54	1.401
AAM-mix2 (Specimen 1)	8.79	10.98	1.95	0.18	12.83	1.519
AAM-mix2 (Specimen 2)	9.55	11.04	1.95	0.18	12.46	0.978
OPC-mix2 (Specimen 1)	4.04	8.14	2.70	0.33	15.79	1.215
OPC-mix2 (Specimen 2)	6.58	11.28	2.70	0.24	16.86	1.029

The compressive strength and the elastic modulus for the AAM-mixes and the OPC-mixes, are given in Table 6.6.

Table 6.6: Properties of PO specimens

Mix	$f_{c,cyl}$ [MPa]	E_c [GPa]
AAM-mix1	29.3	18.3
OPC-mix1	36.7	44.9
AAM-mix2	19.1	20.9
OPC-mix2	24.1	37.1

6.2.3 Conclusion of pull-out results

The AAM-mixes and OPC-mixes obtained typical pull-out behaviour for both the 12 mm and 16 mm embedded reinforcement bar, as demonstrated by the bond-slip curves given in this section. The majority of the specimens exhibited pull-out failure, due to the short embedded length of 3ϕ. However, the larger dimensions of the 16 mm reinforcement, contributed to splitting failure for two of the PO specimens.

Although the peak bond stresses for the AAM-mixes were lower than the OPC-mixes, a better adhesion was obtained between the AAM-mixes and the reinforcement. This was indicated by the larger stresses at loss of adhesion for the AAM-mixes. The design bond stress for the AAMs were all either similar to or higher than the OPC-mixes. It was also demonstrated that the EN 1992-1-1, (2004) can be used to calculate the design bond stress for AAMs, as the calculated values were conservative compared to the bond stress obtained from the PO envelopes. This is beneficial for AAMs, as shorter embedded lengths can be used with a higher design bond stress. However, this should be further investigated.

The pull-out behaviour for AAMs was not represented well with the analytical models obtained from the Model Code, (2010). This was due to the lower peak stresses and the higher initial bond stresses for AAMs. Therefore, this analytical model should be adjusted for the use of AAMs.

Chapter 7

Conclusions and recommendations

7.1 Conclusions

The aim of this study is to determine the structural use of alkali activated materials (AAMs) as an alternative construction material to Ordinary Portland cement (OPC) concrete. This was done by investigating the mechanical properties of a fly ash/slag based AAM activated by sodium silicate and sodium hydroxide, as well as the structural behaviour of the AAM with reinforcement. The following conclusions are drawn from this work:

7.1.1 Mechanical properties of AAMs

For the mechanical properties of AAMs, tests were performed to obtain the workability, compressive strength, density, elastic modulus and stress-strain relation. The parameters which were varied include: the type of activator; the calcium content; the activator concentration; the dosage; the modulus of the activator; and the coarse aggregate content and size. The following conclusions were made:

7.1.1.1 Workablity

- Most of the AAMs exhibited self-compacting characteristics, as the mixes were flowable, while the coarse aggregate remained within the paste without separating.
- The workability was mainly influenced by the solution to binder ratio. In order to obtain the specific values for the different parameters, the amount of alkaline activator was varied, resulting in an increase or decrease in the solution to binder ratio.
- It was found that solution to binder ratio's between 0.4 and 0.62 resulted in promising workability in terms of flowability and segregation.

7.1.1.2 Compressive strength

- Promising compressive strengths of up to 67.1 MPa, were obtained for the AAM mixes.

- The mixes containing sodium silicate and sodium carbonate as alternative activators, did not obtain any strength, except for the mix with slag as the only binder material. This indicates that the binder plays an important role when alternative activators are used.
- The compressive strength increased with an increase in the calcium content. The presence of calcium in the binder causes the formation of C-S-H reaction products, and in turn an increase in strength.
- Higher sodium hydroxide concentration caused a significant increase in the compressive strength. More OH^- are available with high concentrations to dissolve the aluminosilicate in the binder.
- The activator dosage had no effect on the compressive strength of AAMs.
- For the 40 % slag content, the compressive strength decreased with an increase in activator modulus, while for the 20 % slag an optimum activator modulus of 1 was obtained.
- The coarse aggregate content and size did not influence the compressive strength.
- The cylinder strengths were slightly lower than the 80 % cube strength values, typically used for OPC concrete. Therefore, the relationship between the cube strength and the cylinder strength for AAMs should be adjusted.

From these results, it was evident that the compressive strength of AAMs were influenced by the calcium content, sodium hydroxide concentration and the activator modulus, with the concentration having the most significant influence. These relationship between the constituents and the strength can possibly used for future design methods of AAMs.

7.1.1.3 Density

- The densities were slightly lower than 2400 kg/m^3, which is typically obtained for OPC concrete.
- The densities of the AAM mixes followed the trend of the compressive strength results. The calcium content and sodium hydroxide concentration caused an increase in the density, while a decrease was obtained for the activator modulus. Again, the activator dosage had no effect on the density.

7.1.1.4 Elastic modulus

- The elastic modulus for the AAM mixes were generally very low compared to OPC concrete, with values between 8.2 GPa and 32.1 GPa.
- An increase in elastic modulus was obtained with a higher slag content (calcium content).
- The high sodium hydroxide concentrations yielded larger elastic modulus values for the AAM mixes.

- There was no relationship between the activator dosage and the elastic modulus.
- The increase in the activator modulus caused a decrease in the elastic modulus.
- The aggregate content did not significantly influence the elastic modulus.

The sodium hydroxide concentration, the calcium content and the activator modulus had the largest influence on the elastic modulus. Therefore, in order to obtain sufficient elastic modulus values for AAMs, a high calcium content, high sodium hydroxide concentration and low activator modulus should be used.

7.1.1.5 Stress-strain relationship

- There was no clear trend between the different parameters of the AAM mixes and the stress-strain relationship.

7.1.2 Structural behaviour of reinforced AAMs

In order to obtain the flexural behaviour of reinforced AAMs, beams with reinforcement were tested in bending. Reinforcement pull-out tests were performed to obtain the bond between AAMs and the reinforcement. For both these tests, two AAM mixes were compared against two OPC mixes with similar strengths. The following conclusions were made:

7.1.2.1 Bending behaviour of reinforced AAM beams

- Both the AAM-mixes and the OPC-mixes demonstrated typical flexural behaviour for reinforced beams in terms of the moment-deflection curves and the crack formation.
- AAM-mix1 had a slightly lower ultimate moment than OPC-mix1, while similar moments were obtained between AAM-mix2 ans OPC-mix2. This was due to the strengths that was obtained for these mixes. The calculated ultimate moments also compared well with the experimental results.
- The AAM-mixes had larger deflections than the OPC-mixes. The low elastic modulus values for the AAM-mixes contributed to these large deflections. However, it was demonstrated with AAM-mix2, that the deflections decreased with improved elastic modulus. However, the deflections for the AAM-mixes were still larger than the calculated values.
- Similar values were obtained for the ductility index and the energy dissipated between the AAM-mixes and the OPC-mixes.
- A larger crack distribution and wider crack widths were obtained for the AAM-mixes. This was mainly due to the AAM-mixes having larger deflections than the OPC-mixes.

These results demonstrated that it is possible to design reinforced AAM beams with the use of the design codes, such as the EN 1992-1-1, (2004). However, the elastic modulus of AAMs has to be improved in order to reduce the large deflections, and in turn also reduce the crack distribution and crack widths of reinforced AAM beams. The design codes also seem to be inadequate for the deflection calculations of AAMs, and need to be adjusted.

7.1.2.2 Bond between reinforcement and AAMs

- Typical pull-out behaviour was obtained for the 12 mm and 16 mm reinforcement embedded in the AAM-mixes and the OPC-mixes. This was demonstrated by the bond-slip (PO) envelopes. Pull-out failure was obtained due to short embedded lengths, while two of the specimens exhibited splitting failure as a result of the reinforcement dimensions.
- The AAM-mixes obtained lower peak stresses than the OPC-mixes. This was mainly due to the lower strengths for the AAM-mixes.
- The AAM-mixes had larger adhesion loss stresses than the OPC-mixes. This indicates that a better adhesion bond was obtained between AAMs and the reinforcement.
- For the AAM-mixes, the design bond stresses were similar to or higher than the OPC mixes. The calculated design bond stresses were also conservative compared to the bond stresses that was obtained from the PO envelopes. With higher design bond stresses for AAMs, shorter embedded lengths can possibly be used.
- The analytical model, as given by the Model Code, (2010), provided a poor representation of the pull-out behaviour for the AAM-mixes. The peak stresses for AAM-mixes were lower than the analytical model, while the initial bond stresses (adhesion loss and design point) were higher than than the analytical model. Therefore, the analytical model should be adjusted for AAMs.

Although the peak bond stresses for the AAM-mixes were lower than the OPC-mixes, the design bond stress is more important, as the design bond stress is used to represent the bond capacity between concrete and reinforcement in design codes. Therefore, with the higher design bond stresses for AAMs, it can be concluded that the design codes, such as the EN 1992-1-1, (2004), can be used to calculate the design bond stress for AAMs, as the code is conservative.

7.2 Recommendations

The knowledge gained from this study, identified the following important areas for further research:

- The rapid setting times for AAMs require further investigation, as this will make it difficult to cast AAMs on construction sites.

- The solution to binder ratio should be limited between 0.4 and 0.62 in order to avoid very stiff mixes or flowable mixes that segregate. However, these limitations will vary when different amounts of binder is used.
- The leaching of the white efflorescence can be prevented by curing the specimens in plastic bags to avoid contact with CO_2.
- More research is required on the causes for the surface cracks that form when the AAMs harden. These cracks are a concern in terms of the durability of AAMs.
- The results for the alternative activators were contradicting with previous research and require further investigation.
- Even though promising results were obtained for the elastic modulus of AAMs, further research is still necessary. The importance of the elastic modulus was demonstrated with the deflections of reinforced AAM beams. Therefore, this value needs to be improved and properly predicted.
- Further knowledge is required on the flexural behaviour of reinforced AAMs, as only two different mixes were investigated in this study. Better comparisons between AAMs and OPC concrete can be obtained with a more in-depth study.
- The shear behaviour of reinforced beams can also be investigated, as only the bending behaviour was investigated in this study.
- The bond behaviour between AAMs and reinforcement was only investigated for two different reinforcement sizes with one embedded length. Thus, a more in-depth study can be done on the bond-behaviour of AAMs with reinforcement in order to draw better conclusions.
- Only the mechanical properties and structural behaviour of AAMs were investigated in this study. More focus should be placed on the chemistry behind the reactions that occur and products that form within AAMs, in order to gain a better understanding of the final molecular structure and its relation to the mechanical properties of AAMs.

7.3 Concluding statement

This study provided a significant amount of knowledge on the mechanical properties and the structural behaviour of AAMs. However, it can be concluded that the AAMs is still some time away from being used as a structural material, as there is still a number of issues, like the low elastic modulus, that need to be addressed. This study presented a good basis for further research into these issues. AAMs have great potential as a structural material, if these problems are solved.

References

ACI Committee 232 (2002). *Use of Fly Ash in Concrete*. Americal Concrete Institute.

ASTM E8/E8M-09 (2011). *Standard Test Methods for the Tension Testing of Materials*. ASTM International. West Conshohocken, Pennsylvania, USA.

ASTM Standard C618 (2012). *Standard Specification for Coal Fly Ash and Raw or Calcined Natural Pozzolan for Use in Concrete*. ASTM International. West Conshohocken, Pennsylvania, USA.

Adam, A. (2009). 'Strength and durability properties of alkali activated slag and fly ash-based geopolymer concrete'. M.Sc(Eng). RMIT University.

Addis, B. and Goodman, J (2009). 'Concrete mix design'. In: *Fulton's concrete technology*. Ed. by G. Owens. Ninth Edit. Midrand, South Africa: Cement & Concrete Institute. Chap. 11, pp. 219–228.

Alexander, M. and Beushausen, H. (2009). 'Deformation and volume change of hardened concrete'. In: *Fulton's concrete technology*. Ed. by G. Owens. Ninth Edit. Midrand, South Africa: Cement & Concrete Institute. Chap. 8, pp. 111–154.

Álvarez-Ayuso, E., Querol, X., Plana, F., Alastuey, A., Moreno, N., Izquierdo, M., Font, O., Moreno, T., Diez, S., Vázquez, E. and Barra, M. (2008). 'Environmental, physical and structural characterisation of geopolymer matrixes synthesised from coal (co-)combustion fly ashes'. In: *Journal of Hazardous Materials* 154.1-3, pp. 175–183.

Arioz, E., Arioz, O. and Mete Kockar, O. (2012). 'An Experimental Study on the Mechanical and Microstructural Properties of Geopolymers'. In: *Procedia Engineering* 42, pp. 100–105.

Astutiningsih, S. and Liu, Y. (2005). 'Geopolymerisation of Australian slag with effective dissolution by the alkali'. In: *Proceedings of the World Congress Geopolymer*. Ed. by Joseph Davidovits. Geopolymer Institute, pp. 69–74.

Bakharev, T., Sanjayan, J.G. and Cheng, Y.B. (1999). 'Alkali activation of Australian slag cements'. In: *Cement and Concrete Research* 29.1, pp. 113–120.

Ballim, Y., Alexander, M. and Beushausen, H. (2009). 'Durability of concrete'. In: *Fulton's concrete technology*. Ed. by G. Owens. Ninth Edit. Midrand, South Africa: Cement & Concrete Institute. Chap. 9, pp. 155–188.

Barnard, R. (2014). 'Mechanical properties of fly ash/slag based geopolymer concrete with the addition of macro fibres'. Masters. Stellenbosch University.

Ben Haha, M., Le Saout, G., Winnefeld, F. and Lothenbach, B. (2011). 'Influence of activator type on hydration kinetics, hydrate assemblage and microstructural development of alkali activated blast-furnace slags'. In: *Cement and Concrete Research* 41.3, pp. 301–310.

Benaim, R. (2008). *The Design of Prestressed Concrete Bridges. Concepts and principles*. Taylor & Francis.

Bernal, S.A., Mejía de Gutiérrez, R., Pedraza, A.L., Provis, J.L., Rodriguez, E.D. and Delvasto, S. (2011). 'Effect of binder content on the performance of alkali-activated slag concretes'. In: *Cement and Concrete Research* 41.1, pp. 1–8.

Bernal, S.A., Mejía de Gutiérrez, R. and Provis, J.L. (2012). 'Engineering and durability properties of concretes based on alkali-activated granulated blast furnace slag/metakaolin blends'. In: *Construction and Building Materials* 33, pp. 99–108.

Collins, F. and Sanjayan, J.G. (1998). 'Early age strength and workability of slag pastes activated by NaOH and Na_2CO_3'. In: *Cement and Concrete Research* 28.5, pp. 655–664.

Collins, F. and Sanjayan, J.G. (1999). 'Workability and mechanical properties of alkali activated slag concrete'. In: *Cement and Concrete Research* 29.3, pp. 455–458.

Collins, F. and Sanjayan, J.G. (2001). 'Early age strength and workabliltiy of slag pastes activated by sodium silicates'. In: *Magazine of Concrete Research* 53.5, pp. 321–326.

Combrinck, R (2015a). *Lecture: Aggregates and mixing water*. Stellenbosch Campus.

Combrinck, R (2015b). *Lecture: Cement, hydration and extenders*. Stellenbosch Campus.

Dae-Jin, K., Min Sook, K., Geun Young, Y. and Young Hak, L. (2014). 'Bond strength of steel deformed rebars embedded in artificial lightweight aggregate concrete'. In: *Journal of Adhesion Science and Technology* 27.5-6, pp. 1–11.

Davidovits, J. (1989). 'Geoplymers and geopolymeric materials'. In: *Journal of Thermal Analysis* 35.2, pp. 429–441.

Davidovits, J. (1994). 'Properties of Geopolymer Cements'. In: *First International Conference on Alkaline Cements and Concretes*, pp. 131–149.

Davidovits, J. (2011). *Geopolymer chemistry and applications*. Geopolymer Institute.

Davidovits, J. (2013). *Geopolymer cement: A review*. Tech. rep. Geopolymer Institute, pp. 1–11.

De Villiers, J.P. (2015a). 'Bond Behaviour of Deformed Steel Reinforcement in Lightweight Foamed Concrete'. Masters. Stellenbosch University.

De Villiers, W.I. (2015b). *Lecture: Sustainability of Cement-Based Materials*. Stellenbosch Campus.

Diaz, E.I., Allouche, E.N. and Eklund, S. (2010a). 'Factors affecting the suitability of fly ash as source material for geopolymers'. In: *Fuel* 89.5, pp. 992–996.

Diaz, E.I. and Allouche, E.N. (2010b). 'Recycling of fly ash into geopolymer concrete: Creation of a database'. In: *2010 IEEE Green Technologies Conference*.

Douglas, E., Bilodeau, A. and Malhotra, V.M. (1992). 'Properties and durability of alkaline-activated slag concrete'. In: *ACI Materials Journal* 89.5, pp. 509–516.

Duxson, P. (2009). 'Geopolymer precursor design'. In: *Geoplymers: Structures, processing, properties and application*. Ed. by J.L. Provis and J.S.J. Van Deventer. First Edit. Woodhead publishing. Chap. 3, pp. 37–49.

Duxson, P., Mallicoat, S.W., Lukey, G.C., Kriven, W.M. and Deventer, J.S.J. van (2007). 'The effect of alkali and Si/Al ratio on the development of mechanical properties of metakaolin-based geopolymers'. In: *Colloids and Surfaces A: Physicochemical and Engineering Aspects* 292.1, pp. 8–20.

EN 12350-2 (2009). *Testing fresh concrete. Part 2: Slump-test*. Londen, UK: British Standards Institute.

EN 12390-13 (2013). *Testing hardened concrete. Part 13: Determination of the secant modulus of elasticity in compression*. Londen, UK: British Standards Institute.

EN 12390-3 (2002). *Testing hardened concrete. Part 3: Compressive strength of test specimens*. Londen, UK: British Standards Institute.

EN 1992-1-1 (2004). *Eurocode 2: Design of concrete structures. Part 1-1: General rules and rules for buildings*. Londen, UK: British Standards Institute.

Evonik Industries (2010). *GPS Safety Summary for Sodium Hydroxide (NaOH)*.

Farghal Maree, A. and Hilal Riad, K. (2014). 'Analytical and experimental investigation for bond behaviour of newly developed polystyrene foam particles' lightweight concrete'. In: *Engineering Structures* 58.1, pp. 1–11.

Fernández-Jiménez, A. and Palomo, A (2003a). 'Characterisation of fly ashes. Potential reactivity as alkaline cements'. In: *Fuel* 82.18, pp. 2259–2265.

Fernández-Jiménez, A. and Puertas, F. (2003b). 'Effect of activator mix on the hydration and strength behaviour of alkali-activated slag cements'. In: *Advances in Cement Research* 15.3, pp. 129–136.

Fernández-Jiménez, A., Puertas, F., Sobrados, I. and Sanz, J. (2003c). 'Structure of Calcium Silicate Hydrates Formed in Alkaline-Activated Slag: Influence of the Type of Alkaline Activator'. In: *Journal of the American Ceramic Society* 86.8, pp. 1389–1394.

Fernández-Jiménez, A. and Palomo, A. (2005). 'Composition and microstructure of alkali activated fly ash binder: Effect of the activator'. In: *Cement and Concrete Research* 35.10, pp. 1984–1992.

Fernández-Jiménez, A., Palomo, A. and Criado, M. (2006a). 'Alkali activated fly ash binders. A comparative study between sodium and potassium activators'. In: *Materiales de Construcción* 56.281, pp. 51–65.

Fernández-Jiménez, A., Palomo, A. and López-hombrados, C. (2006b). 'Engineering Properties of Alkali-Activated Fly Ash Concrete'. In: 103.2, pp. 106–112.

Fernández-Jiménez, A., Palomo, A., Sobrados, I. and Sanz, J. (2006c). 'The role played by the reactive alumina content in the alkaline activation of fly ashes'. In: *Microporous and Mesoporous Materials* 91.1-3, pp. 111–119.

Garcia-Lodeiro, I., Palomo, A., Fernández-Jiménez, A. and Macphee, D.E. (2011). 'Compatibility studies between N-A-S-H and C-A-S-H gels. Study in the ternary diagram Na_2O-CaO-Al_2O_3-SiO_2-H_2O'. In: *Cement and Concrete Research* 41.9, pp. 923–931.

Garcia-Lodeiro, I., Palomo, A. and Fernández-Jiménez, A. (2015). 'An overview of the chemistry of alkali-activated cement-based binders'. In: *Handbook of alkali-activated cements, mortars and concretes*. Ed. by F. Pacheco-Torgal, J.A. Labrincha, C. Leonelli, A. Palomo and P. Chindaprasirt. Sawston, Cambridge, UK: Woodhead publishing. Chap. 2, pp. 19–47.

Geopolymer Institute (2013). *Geopolymer cement*. URL: `http://www.geopolymer.org/applications/geopolymer-cement/` (visited on 29/09/2015).

Gourley, J.T. (2014). 'Geopolymers in Australia'. In: *Journal of the Australian Ceramics Society* 50, pp. 102–110.

Grieve, G. (2009). 'Cementitious materials'. In: *Fulton's concrete technology*. Ed. by G. Owens. Ninth Edit. Midrand, South Africa: Cement & Concrete Institute. Chap. 1, pp. 1–16.

Hager, I. (2013). 'Behaviour of cement concrete at high temperature'. In: *Bulletin of the Polish Academy of Sciences: Technical Sciences* 61.1, pp. 1–10.

Hardjito, D. (2005). 'Studies on Fly Ash-Based Geopolymer Concrete'. Doctor of Philosphy. Curtin University of Technology.

Hardjito, D., Wallah, S.E., Sumajouw, D.M.J and Rangan, B.V. (2004). 'On the development of fly ash-based geopolymer concrete'. In: *ACI Materials Journal* 101.6, pp. 467–472.

Hardjito, D. and Rangan, B.V. (2005). *Development and properties of low-calcium fly ash-based geopolymer concrete*. Tech. rep. Faculty of Engineering Curtin University of Technology Perth, Australia.

Hibbeler, R.C. (2014). *Mechanics of Materials*. Pearson.

Khale, D. and Chaudhary, R. (2007). 'Mechanism of geopolymerization and factors influencing its development: A review'. In: *Journal of Materials Science* 42.3, pp. 729–746.

Kurt, C. and Bittner, J. (2006). 'Sodium Hydroxide'. In: *Ullmann's Encyclopedia of Industrial Chemisty* 33, pp. 371–382.

Kwan, A.K.H., Ho, J.C.M. and Pam, H.J. (2002). 'Flexural strength and ductility of reinforced concrete beams'. In: *Proceedings of the Institution of Civil Engineers: Structures and Buildings*, pp. 361–369.

Lagaly, G., Tufar, W., Minihan, A. and Lovell, A. (2000). 'Silicates'. In: *Ullmann's Encyclopedia of Industrial Chemisty* 32, pp. 509 –572.

Lawson, J.L. (2009). 'On the Determination of the Elastic Properties of Geopolymeric Materials Using Non-Destructive Ultrasonic'. Masters of Science.

Lewis, D.W. (1992). *Properties and uses of iron and steel slags*. URL: `http://www.nationalslag.org/sites/nationalslag/files/documents/nsa{\_}182-6{\_}properties{\_}and{\_}uses{\_}slag.pdf`.

Li, C., Sun, H. and Li, L. (2010). 'A review: The comparison between alkali-activated slag (Si + Ca) and metakaolin (Si + Al) cements'. In: *Cement and Concrete Research* 40.9, pp. 1341–1349.

Lide, D.R. (2005). *CRC Handbook of chemistry and physics*. 85th Edit. Boca Raton, FL: CRC Press Inc.

Lloyd, N.A. and Rangan, B.V. (2010). 'Geopolymer concrete with fly ash'. In: *Second International Conference on Sustainable Construction Materials and Technologies* 7.

Model Code (2010). *FIB. Special Activity Group 5*. CEB and FIB.

Montgomery, D.C. and Runger, G.C. (2007). *Applied statistics and probability for engineers*. John Wiley & Sons, Inc.

Motorwala, A., Shah, V., Kammula, R., Nannapaneni, P. and Raijiwala, D.B. (2013). 'Alkali activated fly-ash based geopolymer concrete'. In: *International Journal of Emerging Technology and Advanced Engineering* 3.1, pp. 159–166.

Nath, P. and Sarker, P.K. (2012). 'Geopolymer concrete for ambient curing condition'. In: *Australasian Structural Engineering Conference 2012: The past, present and future of Structural Engineering*.

Occidental Chemical Corporation (2013). *Caustic soda handbook*. URL: http://www.oxychile.cl/rps{_}oxychile{_}v56/OpenSite/OxyEspa{\~{n}}ol/ProductosyServicios/SodaC{\'{a}}usticaL{\'{i}}quida/20080124144950/HandbookCausticSoda{_}OFICIAL.pdf.

PCA (2015). *Global cement consumption on the rise*. URL: http://www.cement.org/newsroom/2015/06/03/global-cement-consumption-on-the-rise (visited on 31/07/2015).

Palomo, A., Grutzeck, M.W. and Blanco, M.T. (1999). 'Alkali-activated fly ashes: A cement for the future'. In: *Cement and Concrete Research* 29.8, pp. 1323–1329.

Pedziwiatr, J. (2008). 'Influence of internal cracks on bond in cracking concrete structures'. In: *Archives of civil and mecahincal engineering* VIII.

Penelis, G.G. and Penelis, G.G. (2014). *Concrete Buildings in Seismic Regions*. Taylor & Francis.

Perrie, B. (2009). 'Strength of hardened concrete'. In: *Fulton's concrete technology*. Ed. by G. Owens. Ninth Edit. Midrand, South Africa: Cement & Concrete Institute. Chap. 7, pp. 97–110.

Provis, J.L. and Van Deventer, J.S.J. (2009). 'Introduction to geopolymers'. In: *Geopolymers: Structures, processing, properties and application*. Ed. by J.L. Provis and J.S.J. Van Deventer. First Edit. Woodhead publishing. Chap. 1, pp. 1 –11.

Provis, J.L. and van Deventer, J.S.J (Eds.) (2014). *Alkali avtivated materials: State of the Art Report, RILEM TC 224-AAM*.

Puertas, F., Martínez-Ramírez, S., Alonso, S. and Vázquez, T. (2000). 'Alkali-activated fly ash/slag cements. Strength behaviour and hydration products'. In: *Cement and Concrete Research* 30.10, pp. 1625–1632.

Rangan, V. (2008). 'Low-Calcium, Fly-Ash-Based Geopolymer Concrete'. In: *Concrete Construction Engineering Handbook*. Ed. by E.G. Nawy. Second Edi. CRC Press, Taylor & Francis Group. Chap. 26.

Reynolds, C.E., Steedman, J.C. and Threlfall, A.J. (2008). *Concrete Designer's Handbook*. Taylor & Francis.

Robberts, J.M. and Marchall, V. (2010). *Analysis and Design of Concrete Structures*. Cement & Concrete Institute.

Roy, D.M. (1999). 'Alkali-activated cements: Opportunities and challenges'. In: *Cement and Concrete Research* 29.2, pp. 249–254.

SAISC (2013). *The Red Book. Southern African Steel Construction Handbook*. Southern African Institute of Steel Construction.

SANS 201 (2008). *South African National Standard. Sieve analysis, fines content and dust content of aggregates*. Pretoria, South Africa: South African Bureau of Standards.

SANS 50450-1 (2014). *South African National Standard. Fly ash for concrete - Definition, specification and conformity criteria*. Pretoria, South Africa: South African Bureau of Standards.

SANS 5844 (2014). *South African National Standard. Particle and relative densities of aggregates*. Pretoria, South Africa: South African Bureau of Standards.

SANS 6892-1 (2010). *South African National Standard. Metallic materials - Tensile testing - Method of test at room temperature*. Pretoria, South Africa: South African Bureau of Standards.

Sakulich, A.R., Anderson, E., Schauer, C.L. and Barsoum, M.W. (2010). 'Influence of Si:Al ratio on the microstructural and mechanical properties of a fine-limestone aggregate alkali-activated slag concrete'. In: *Materials and Structures* 43.7, pp. 1025–1035.

Schilling, P.J., Butler, L.G., Roy, A. and Eaton, H.C. (1994). '^{29}Si and ^{27}Al MAS-NMR of NaOH-Activated Blast-Furnace Slag'. In: *Journal of the American Ceramic Society* 77.9, pp. 2363–2368.

Shi, C., Krivenko, P.V. and Roy, D (2006). *Alkali-Activated Cements and Concretes*. Taylor & Francis, pp. 6–29.

Siemens, VAI (2011). *SIMETAL Corex technology Industrially and commercially proven iron making*. URL: `http://www.industry.siemens.com/datapool/industry/industrysolutions/metals/simetal/en/SIMETAL-Corex-technology-en.pdf`.

Silverstrim, T, Rostami, H, Larrade, J.C and Samadi-Maybody, A (1997). *Fly ash cementitous material and method of making product*.

Slag Cement Association, SCA (2002). *Slag cement*. URL: `http://www.slagcement.org/pdf/no1slagcement.pdf`.

Sofi, M., Deventer, J.S.J. van, Mendis, P.A. and Lukey, G.C. (2007). 'Engineering properties of inorganic polymer concretes (IPCs)'. In: *Cement and Concrete Research* 37.2, pp. 251–257.

Statista (2016). *United states and world cement production in 2010 and 2015*. URL: `http://www.statista.com/statistics/219343/cement-production-worldwide/` (visited on 01/09/2016).

Sumajouw, D.M.J and Rangan, B.V. (2006). *Low-calcium fly ash-based geopolymer concrete: Reinforced beams and columns*. Tech. rep. Faculty of Engineering Curtin University of Technology Perth, Australia.

Sumajouw, D.M.J., Hardjito, D., Wallah, S.E. and Rangan, B.V. (2007). 'Fly ash-based geopolymer concrete: Study of slender reinforced columns'. In: *Journal of Materials Science* 42.9, pp. 3124–3130.

Temuujin, J., Riessen, A. van and Williams, R. (2009). 'Influence of calcium compounds on the mechanical properties of fly ash geopolymer pastes'. In: *Journal of Hazardous Materials* 167.1-3, pp. 82–88.

Thieme, C. (2000). 'Sodium carbonate'. In: *Ullmann's Encyclopedia of Industrial Chemisty* 33, pp. 209–317.

Van Chanh, N., Trung, B.D. and Van Tuan, D. (2008). 'Recent research geopolymer concrete'. In: *Civil Engineering*, pp. 235–241.

Van Jaarsveld, J.G.S, Van Deventer, J.S.J. and Lorenzeni, L. (1997). 'The potential use of geopolymeric materials to immobilise toxic metals: Part I. Theory and applications'. In: 10.7, pp. 659–669.

Wallah, S.E. and Rangan, B.V. (2006). *Low-calcium fly ash-based geopolymer concrete: Long-term properties*. Tech. rep. Faculty of Engineering, Curtin University of Technology, Perth Australia.

Wallah, S.E. and Hardjito, D. (2015). 'Assessing the shrinkage and creep of alkali-activated concrete binders'. In: *Handbook of alkali-activated cements, mortars and concretes*. Ed. by F. Pacheco-Torgal, J.A. Labrincha, C. Leonelli, A. Palomo and P. Chindaprasirt. Sawston, Cambridge, UK: Woodhead publishing. Chap. 10, pp. 265–290.

Wang, S., Scrivener, K.L. and Pratt, P.L. (1994). 'Factors affecting the strength of alkali-activated slag'. In: *Cement and Concrete Research* 24.6, pp. 1033–1043.

Wight, J.K. and MacGregor, J.G. (2012). *Reinforced Concrete. Mechanics and Design*. Pearson.

Xu, H. and Van Deventer, J.S.J. (2000). 'The geopolymerisation of alumino-silicate minerals'. In: *International Journal of Mineral Processing* 59.3, pp. 247–266.

Yip, C.K. and Van Deventer, J.S.J. (2003). 'Microanalysis of calcium silicate hydrate gel formed within a geopolymeric binder'. In: *Journal of Materials Science* 38.18, pp. 3851–3860.

Yip, C.K., Lukey, G.C., Provis, J.L. and Van Deventer, J.S.J. (2008). 'Effect of calcium silicate sources on geopolymerisation'. In: *Cement and Concrete Research* 38, pp. 554–564.

Appendix A

Mechanical properties

The mechanical properties that was obtained for all the mixes are summarised within this Appendix. The mechanical properties include: workability; cube strength ($f_{c,cube}$); cylinder strength ($f_{c,cyl}$); density (ρ); elastic modulus (E_c); stress percentage ($f_{\%}$); and the strain percentage ($\varepsilon_{\%}$). The standard deviation (SD) and coefficient of variation (CV) are also included. The CV is indicated in red for values higher than 10 %.

The mixes containing 40 % slag is given in Table A.1, while the 20 % slag is given in Table A.2. The reference mix is indicated in blue. The mixes where alternative activators were used, is given in Table A.3. The reinforced beam (RB) and pull-out(PO) mixes are given in Table A.4.

Table A.1: Mechanical properties of mixes containing 40 % slag

Mix	Workability [mm]	Cube strength [MPa]			Cylinder strength [MPa]			Density [kg/m^3]			Elastic modulus [GPa]			Stress percentage [%]			Strain percentage [%]		
		$f_{c,cube}$	SD	CV	$f_{c,cyl}$	SD	CV	ρ	SD	CV	E_c	SD	CV	$f_{\%}$	SD	CV	$\varepsilon_{\%}$	SD	CV
SH-40-C4N3.5M0.75	325	28.8	1.2	4.2	24.8	0.6	2.4	2278.6	28.4	1.2	26.9	3.7	13.6	70.0	5.6	8.0	48.9	10.0	20.4
SH-40-C4N3.5M1	405	9.2	0.4	3.9	5.2	0.1	2.6	2272.0	14.8	0.7	10.6	1.1	10.1	77.2	0.5	0.7	33.0	1.9	5.6
SH-40-C4N3.5M2	615	23.9	0.7	3.1	17.9	0.4	2.3	2273.6	20.6	0.9	13.1	0.6	4.6	58.1	2.6	4.5	28.4	1.7	5.9
SH-40-C4N4.3M1	605	5.4	0.4	6.4	3.3	0.2	6.9	2211.2	49.6	2.2	11.5	3.9	33.6	69.9	0.5	0.7	22.0	3.5	16.1
SH-40-C4N5M1	740	-	-	-	-	-	-	2159.8	32.4	1.5	-	-	-	-	-	-	-	-	-
SH-40-C4N5.8M1	-	-	-	-	-	-	-	2147.7	50.3	2.3	-	-	-	-	-	-	-	-	-
SH-40-C6N3.5M1	275	22.2	3.5	15.6	17.2	2.0	11.6	2304.8	5.6	0.2	19.8	0.3	1.3	63.0	1.0	1.7	31.4	3.2	10.3
SH-40-C6N4.3M1	450	27.6	0.9	3.4	20.8	1.6	7.9	2304.2	32.5	1.4	23.2	1.2	5.3	65.2	4.1	6.3	33.9	2.2	6.3
SH-40-C6N5M1	605	20.9	2.2	10.4	16.7	2.1	12.3	2291.7	45.8	2.0	20.2	2.1	10.4	65.6	3.1	4.7	30.3	1.3	4.2
SH-40-C6N5.8M1	735	20	1.5	7.6	14.9	0.8	5.3	2235.3	26.4	1.2	18.8	1.1	5.9	64.6	1.8	2.8	30.3	2.2	7.2
SH-40-C8N3.5M1	180	33.8	1.1	3.1	24.8	1.1	4.1	2283.6	32.7	1.4	22.8	0.3	1.4	65.2	0.4	0.6	36.7	1.8	5.0
SH-40-C8N4.3M1	385	40.6	0.7	1.6	31.5	2.0	6.4	2322.1	3.3	0.1	23.0	1.0	4.1	66.2	0.7	1.1	44.4	1.5	3.4
SH-40-C8N5M0.75	410	52.3	2.9	5.6	47.8	2.8	5.8	2354.0	26.0	1.1	32.0	3.0	9.3	69.0	0.8	1.2	52.7	2.1	3.9
SH-40-C8N5M1	515	43.5	1.3	2.9	31.3	0.9	3.0	2316.5	25.3	1.1	21.6	0.3	1.4	66.7	3.3	5.0	46.6	6.6	14.1
SH-40-C8N5M2	715	29.8	0.7	2.3	17.6	0.9	5.3	2244.1	28.4	1.3	9.1	0.4	4.5	65.6	1.9	2.9	45.9	4.0	8.6
SH-40-C8N5.8M1	715	45.4	1.2	2.7	33.8	0.4	1.1	2332.9	18.3	0.8	20.8	1.8	8.8	68.9	2.3	3.3	44.2	4.4	9.9
SH-40-C12N3.5M1	-	52.5	1.0	1.9	43.2	0.6	1.4	2322.6	42.0	1.8	27.2	1.9	7.0	66.4	2.4	3.6	45.8	2.8	6.2
SH-40-C12N5M1	370	57.3	0.3	0.5	41.2	0.7	1.7	2333.3	16.9	0.7	24.1	1.5	6.2	84.1	2.9	3.4	74.8	2.3	3.1
SH-40-C12N5.8M0.75	435	67.1	1.1	1.6	57.4	0.9	1.6	2333.4	8.2	0.4	32.1	1.0	3.1	75.4	3.9	5.1	61.9	7.9	12.8
SH-40-C12N5.8M1	585	56.5	2.1	3.6	44.3	1.2	2.7	2355.7	16.5	0.7	23.6	0.5	2.1	74.0	2.5	3.3	57.5	1.3	2.2
SH-40-C12N5.8M2	730	30.0	0.7	2.3	18.1	0.4	2.3	2291.0	16.4	0.7	8.6	0.1	1.6	66.2	1.6	2.3	46.3	2.3	4.9
SH-40-C8N5M1-G50	375	43.7	0.6	1.3	32.0	1.3	3.9	2270.3	15.6	0.7	20.2	0.7	3.7	64.9	2.1	3.2	44.4	5.3	12.0
SH-40-C8N5M1-G70	550	48.8	1.2	2.5	32.2	1.5	4.5	2389.0	17.1	0.7	19.0	0.2	1.1	70.3	2.8	3.9	51.6	2.6	5.1
SH-40-C8N5M1-6mm	345	46.2	1.0	2.1	31.4	0.9	3.0	2315.8	23.2	1.0	25.0	2.1	8.3	64.5	3.5	5.5	36.9	3.7	10.1
SH-40-C8N5M1-S50	345	38.6	1.5	4.0	31.2	1.1	3.7	2217.6	18.4	0.8	16.9	0.2	1.2	68.7	2.1	3.1	50.0	3.9	7.8
SH-40-C8N5M1-S60	400	43.7	1.5	3.5	36.2	1.8	5.1	2288.8	46.4	2.0	18.3	1.0	5.5	68.8	3.2	4.6	52.6	6.1	11.6
SH-40-C8N5M1-S70	470	44.6	1.1	2.5	33.5	1.1	3.4	2313.9	28.1	1.2	16.8	0.8	4.9	73.3	1.1	1.4	57.7	3.2	5.5

Table A.2: Mechanical properties of mixes containing 20 % slag

Mix	Workability [mm]	Cube strength [MPa]			Cylinder strength [MPa]			Density [kg/m^3]			Elastic modulus [GPa]			Stress percentage [%]			Strain percentage [%]		
		$f_{c,cube}$	SD	CV	$f_{c,cyl}$	SD	CV	ρ	SD	CV	E_c	SD	CV	$f_{\%}$	SD	CV	$\varepsilon_{\%}$	SD	CV
SH-20-C4N3.5M0.75	380	-	-	-	-	-	-	2195.1	15.3	0.7	-	-	-	-	-	-	-	-	-
SH-20-C4N3.5M1	550	-	-	-	-	-	-	2196.2	23.7	1.1	-	-	-	-	-	-	-	-	-
SH-20-C4N3.5M2	700	8.0	0.1	1.3	5.4	0.1	2.1	2207.5	13.4	0.6	9.8	0.4	4.5	75.9	0.6	0.8	36.1	2.6	7.3
SH-20-C4N4.3M1	-	-	-	-	-	-	-	2178.6	42.7	2.0	-	-	-	-	-	-	-	-	-
SH-20-C6N3.5M1	335	7.1	0.2	7.6	5.0	0.4	7.6	2258.0	37.6	1.7	12.4	1.2	9.3	71.6	0.9	1.2	28.1	1.1	4.0
SH-20-C6N4.3M1	495	7.5	0.6	7.7	5.0	0.1	3.0	2240.8	22.0	1.0	10.3	1.1	11.0	76.4	2.3	3.0	35.0	4.8	13.9
SH-20-C6N5M1	670	-	-	-	-	-	-	2238.8	26.9	1.2	-	-	-	-	-	-	-	-	-
SH-20-C6N5.8M1	770	7.2	0.3	4.8	5.6	0.1	1.8	2201.0	54.3	2.5	11	1.0	8.9	64.2	0.8	1.3	25.2	2.3	9.0
SH-20-C8N3.5M1	205	11.0	0.5	4.9	7.6	0.7	8.9	2274.2	40.6	1.8	15.0	1.6	10.3	71.1	3.4	4.8	27.7	4.2	15.0
SH-20-C8N4.3M1	450	22.9	1.1	4.7	19.1	0.7	3.9	2274.5	22.5	1.0	26.3	2.7	10.1	64.9	5.3	8.1	35.8	6.1	17.0
SH-20-C8N5M0.75	505	18.6	0.6	3.4	14.8	0.6	4.2	2300.5	30.9	1.3	19.6	1.5	7.7	68.4	2.2	3.2	33.2	3.7	11.0
SH-20-C8N5M1	595	24.6	0.4	1.8	17.9	0.1	0.5	2291.3	21.1	0.9	19.8	0.3	1.3	69.1	2.0	2.9	37.8	0.7	1.8
SH-20-C8N5M2	750	15.7	0.7	4.6	9.8	0.3	2.9	2213.1	45.0	2.0	10.3	0.3	2.9	63.7	2.8	4.3	31.0	8.5	27.5
SH-20-C8N5.8M1	715	26.0	1.0	3.7	21.3	0.5	2.3	2267.7	43.1	1.9	23.1	3.3	14.1	67.6	4.0	5.9	36.9	4.6	12.5
SH-20-C12N5M1	510	35.9	0.3	0.7	27.3	0.4	1.3	2319.6	30.2	1.3	18.9	0.5	2.5	64.3	1.3	2.0	42.9	1.6	3.7
SH-20-C12N5.8M0.75	455	39.7	1.1	2.7	34.3	0.2	0.6	2328.7	35.8	1.5	31.2	1.3	4.2	62.9	2.7	4.4	39.4	1.8	4.5
SH-20-C12N5.8M1	615	41.2	0.7	1.6	30.4	0.9	2.9	2340.5	33.7	1.4	20.3	0.2	1.1	65.7	0.9	1.3	43.4	3.2	7.4
SH-20-C12N5.8M2	740	18.3	0.9	4.8	10.3	0.5	4.4	2228.9	30.6	1.4	8.2	0.6	7.8	65.4	1.7	2.7	31.3	5.2	16.6

Table A.3: Mechanical properties of mixes containing alternative activators

Mix	Workability [mm]	Cube strength [MPa]			Cylinder strength [MPa]			Density [kg/m^3]			Elastic modulus [GPa]			Stress percentage [%]			Strain percentage [%]		
		$f_{c,cube}$	SD	CV	$f_{c,cyl}$	SD	CV	ρ	SD	CV	E_c	SD	CV	$f_{\%}$	SD	CV	$\varepsilon_{\%}$	SD	CV
SC-40-C2N3.5M1	25	-	-	-	-	-	-	2283.1	24.3	1.1	-	-	-	-	-	-	-	-	-
C-40-C2N3.5	360	-	-	-	-	-	-	2278.5	41.8	1.8	-	-	-	-	-	-	-	-	-
SC-100-C2N3.5M1	20	17.5	6.8	38.9	-	-	-	2285.8	33.4	1.5	-	-	-	-	-	-	-	-	-
SC-40(20)-C2N3.5M1	-	-	-	-	-	-	-	-	-	-	-	-	-	-	-	-	-	-	-
S-40-N2.9	50	-	-	-	-	-	-	2134.4	19.3	1.0	-	-	-	-	-	-	-	-	-
S-40-N5	425	-	-	-	-	-	-	2142.3	24.9	1.2	-	-	-	-	-	-	-	-	-
S-40(20)-N2.9	-	-	-	-	-	-	-	-	-	-	-	-	-	-	-	-	-	-	-

Table A.4: Mechanical properties of mixes for the RB test and PO test

Mix	Workability [mm]	Cube strength [MPa]			Cylinder strength [MPa]			Density [kg/m^3]			Elastic modulus [GPa]			Stress percentage [%]			Strain percentage [%]		
		$f_{c,cube}$	SD	CV	$f_{c,cyl}$	SD	CV	ρ	SD	CV	E_c	SD	CV	$f_{\%}$	SD	CV	$\varepsilon_{\%}$	SD	CV
AAM-mix1 (Beam 1)	-	35.6	0.7	1.8	27.0	2.0	7.5	2269.9	27.2	1.2	12.2	0.8	6.5	62.7	4.0	6.4	49.3	4.8	9.7
AAM-mix1 (Beam 2)	-	36.5	1.1	3.0	25.9	1.0	4.0	2299.9	1.8	0.1	12.3	0.4	2.8	68.7	4.3	6.3	52.5	5.4	10.3
OPC-mix1 (Beam 1)	-	42.8	0.8	1.9	35.6	1.0	2.8	2399.4	3.9	0.2	44.6	2.8	6.3	67.7	4.4	6.5	43.7	6.1	14.1
OPC-mix1 (Beam 2)	-	41.1	1.3	3.3	36.8	0.5	1.4	2402.6	2.4	0.1	46.1	2.5	5.4	60.7	3.8	6.2	37.0	4.8	13.1
AAM-mix2 (Beam 1)	-	22.2	0.1	0.5	21.2	0.7	3.5	2214.6	13.1	0.6	25.3	1.5	6.0	56.8	4.5	7.9	27.1	3.6	13.4
AAM-mix2 (Beam 2)	-	21.2	0.7	3.3	20.7	0.4	2.0	2240.6	14.2	0.6	25.2	3.3	13.1	60.9	5.3	8.7	32.2	5.5	17.2
OPC-mix2 (Beam 1)	-	24.2	0.2	1.0	23.3	0.3	1.2	2399.4	3.9	0.2	33.1	4.5	13.6	54.2	12.9	23.8	25.9	4.3	16.6
OPC-mix2 (Beam 2)	-	25.8	0.6	2.3	23.5	0.5	2.3	2399.8	4.7	0.2	36.8	3.5	9.6	64.9	7.5	11.6	32.6	9.0	27.7
AAM-mix1 (PO)	-	40.5	0.4	1.1	29.3	0.7	2.5	2301.9	10.4	0.5	18.3	1.0	5.2	64.3	1.9	3.0	45.2	2.4	5.3
OPC-mix1 (PO)	-	41.5	1.5	3.6	36.7	2.0	5.4	2400.6	6.3	0.3	44.9	4.3	9.6	68.0	5.4	7.9	45.9	5.6	12.1
AAM-mix2 (PO)	-	19.7	0.2	0.9	19.1	0.2	0.8	2226.8	27.3	1.2	20.9	0.6	2.7	60.8	1.3	2.1	31.6	1.0	3.2
OPC-mix2 (PO)	-	25.3	1.0	3.8	24.1	0.4	1.7	2338.7	9.0	0.4	37.1	2.2	5.8	70.1	4.9	7.0	38.3	6.7	17.4

Appendix B

Reinforced beam test setup

The frame setup that was constructed for the reinforced beam (RB) test is shown in Figure B.1. The Instron was fixed to a free standing frame. The RB specimens were simply supported over a span of 2.7 m. A spreader beam was placed on two rollers in order to apply the two point loads on the RB specimens. A bearing was used between the Instron and the spreader beam.

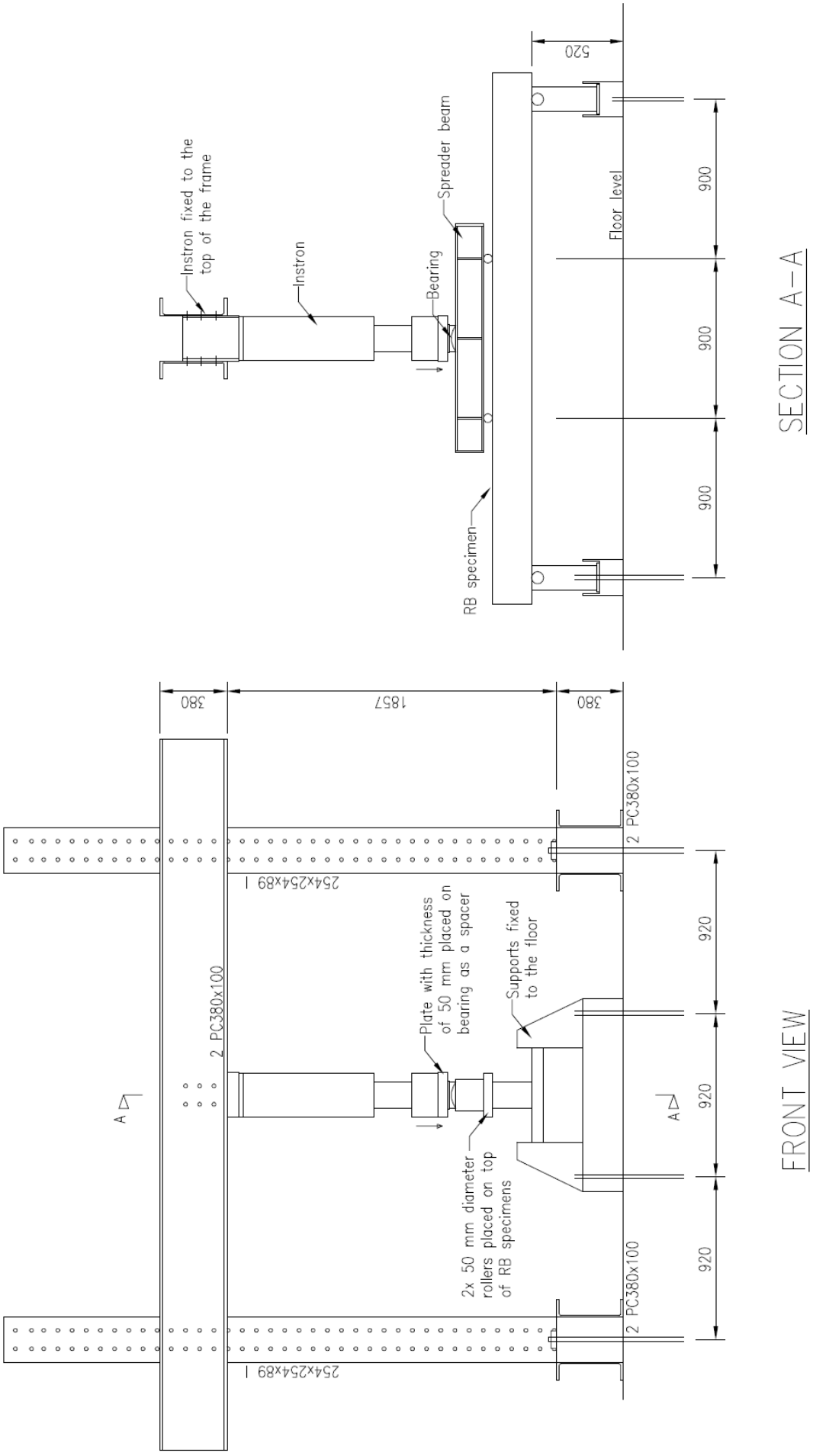

Figure B.1: The frame setup constructed for RB test

Appendix C

Reinforced beam crack results

The results that was obtained for the crack formation of the reinforced beam (RB) specimens are given in this Appendix. The crack widths at the different load increments and the spacing between the cracks are given for all the RB specimens in Table C.1 to C.8. The cracks spacings are given from the left support towards the right support (See Figure C.1). The crack patterns for each RB specimens is demonstrated in Figure C.1.

Table C.1: Crack development of AAM-mix1 (Beam 1)

	Crack widths [mm]						
Crack number	15 kN	30 kN	45 kN	60 kN	75 kN	Crack number	Crack spacing [mm]
1	0.05	0.1	0.15	0.2		18	340
2	0.05	0.15	0.25	0.4		19	95
3	0.05	0.1	0.25	0.25		13	130
4	0.05	0.15	0.2	0.25		14	160
5	0.05	0.15	0.2	0.3		1	90
6	0.05	0.1	0.15	0.25		2	115
7	0.05	0.2	0.3	0.3		3	115
8	0.05	0.15	0.25	0.3		15	80
9	0.05	0.15	0.2	0.25		4	95
10	0.05	0.05	0.1	0.2		5	75
11	0.05	0.1	0.15	0.2		6	110
12	0.05	0.05	0.1	0.15		20	80
13		0.05	0.1	0.15		7	70
14		0.1	0.2	0.3		16	110
15		0.1	0.1	0.15		8	120
16		0.1	0.15	0.2		9	80
17		0.05	0.1	0.15		10	90
18			0.05	0.1		11	155
19			0.05	0.1		12	100
20			0.05	0.15		17	140
21			0.05	0.05		21	100

Table C.2: Crack development of AAM-mix1 (Beam 2)

	Crack widths [mm]						
Crack number	15 kN	30 kN	45 kN	60 kN	75 kN	Crack number	Crack spacing [mm]
1	0.05	0.1	0.1	0.15		21	300
2	0.05	0.1	0.1	0.1		1	120
3	0.05	0.1	0.25	0.35		2	120
4	0.05	0.15	0.25	0.3		3	135
5	0.05	0.1	0.2	0.3		4	100
6	0.05	0.2	0.2	0.2		5	120
7	0.05	0.1	0.2	0.25		6	120
8	0.1	0.2	0.3	0.35		18	120
9	0.05	0.1	0.15	0.2		7	70
10	0.05	0.05	0.1	0.1		19	55
11	0.05	0.1	0.15	0.2		8	110
12	0.05	0.1	0.15	0.25		9	100
13	0.05	0.1	0.2	0.25		10	60
14	0.05	0.05	0.15	0.2		11	70
15	0.05	0.1	0.15	0.25		12	135
16	0.05	0.1	0.15	0.15		13	110
17	0.05	0.1	0.15	0.15		14	80
18		0.05	0.1	0.15		15	135
19		0.05	0.1	0.15		16	150
20			0.05	0.1		17	90
21				0.1		20	130
22				0.05		21	50

Table C.3: Crack development of OPC-mix1 (Beam 1)

	Crack widths [mm]						
Crack number	15 kN	30 kN	45 kN	60 kN	75 kN	Crack number	Crack spacing [mm]
1	0.05	0.1	0.1	0.2		13	425
2	0.05	0.05	0.1	0.15		3	180
3		0.05	0.05	0.05		4	120
4		0.05	0.1	0.1		5	110
5		0.05	0.15	0.25		14	120
6		0.1	0.2	0.3		1	85
7		0.05	0.05	0.1		6	130
8		0.1	0.15	0.25		7	115
9		0.05	0.1	0.2		15	50
10		0.05	0.1	0.15		8	120
11		0.05	0.15	0.25		9	160
12		0.05	0.05	0.05		10	90
13			0.05	0.1		2	110
14			0.05	0.05		11	150
15			0.05	0.1		18	95
16			0.05	0.05		12	105
17			0.05	0.05		16	70
18				0.05		17	60

Table C.4: Crack development of OPC-mix1 (Beam 2)

	Crack widths [mm]						
Crack number	15 kN	30 kN	45 kN	60 kN	75 kN	Crack number	Crack spacing [mm]
1	0.05	0.05	0.15	0.2	0.3	19	350
2		0.05	0.05	0.05	0.05	14	120
3		0.05	0.05	0.1	0.15	2	90
4		0.05	0.05	0.1	0.15	15	85
5		0.05	0.15	0.2	0.35	3	95
6		0.05	0.15	0.2	0.3	4	55
7		0.05	0.1	0.15	0.2	5	140
8		0.05	0.15	0.15	0.2	6	120
9		0.05	0.15	0.2	0.2	7	100
10		0.05	0.15	0.2	0.25	8	95
11		0.05	0.1	0.15	0.2	1	150
12		0.05	0.1	0.15	0.25	17	65
13		0.05	0.05	0.1	0.2	9	95
14			0.05	0.05	0.05	10	135
15			0.05	0.05	0.1	11	175
16			0.05	0.05	0.1	12	155
17				0.05	0.05	13	190
18				0.05	0.05	16	120
19					0.05	18	105

Table C.5: Crack development of AAM-mix2 (Beam 1)

	Crack widths [mm]						
Crack number	15 kN	30 kN	45 kN	60 kN	75 kN	Crack number	Crack spacing [mm]
1	0.05	0.1	0.1	0.1		18	240
2	0.05	0.1	0.1	0.15		16	145
3	0.05	0.05	0.05	0.1		1	115
4	0.05	0.1	0.15	0.25		2	160
5	0.05	0.1	0.15	0.2		3	110
6	0.05	0.05	0.15	0.2		4	120
7	0.05	0.05	0.1	0.15		5	90
8	0.05	0.1	0.15	0.2		6	105
9	0.05	0.1	0.15	0.2		7	80
10	0.05	0.1	0.15	0.25		8	80
11	0.05	0.1	0.2	0.3		9	135
12	0.05	0.1	0.2	0.25		19	55
13	0.05	0.05	0.1	0.2		10	70
14	0.05	0.1	0.15	0.2		11	125
15	0.05	0.05	0.1	0.15		20	120
16		0.05	0.1	0.1		12	65
17		0.05	0.1	0.15		13	135
18			0.1	0.15		14	110
19			0.05	0.1		15	185
20			0.05	0.05		17	150

Table C.6: Crack development of AAM-mix2 (Beam 2)

	Crack widths [mm]						
Crack number	15 kN	30 kN	45 kN	60 kN	75 kN	Crack number	Crack spacing [mm]
1	0.05	0.05	0.1	0.1		23	120
2	0.05	0.15	0.2	0.3		13	175
3	0.05	0.1	0.2	0.3		14	110
4	0.05	0.1	0.2	0.25		19	90
5	0.05	0.05	0.15	0.2		1	120
6	0.05	0.1	0.2	0.3		20	95
7	0.05	0.1	0.2	0.3		2	110
8	0.05	0.1	0.15	0.2		15	110
9	0.05	0.1	0.2	0.25		3	105
10	0.05	0.1	0.15	0.25		4	130
11	0.05	0.05	0.1	0.25		16	70
12	0.05	0.05	0.1	0.15		5	110
13		0.05	0.05	0.05		6	80
14		0.05	0.1	0.1		7	95
15		0.05	0.1	0.2		8	90
16		0.05	0.1	0.15		9	120
17		0.05	0.05	0.1		10	95
18		0.05	0.1	0.1		21	130
19			0.05	0.05		11	35
20			0.05	0.1		12	110
21			0.05	0.05		17	55
22			0.05	0.05		18	160
23				0.1		22	120

Table C.7: Crack development of OPC-mix2 (Beam 1)

	Crack widths [mm]						
Crack number	15 kN	30 kN	45 kN	60 kN	75 kN	Crack number	Crack spacing [mm]
1	0.05	0.1	0.15	0.25		15	325
2	0.05	0.05	0.1	0.2		5	105
3	0.05	0.05	0.1	0.2		6	160
4	0.05	0.05	0.1	0.15		7	130
5		0.05	0.05	0.1		8	70
6		0.05	0.05	0.1		1	160
7		0.05	0.05	0.1		16	55
8		0.05	0.1	0.15		9	120
9		0.05	0.1	0.15		2	95
10		0.05	0.1	0.15		10	115
11		0.05	0.05	0.1		3	135
12		0.05	0.05	0.1		11	135
13		0.05	0.05	0.1		4	115
14		0.05	0.05	0.05		12	55
15			0.05	0.1		13	115
16			0.05	0.1		14	90
17			0.05	0.05		17	75
18			0.05	0.05		18	130
19			0.05	0.05		19	95
20			0.05	0.05		20	160

Table C.8: Crack development of OPC-mix2 (Beam 2)

	Crack widths [mm]						
Crack number	15 kN	30 kN	45 kN	60 kN	75 kN	Crack number	Crack spacing [mm]
1	0.05	0.05	0.1	0.2		19	270
2	0.05	0.05	0.1	0.2		16	135
3	0.05	0.05	0.1	0.15		4	70
4		0.05	0.05	0.1		5	190
5		0.05	0.05	0.15		6	150
6		0.05	0.1	0.2		1	125
7		0.05	0.1	0.1		2	160
8		0.05	0.1	0.15		7	85
9		0.05	0.1	0.1		3	130
10		0.05	0.1	0.2		8	65
11		0.05	0.05	0.1		17	90
12		0.05	0.1	0.2		9	85
13		0.05	0.05	0.1		10	100
14		0.05	0.05	0.1		11	125
15		0.05	0.05	0.05		12	90
16			0.05	0.05		13	135
17			0.05	0.1		14	70
18			0.05	0.05		15	125
19				0.05		18	140

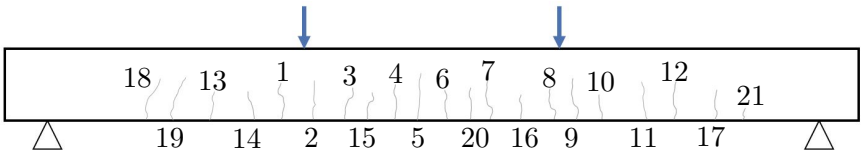

(a) AAM-mix1 (Beam 1)

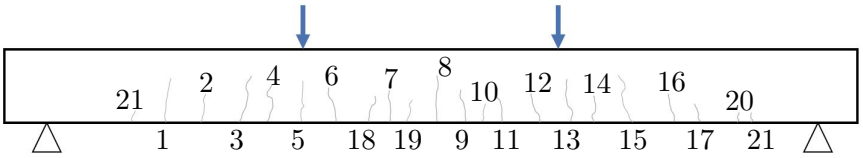

(b) AAM-mix1 (Beam 2)

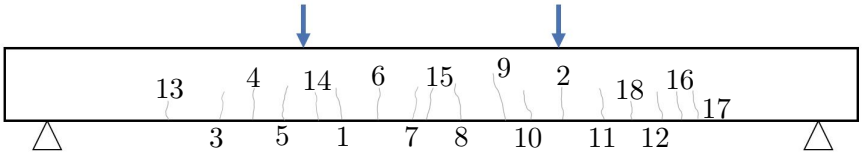

(c) OPC-mix1 (Beam 1)

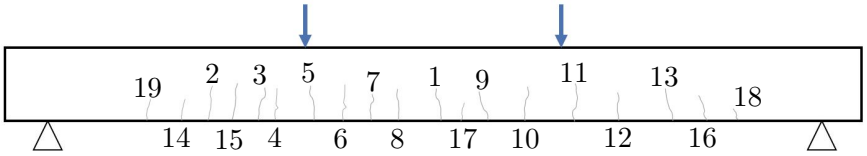

(d) OPC-mix1 (Beam 2)

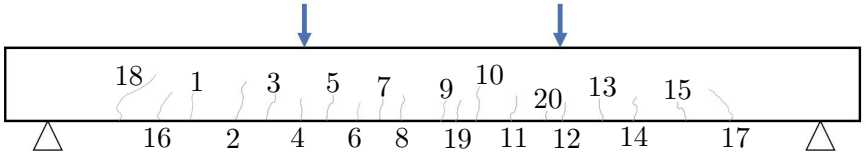

(e) AAM-mix2 (Beam 1)

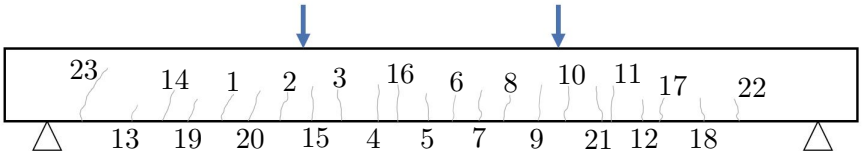

(f) AAM-mix2 (Beam 2)

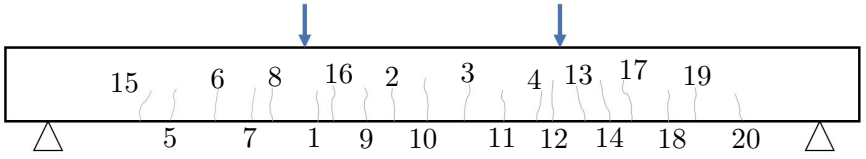

(g) OPC-mix2 (Beam 1)

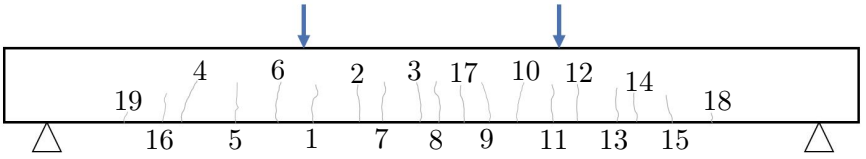

(h) OPC-mix2 (Beam 2)

Figure C.1: Crack patterns for RB specimens

Appendix D

Mix constituents

The proportions of the mix constituents are given for all the mixes in this Appendix. The mix proportions for all the mixes containing sodium hydroxide and sodium silicate as the alkaline activators, are given in Table D.1. The reference mix is indicated in blue. The alternative activator mixes are given in Table D.2, while Table D.3 contains the mix proportions for the reinforced beam (RB) mixes and pull-out (PO) mixes.

Appendix D. Mix constituents

Table D.1: Mix proportions for mixes containing sodium hydroxide and sodium silicate [kg/m^3]

Mix	Course aggregate	Fine aggregate	Slag	Fly ash	Sodium silicate	Sodium hydroxide	Water
SH-40-C4N3.5M0.75	1030	690	180	270	41	105	75
SH-40-C4N3.5M1	1030	690	180	270	54	94	75
SH-40-C4N3.5M2	1030	690	180	270	108	53	75
SH-40-C4N4.3M1	1030	690	180	270	67	116	75
SH-40-C4N5M1	1030	690	180	270	77	134	75
SH-40-C4N5.8M1	1030	690	180	270	89	155	75
SH-40-C6N3.5M1	1030	690	180	270	55	66	75
SH-40-C6N4.3M1	1030	690	180	270	67	81	75
SH-40-C6N5M1	1030	690	180	270	78	94	75
SH-40-C6N5.8M1	1030	690	180	270	90	108	75
SH-40-C8N3.5M1	1030	690	180	270	54	51	75
SH-40-C8N4.3M1	1030	690	180	270	67	63	75
SH-40-C8N5M0.75	1030	690	180	270	58	81	75
SH-40-C8N5M1	1030	690	180	270	77	72	75
SH-40-C8N5M2	1030	690	180	270	154	41	75
SH-40-C8N5.8M1	1030	690	180	270	89	84	75
SH-40-C12N3.5M1	1030	690	180	270	54	36	75
SH-40-C12N5M1	1030	690	180	270	77	52	75
SH-40-C12N5.8M0.75	1030	690	180	270	67	67	75
SH-40-C12N5.8M1	1030	690	180	270	90	60	75
SH-40-C12N5.8M2	1030	690	180	270	179	34	75
SH-40-C8N5M1-G50	860	860	180	270	77	72	75
SH-40-C8N5M1-G70	1204	516	180	270	77	72	75
SH-40-C8N5M1-6mm	1030	690	180	270	77	72	75
SH-40-C8N5M1-S50	860	860	180	270	77	72	75
SH-40-C8N5M1-S60	1030	690	180	270	77	72	75
SH-40-C8N5M1-S70	1204	516	180	270	77	72	75
SH-20-C4N3.5M0.75	1030	690	90	360	41	105	75
SH-20-C4N3.5M1	1030	690	90	360	54	94	75
SH-20-C4N3.5M2	1030	690	90	360	108	53	75
SH-20-C4N4.3M1	1030	690	90	360	67	116	75
SH-20-C6N3.5M1	1030	690	90	360	55	66	75
SH-20-C6N4.3M1	1030	690	90	360	67	81	75
SH-20-C6N5M1	1030	690	90	360	78	94	75
SH-20-C6N5.8M1	1030	690	90	360	90	108	75
SH-20-C8N3.5M1	1030	690	90	360	54	51	75
SH-20-C8N4.3M1	1030	690	90	360	67	63	75
SH-20-C8N5M0.75	1030	690	90	360	58	81	75
SH-20-C8N5M1	1030	690	90	360	77	72	75
SH-20-C8N5M2	1030	690	90	360	154	41	75
SH-20-C8N5.8M1	1030	690	90	360	89	84	75
SH-20-C12N5M1	1030	690	90	360	77	52	75
SH-20-C12N5.8M0.75	1030	690	90	360	67	67	75
SH-20-C12N5.8M1	1030	690	90	360	90	60	75
SH-20-C12N5.8M2	1030	690	90	360	179	34	75

Table D.2: Mix proportions for mixes with alternative activators [kg/m^3]

Mix	Course aggregate	Fine aggregate	Slag	Fly ash	Cement	Sodium silicate	Sodium carbonate	Water
SC-40-C2N3.5M1	1030	690	180	270	-	54	100	75
C-40-C2N3.5	1030	690	180	270	-	-	145	75
SC-100-C2N3.5M1	1030	690	450	-	-	54	100	75
SC-40(20)-C2N3.5M1	1030	690	180	180	90	54	100	75
S-40-N2.9	1030	690	180	270	-	150	-	75
S-40-N5	1030	690	180	270	-	255	-	75
S-40(20)-N2.9	1030	690	180	180	90	150	-	75

Table D.3: Mix proportions RB tests and PO tests [kg/m^3]

Mix	Course aggregate	Fine aggregate	Slag	Fly ash	Cement	Limestone	Sodium silicate	Sodium carbonate	Water
AAM-mix1	1030	690	180	270	-	-	77	72	75
AAM-mix2	1030	690	90	360	-	-	77	72	75
OPC-mix1	1100	769	-	-	328	-	-	-	190
OPC-mix2	1100	827	-	-	232	22	-	-	190